Politechnika Wrocławska

Wydział Podstawowych Problemów Techniki

MASTER'S THESIS

Photocathode characterisation and ageing studies for precise-timing gaseous detectors

Author: inż. Marta Lisowska

Supervisor: prof. dr hab. inż. Grzegorz Sęk

Wrocław 2021

Acknowledgements

I would like to acknowledge everyone who played a role in creating this Master's thesis.

First of all, I would like to thank Florian Maximilian Brunbauer, my supervisor at CERN, who introduced me to the world of gaseous detectors and has been helping me at every stage of my project, from working in the laboratory, through analysing research results, to writing this Master's thesis. Your dedication had a great impact on accomplishing this task and inspired me to steer my further studies towards the field of experimental particle physics.

Secondly, I owe a deep sense of gratitude to Leszek Ropelewski, the leader of the CERN Gaseous Detector Development (GDD) group, and Eraldo Oliveri, the head of the GDD laboratory. Personal contact with such excellent specialists as you and the use of the unique experimental equipment in the laboratory have broadened my knowledge and developed my skills as well as made me grow as a young scientist.

Moreover, I thank all members of the GDD group and other collaborators, in particular Miranda van Stenis and Thomas Schneider from CERN, Lukas Sohl and Thomas Papaevangelou from CEA, Xu Wand and Yi Zhou from USTC and Triloki, Shuddha Dasgupta, Fulvio Tessarotto from INFN. Working with such friendly people, who were always eager to help me as well as give me a chance to show my creativity, was the best work environment that I could imagine.

Finally, I am enormously thankful to my parents, who supported me throughout my education. Without you, I would never be able to realise my dreams.

Abstract

The challenges of future High Energy Physics experiments, including high-pile-up environments expected in the High-Luminosity Large Hadron Collider (HL-LHC) [1], have aroused intense interest in the development of technologies for precise detectors with high time resolution. Within the PicoSec MicroMegas collaboration [2], a detector that aims at reaching a time resolution of tens of picoseconds is being developed. The first prototype of the detector demonstrated high time resolution on small scale, however, to make the concept appropriate to physics applications, several developments are required. This includes the optimalisation of the photocathode, which is at the core of the PicoSec detector.

The first prototype of the PicoSec detector uses a semi-transparent cesium iodide (CsI) photocathode [2], but the degradation of CsI quantum efficiency (QE) is a concern in the development of this concept as it directly translates to a degeneration of the detector's timing performance. It is therefore necessary to carry out measurements to quantify the photocathodes degeneration and to find alternative materials that could be used in future versions of the PicoSec detector. The characterisation of the photocathodes was performed with the use of the ASSET measurement setup [3] located in the laboratory of the Gaseous Detector Development group at the European Organization for Nuclear Research (CERN) in Switzerland. The experimental setup enables QE measurements in the VUV wavelength regime (130 - 200 nm), both in reflective and transmission modes, and allows to study the process of photocathodes accelerated ageing under X-ray irradiation. The measurements of 4 different photocathode materials were made including: CsI, diamond-like carbon (DLC), boron carbide (B_4C) and hydrogenated nanodiamonds (HND). Experimental results showed that CsI had the highest quantum efficiency, however, the degeneration of B_4C and HND was much slower. This is still not a strong argument to replace CsI photocathodes, but it suggests that these materials may be potential alternatives for CsI in the PicoSec detector. The main achievement is that the setup has been tested and the results are reliable. As a next step, more materials will be examined and evaluated for their suitability for precise-timing gaseous detectors.

Key words

photocathode, ageing studies, precise timing, gaseous detectors, quantum efficiency

Contents

Chapter 1

Introduction

The challenges of future High Energy Physics experiments, including high-pile-up environments expected in the High-Luminosity Large Hadron Collider (HL-LHC) [1], have aroused intense interest in the development of technologies for precise detectors with high time resolution. The demand of a large area coverage, high rate-capabilities and radiation hardness together with good spatial and energy resolution have started the investigation of Micro-Pattern Gaseous Detectors (MPGDs) as potential detector technologies to fulfil these requirements. Conventionally, the time resolution of gaseous detectors is on the scale of nanoseconds as a result of interaction depth differences on the millimeter-scale in the active detection volumes. Concerning the necessary time resolution for pile-up mitigation of the order of tens of picoseconds (ps), significant modifications are required for the technology to approach the desired performance.

Within the PicoSec MicroMegas collaboration [2], a precise-timing gaseous detector concept is being developed. The detector aims at reaching a time resolution of tens of ps for the detection of charged particles, which is an improvement by two orders of magnitude in comparison to the performance of conventional MPGDs. The first prototype has shown that sub-50-ps time resolution can be achieved, however, to make the concept appropriate to physics applications, several developments are required. Besides upscaling, this includes studies and optimisation of the photocathode, which is at the core of the PicoSec detector.

The photocathode is used to convert photons into electrons using the photoelectric effect [4]. It is based on a thin layer of material applied to the supporting surface. This layer may be opaque, and then the emission of electrons occurs from the same side from which the light falls, or semi-transparent, where the emission of electrons takes place on the opposite side to the illuminated surface. Due to the low work function of the photocathodes, they are made mainly of alkali metals - often cesium - and their compounds, including silver, oxygen and antimony, cesium-oxide and cesium-antimony. Depending on the type of the photocathode, it is sensitive in different spectral ranges, generally ranging from near infrared to ultraviolet.

An important quantity that defines the response of photocathodes is their quantum efficiency (QE) - defined as the ratio of the number of incident photons that were converted into electrons to the number of all photons which arrived to the photocathode [4]. The measurements can be done in the reflective mode or the transmission mode. The reflective mode allows to measure the QE of both opaque and semi-transparent photocathodes. The transmission mode enables the measurements of the QE as well as the transparency. It is targeted at semi-transparent photocathodes such as thin photocathode layers on crystals. The transmission mode reflects the way photocathodes will be used in the PicoSec project and is closer to the intended application.

Photocathodes are important in High Energy Physics and they are commonly used as the negatively charged electrodes in radiation detectors [4]. Opaque photocathodes are used in vacuum photodiodes where the electrodes have a shape of a cylinder or a sphere surrounding the anode. The photocathodes are placed inside the lamp. Semi-transparent photocathodes are mainly used in photomultipliers. Usually they are sprayed on the inside of the bulb. Moreover, photocathodes are used in accelerator physics to generate bright electron beams in devices like free electron lasers or ultrafast electron diffraction setups.

The motivation for the presented research into robust photocathodes is the idea of creating the PicoSec detector [2]. Prolonged operation in particle beams might lead to the photocathode's deterioration and a drop in the QE resulting in a decrease in timing capabilities. Therefore, detailed studies of the suitability and robustness of various photocathodes had been necessary and were conducted within the scope of this Master's thesis. Primary aims of the Master's thesis were to examine different photocathode materials as well as protective layers and carry out accelerated ageing studies of photocathodes under ion bombardment to find and choose a well-suited photocathode for the PicoSec detector.

The Master's thesis was carried out in the Gaseous Detector Development (GDD) laboratory within the EP-DT-DD group at CERN. Over a period of 12 months, I became familiarised with an existing characterisation setup and worked on its improvement and further development to optimise it for the presented studies. The scope of the experimental work included wavelength-resolved QE measurements in the VUV wavelength regime (130 - 200 nm), both in reflection and transmission modes, and accelerated ageing studies under X-ray irradiation. The main literature on the subject were the article about the PicoSec project [2] and textbooks [5] and [6] on the basis of which the analysis of the theory was made.

The Master's thesis plan is as follows. In the second chapter, theoretical knowledge of the interaction of particles with matter, necessary to understand the phenomena occurring in detectors, was organized. The third chapter is a compendium of knowledge about the gaseous radiation detectors, which presents their scopes of work and classification, as well as provides the most important information on Multi-Wire Proportional Chamber and Micro-Pattern Gaseous Detectors. Chapter four describes PicoSec MicroMegas project, which aims at the development of a precise-timing gaseous detector, and includes the new module designs. Chapter five is a detailed description of the ASSET experimental setup that was used to measure the samples. In the sixth chapter, the obtained results were presented and discussed as well as compared to the data contained in the publications. The last chapter is a summary of the conclusions drawn from this Master's thesis.

Chapter 2

Interaction of particles with matter

2.1 Interaction of charged particles with matter

The operation of any radiation detector depends on the way in which incident radiation interacts with the active medium of the detector itself [5]. An understanding of the response of a particular type of the detector must therefore be based on the knowledge of the basic mechanisms by which radiation interacts and deposits energy in matter. There is a fundamental difference in the interaction of charged particles and photons with matter. The description of the interaction of particles with matter presented in Subsections 2.1 and 2.2 of this work was prepared mainly on the basis of the information contained in Chapter 2 of the book [5].

The charged particles can be divided into two groups: heavy charged particles (protons, alpha particles, atomic ions) and fast electrons [5]. The heavy charged particles interact with matter mainly through Coulomb forces between their positive charge and the negative charge of orbital electrons within the material's atoms. They lose energy in the process of excitation and ionization of the atoms in many events of interaction and the lost energy has a quasi-continuous nature. As a result, a beam of heavy charged particles penetrates deep into the medium, decreasing in energy without changing its intensity. This happens until the distance travelled approaches a defined particle range, when the energy drops sharply to zero and the beam is stopped. In case of fast electrons, the energy loss is slightly different because of their small mass as well as indistinguishability and the fact that they lose energy primarily due to Bremsstrahlung,

2.1.1 Energy loss process

The mean energy loss per distance travelled of the heavy charged particles penetrating matter is described by the Bethe formula [7]. For a particle with speed v, charge z and energy E, travelling a distance x into a target of electron density n and mean excitation potential I, the relativistic version of the Bethe formula is defined by:

$$-\left\langle \frac{dE}{dx} \right\rangle = \frac{4\pi}{m_e c^2} \cdot \frac{nz^2}{\beta^2} \cdot \left(\frac{e^2}{4\pi\varepsilon_0} \right)^2 \cdot \left[ln\left(\frac{2m_e c^2 \beta^2}{I \cdot (1-\beta^2)} \right) - \beta^2 \right] \tag{2.1}$$

where:

- c - speed of light,
- β - ratio of the speeds: β = v/c
- ε_0 - vacuum permittivity;
- e - electron charge;
- m_e - electron rest mass.

The electron density of the material n can be calculated by:

$$n = \frac{\rho \cdot Z \cdot N_A}{A \cdot M_u} \tag{2.2}$$

where:

ρ - the density of the material;
Z - its atomic number;
A - its relative atomic mass;
N_A - the Avogadro number;
M_u - the Molar mass constant.

The Bethe formula was explained in detail in Chapter 2 of the book [5]. It shows that the energy loss strongly depends on the properties of a heavy charged particle that interacts with matter. The energy loss per distance travelled as a function of energy calculated for different heavy charged particles in silicon is presented in Figure 2.1. All the particles have the same tendency: the higher their energy, the smaller the energy losses and the particles penetrate deeper into the medium. Moreover, the heavier the particles, the more effectively they are stopped in the medium. In addition, the energy loss depends on the atomic number of the material that the particle penetrates. The energy loss per distance travelled as a function of energy calculated for alpha particles in different materials is presented in Figure 2.2. The graph shows that the bigger the atomic number of the material, the more effectively the particles are stopped.

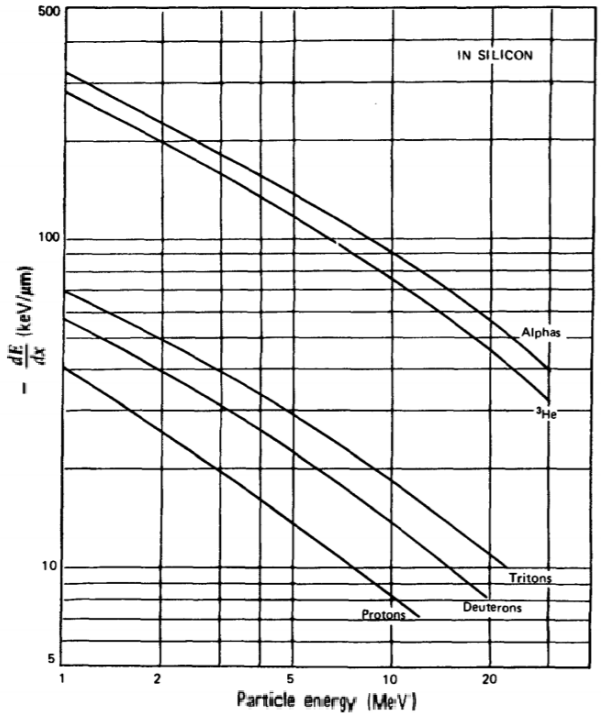

Figure 2.1: The energy loss per distance travelled as a function of energy for different heavy charged particles in silicon. All the particles have the same tendency: the higher their energy, the smaller the energy losses and the particles penetrate deeper into the medium. Moreover, the heavier the particles, the more effectively they are stopped in the medium. [5]

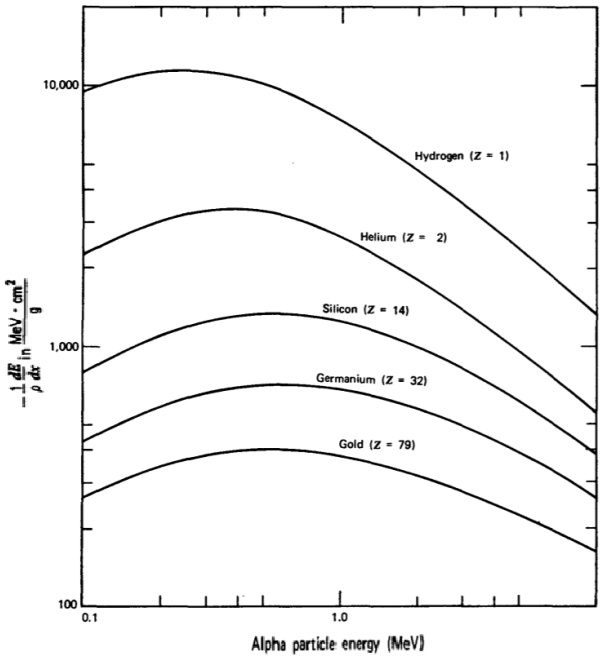

Figure 2.2: The energy loss per distance travelled as a function of energy calculated for alpha particles in different materials. The graph shows that the bigger the atomic number of the material, the more effectively the particles are stopped. The values are normalized by the density of the material [5]

The Bethe formula leads to the characteristic dependence known as the Bragg curve which describes the energy loss of a heavy charged particle along its distance of penetration [5]. When the accelerated charged particle travels through matter, the atoms of the material are ionized and the energy is deposited along the path. As the energy of the particle decreases, the interaction cross section increases and the so-called Bragg peak occurs. Thus, for most of the track, the energy loss is roughly inversely proportional to the square of the velocity of the particle, until the end of the track, where the characteristic peak occurs and the particle stops completely. An example of the Bragg curves for both a single alpha particle and parallel beam of alpha particles of the same several MeV initial energy traveling through air is shown in Figure 2.3.

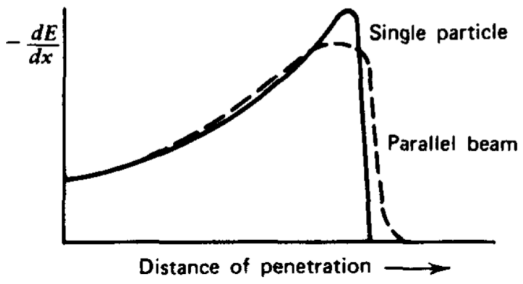

Figure 2.3: The Bragg curve describing the energy loss along the distance of penetration in air for both a single alpha particle and parallel beam of alpha particles of the same several MeV initial energy. [5]

When the distance travelled approaches a defined particle range, the energy drops sharply to zero and the beam is stopped. The definition of the particle range can be explained through the curve shown in Figure 2.4 which presents the number of alpha particles recorded after passing

through t thick absorbent [5]. There are two ways to determine the range of the alpha particles in the absorbent material from the plot. The most common version is the mean range, which is defined as the thickness of the absorbent that reduces the number of alpha particle to exactly half of its value in the absence of the material. Other definition is the extrapolated range, which is obtained by extrapolating the linear part of the end of the transmission curve to zero. The range of heavy charged particles with a given energy is therefore a unique quantity in a particular absorbing material.

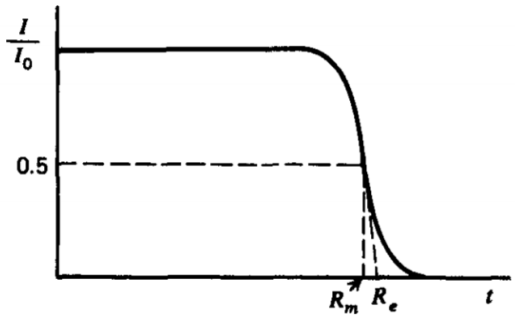

Figure 2.4: The number of alpha particles recorded after passing through t thick absorbent. I is the number of detected particles through an absorbent, while I_0 is the number of detected particles without the absorbent. The mean range R as well as the extrapolated range R_e are marked. [5]

2.1.2 Bremsstrahlung

Fast electrons, in comparison to heavy charged particles, lose their energy at a lower rate and follow a much more sinuous path through the absorbent [5]. The energy of fast electrons can be lost by radiative processes and by Coulomb interactions. The radiative losses can be generated at any position along the electron track and take the form of Bremsstrahlung. The description of Bremsstrahlung presented in this thesis was written on the basis of information taken from Chapter 2 of the book [5] and the website [8].

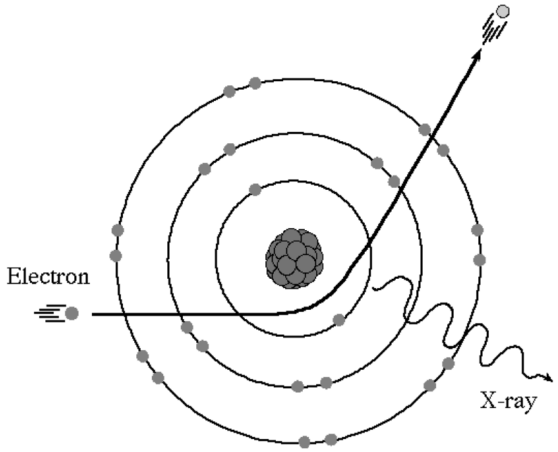

Figure 2.5: Bremsstrahlung produced due to the deceleration of an electron when it is deflected by an atomic nucleus. The moving particle loses its kinetic energy which is converted into radiation. [9]

A scheme of Bremsstrahlung is shown in Figure 2.5. During the process, the electromagnetic radiation is produced due to the deceleration (negative acceleration) of a charged particle (such as an electron) when it is deflected by another charged particle (such as an atomic nucleus). As a result, the moving particle loses its kinetic energy which is converted into electromagnetic radiation (i.e. a photon), therefore it satisfies the law of conservation of energy. The energy of a produced photon hf is:

$$hf = E_{k1} - E_{k2} \tag{2.3}$$

where:

h - Planck constant;
f - frequency of the photon;
E_{k1} - initial kinetic energy of the electron;
E_{k2} - final kinetic energy of the electron.

The spectrum of Bremsstrahlung is continuous and its intensity depends on the change of the energy of the braking particle: the higher the energy difference, the higher the intensity of the spectrum. What is more, increase of the change of the energy causes the shift of the intensity peak toward higher frequencies. If during the process the electron loses all of the kinetic energy ($E_{k2} = 0$), then its initial energy is converted into photon energy and the low-wavelength cutoff λ_{min} that depends only on the voltage V that the electron is accelerated through:

$$hf_{max} = E_{k1} = eV \quad \Rightarrow \quad h\frac{c}{\lambda_{min}} = eV \quad \Rightarrow \quad \lambda_{min} = \frac{hc}{eV}, \tag{2.4}$$

where:

c - speed of light;
e - elementary charge;
V - voltage that the electron is accelerated through.

The most common source of Bremsstrahlung is an X-ray tube, the scheme of which is shown in Figure 2.6. The heated cathode emits electrons that are then accelerated by a voltage V, reaching high energies. The vacuum inside the tube prevents the electrons from scattering on air molecules. The electrons hitting the anode are decelerated on it which causes the emission of X-rays. If the electrons have high velocities and the braking process is fast, the intensity of Bremsstrahlung is high and the peak is shifted toward higher frequencies.

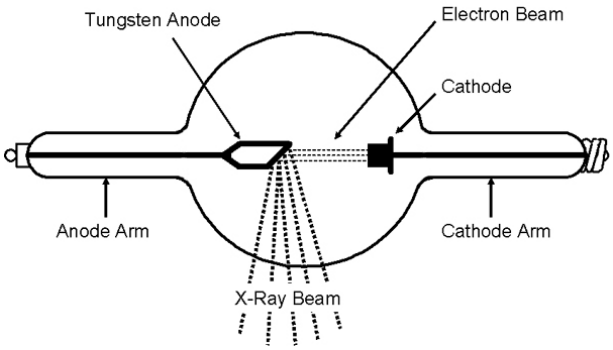

Figure 2.6: A scheme of an X-ray tube being a source of Bremsstrahlung [10].

The result of the operation of the device described above is a continuous spectrum of radiation. The most characteristic feature of Bremsstrahlung is the existence of the low-wavelength cutoff. It may happen that an accelerated electron, while hitting the anode, dislocates its electron, leaving a vacancy in the inner shell of an atom. The vacancy is then filled by an electron from the outer shell, releasing a photon in a pattern that is characteristic to each element. The spectrum of the X-rays emitted by an X-ray tube consists of continuous Bremsstrahlung with sharp peaks of characteristic radiation is presented in Figure 2.7.

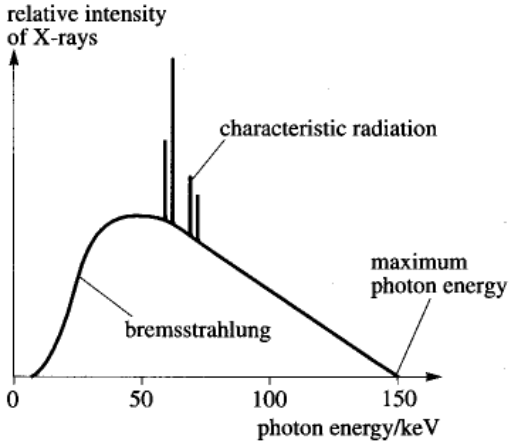

Figure 2.7: The spectrum of the X-rays emitted by an X-ray tube consists of continuous Bremsstrahlung with sharp peaks of characteristic radiation. [11]

2.1.3 Cherenkov radiation

Cherenkov radiation is another physical phenomenon used for the detection of charged particles [5]. It is electromagnetic radiation emitted when a charged particle (e.g. an electron) moves in a material medium at a speed greater than the phase velocity of light in that medium. The electromagnetic wave is emitted only in a specific direction lying at an acute angle to the direction of motion of the particle. The phenomenon is named for the Russian physicist Paweł A. Cherenkov, who shared the Nobel Prize in Physics in 1958 for its discovery [12]. The description of Cherenkov radiation presented in this thesis was prepared on the basis of information taken from Chapter 2 of the book [5].

A scheme of Cherenkov radiation is shown in Figure 2.8. When a particle with an electric charge moves through a dielectric medium, it polarizes atoms close to its path. After the particle passes, the atoms return to their previous states, emitting a quantum of energy. The condition for the formation of Cherenkov radiation is the appropriate velocity of the charged particle. It must be greater than the phase velocity of light in the substance through which the particle moves. This condition is expressed by the formula:

$$v > v_f = \frac{c}{n} \tag{2.5}$$

where c is speed of light in vacuum and n is a refractive index of the substance. The fronts of waves emitted at particular moments in points 0, 1, ..., 5 successively (see Figure 2.8 - black

circles) reach the conical surface (blue line, cone tip in point 5) simultaneously. At time t, the particle travels the distance from point 0 to point 5 - this path is vt (red line). At the same time, the light emitted by the particle at point 0 overcomes a certain distance to the conical surface $v_f t$ (green line). From Figure 2.8 it can be seen that:

$$sin\alpha = \frac{v_f t}{vt} = \frac{v_f}{v} = \frac{c}{nv} \tag{2.6}$$

As a result of interference, the radiation propagates further only in a direction perpendicular to the conical surface. The direction of radiation propagation creates an angle θ with the particle's movement direction, which can be determined from the relationship:

$$\theta = \frac{\pi}{2} - \alpha \tag{2.7}$$

thus, using the formula 2.6, the formula to calculate the angle θ is:

$$\theta = arccos\left(\frac{c}{nv}\right) \tag{2.8}$$

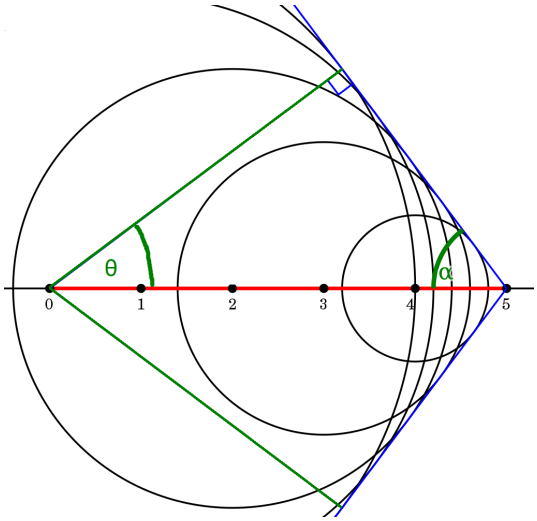

Figure 2.8: The geometry of the Cherenkov radiation shown for the ideal case of no dispersion. The particle moves left side to right, emitting spherical waves at points from 0 to 5 (black circles). The wave fronts simultaneously reach the conical surface (blue line, cone tip in point 5). At time t the particle travels the distance from point 0 to point 5 (red line). At the same time, the light emitted by the particle at point 0 overcomes a certain distance to the conical surface (green line) [13].

In elementary particle physics, Cherenkov radiation is used in counters for the detection and precise calculation of the velocity of high energy charged particles. A classic example of Cherenkov radiation is the characteristic blue glow around the core of an underwater nuclear reactor. The reactions taking place in the nuclear reactor result in the creation of high energy particles. The particles getting into the water (being the reactor coolant) cause the formation of Cherenkov radiation. However, this phenomena is very selective because the light can be emitted only if $v > v_f$. In gaseous detectors, such as RICH [14], it can be adjusted by varying gas pressure, thus, the threshold of acceptance can be easily tuned.

2.2 Interaction of photons with matter

There are three major types of the interaction of photons with matter: photoelectric effect, Compton scattering and pair production [5], presented in Figure 2.9. The total cross-section of interaction of a photon with an atom is equal to the sum of all three partial cross-sections:

$$\sigma = \sigma_f + \sigma_C + \sigma_p \tag{2.9}$$

where:

σ_f - cross-section of photoelectric effect;
σ_C - cross-section of Compton scattering;
σ_p - cross-section of pair production.

Depending on the photon energy and the target material, one of the three partial cross-sections can have a greater impact than the other two, which was explained in Chapter 2 of the book [5]. The relative yield of the three processes varies. At low photon energy values, the photoelectric effect dominates. At intermediate energies, Compton scattering dominates. Compton scattering also increases as the atomic number of matter decreases, which is why the dominance range is wider for light nuclei. At high energies, electron-positron pair production dominates.

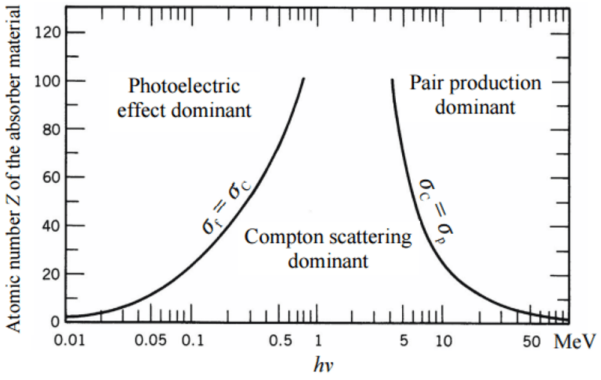

Figure 2.9: Three major types of the interaction of photons with matter: photoelectric effect, Compton scattering and pair production. The curves mark the regions where each effect is dominant [15].

The knowledge of the definition of the cross-section of the interaction allows to derive the relationship between the intensity of photons and the thickness of the absorber material. When photons of the same energy are collimated into one narrow beam and when the detector placed behind the material detects only photons that traveled through the medium without any interaction with it, then the dependence is an exponential attenuation of photons. During each of the interactions the photons are removed from the beam due to the absorbtion or scattering away from the detector direction. Thus, the cross-section can be described by a probability of occurance per unit path length in the material. Adding all the probabilities gives the so-called linear attenuation coefficient:

$$\mu = \tau_f + \tau_C + \tau_p \tag{2.10}$$

Gamma radiation intensity after attenuation can be calculated by using the following formula:

$$I = I_0 e^{-\mu x} \tag{2.11}$$

where:

I - intensity after attenuation;
I_0 - incident intensity;
μ - the linear attenuation coefficient (cm^{-1});
x - physical thickness of absorber (cm).

The equation shows that the linear attenuation coefficient increases with the atomic number of the absorber material and decreases with the gamma radiation energy. Dependence of gamma radiation intensity as a function of absorber thickness is shown in Figure 2.10.

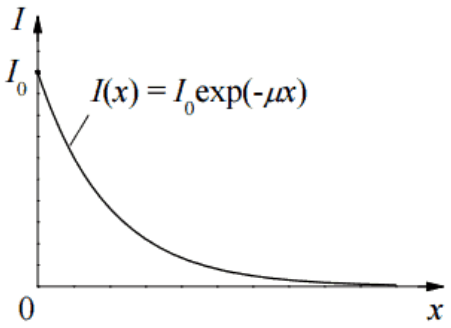

Figure 2.10: Dependence of gamma radiation intensity a function of absorber thickness [15].

2.2.1 Photoelectric effect

The photoelectric effect is the emission of electrons from a metal surface by the incident of electromagnetic radiation at a certain frequency [16]. The explanation of the photoemission contributed to the development of the wave-particle theory of matter, in which the objects of the microworld are simultaneously assigned wave and particle properties. For discovering the laws of the photoelectric effect, Albert Einstein was awarded the Nobel Prize in 1921.

The device for studying the photoelectric effect is shown in Figure 2.11 . Filtered, monochromatic light with the frequency f enters a vacuum tube and illuminates the cathode, causing the emission of electrons. A potential difference is maintained between the cathode (negative voltage) and the anode (positive voltage), causing an accumulation of electrons on the anode.

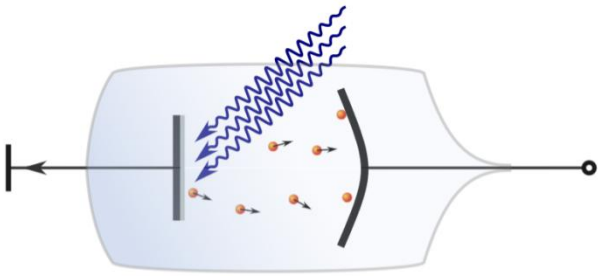

Figure 2.11: A scheme of the experiment to study the photoelectric effect. The light interacts with the cathode which results in the emission of electrons that are afterwards accumulated on the anode [16].

The description of the photoelectric effect presented in this thesis was written on the basis of information contained on the website [16]. According to Einstein's theory, energy located in a small volume of space remains localised also when it moves away from the source. The energy E contained in such a portion is equal to hf, where h is the Planck constant and f is the frequency. During the photoelectric effect, one photon is absorbed by one electron. The energy needed to liberate the electron from its atomic binding is called the work function W and it is a characteristic value for the material from which the cathode is made of. If $hf < W$, the electron does not leave the metal surface and the photoemission does not occur. If $hf \geq W$, the photoelectric effect is present and the electron gains the energy which is then converted into the work function and the rest of it - into kinetic energy E_K:

$$hf = W + E_k \tag{2.12}$$

The electrons emitted in the photoelectric effect are sometimes called photoelectrons. The kinetic energy of photoelectrons does not depend on the light intensity or duration of exposure, but only on its frequency. The emitted electrons can have a range of kinetic energies because the electrons in the cathode can occupy many different quantum states with different binding energies, as well as due to the energy losses that these electrons may incur when leaving the medium. When the photoelectron is emitted into a vacuum, the term external photoemission is often used, while when charge carriers are transferred between energy bands is distinguished as internal photoemission (also called photoconductivity). If the illuminated medium is gas, the phenomenon of photoionisation takes place.

The photoelectric effect is commonly used in devices which convert absorbed light into electricity and a measurable charge. A popular example is a photomultiplier tube (PMT) - a vacuum tube with a single-photon sensitivity with a coated photocathode and a series of electrodes - which is shown in Figure 2.12. The photocathode, made of specially selected materials that ensure a low work function to detect even at very low light levels, converts photons into photoelectrons which are afterwards multiplied on dynodes to provide a sizable output signal. The photoelectric effect is also used in devices like photodiodes, solar cells, image sensors, night vision devices, etc. as well as in a powerful technique to probe the structure of the electrons in a material called the angle-resolved photoemission spectroscopy (ARPES).

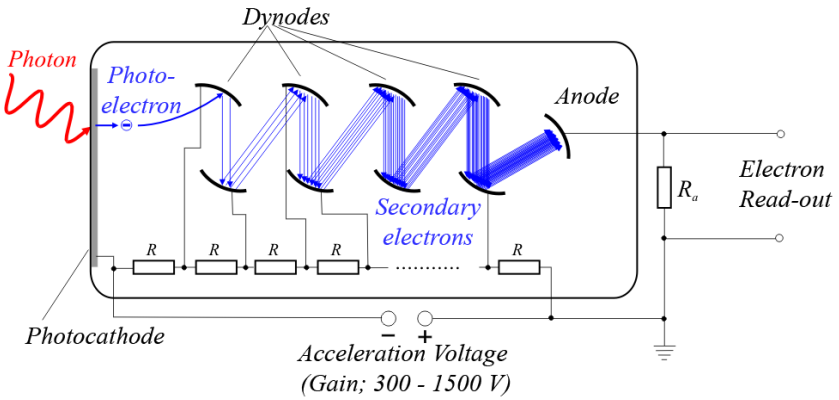

Figure 2.12: A principle of operation of the photomultiplier. An incident photon is converted into photoelectron on the photocathode which is then accelerated by the voltage inside the vacuum tube and multiplied on the dynodes in order to be detected on the output [16].

2.2.2 Compton scattering

At intermediate energies, another process - the Compton scattering, can take place [17]. The Compton effect is the scattering of high-frequency electromagnetic radiation (X-rays and gamma rays) on a charged particle, usually a free or weakly bound electron, resulting in a decrease in energy (increase in wavelength) of the radiation. During the process, part of the photon's energy is transferred to the electron, however, overall energy and momentum of the system are conserved. The Compton scattering was an essential experiment in the history of physics which convinced scientists that light can be treated as a stream of particles, therefore, it resulted in Arthur Holly Compton being awarded the Nobel Prize in Physics in 1927 for his discovery.

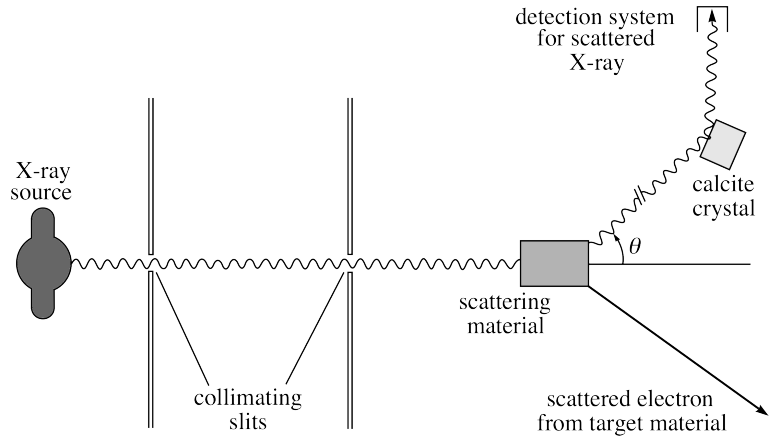

Figure 2.13: The experiment setup to study the Compton scattering. The incident photon is scattered on the target material, causing the electron's recoil [17].

The description of the Compton scattering presented in this work was prepared on the basis of information contained on the website [17]. The experimental setup for studying the Compton scattering is presented in Figure 2.13. An incident photon produced in an x-ray source passes through collimating slits and hits a scattering material and the Compton effect occurs: the incident photon transfers part of its energy to an electron and the scattered photon changes the direction of its original path, causing a recoil of the scattered electron from the target material. The energy of the scattered photon is measured by a system of a calcite crystal (using Bragg's law) combined with a detection system for scattered X-rays. The increase in wavelength of the scattered photon $\Delta\lambda$, called the Compton shift, depends on the photon scattering angle θ according to the formula:

$$\Delta\lambda = \lambda' - \lambda = \frac{h}{m_e c}\,(1 - cos\theta), \tag{2.13}$$

where: h - the Planck constant; m_e - the electron rest mass; c - the speed of light in vacuum. The quantity $h/m_e c$ is known as the Compton wavelength of the electron λ_C and it is equal to $2.43 \cdot 10^{-12}$ m. The wavelength shift formula can be converted to the expression for photon energy after scattering:

$$E' = \frac{hc}{\lambda'} = \frac{E}{1 + \frac{E}{m_e c^2}(1 - cos\theta)} \tag{2.14}$$

where: E - the energy of the incident photon.

All the above considerations were derived with the assumption that the charged particle is initially at rest. In such a situation, the energy of the scattered photon is always lower than the energy of the incident photon. Nevertheless, the phenomenon also takes place for fast-moving electrons. If the electron's energy is sufficiently high, part of it may be transferred to the photon, therefore, the energy of the scattered photon is greater than the energy of the incident photon. Because of this difference, it has come to be known as inverse Compton scattering. It should be emphasized, however, that this is still the same phenomenon, only observed from a different frame of reference.

Due to the fact that Compton scattering is the most likely type of interaction that of gamma rays and high-energy X-rays can undergo as they passes through matter, it plays an essential role in radiobiology, including radiation therapy. Compton scattering can be also used in material physics to study the wave function of electrons in matter in the momentum representation. In addition, the inverse Compton scattering is significant in astrophysics studies as well as in some synchrotron radiation facilities in nuclear physics experiments.

2.2.3 Pair production

Above a threshold of twice the total rest mass energy of a particle (at least 1.022 MeV for electron), pair production is likely to occur [18]. High energy neutral bosons bombarding the nucleus may create a subatomic particle and its antiparticle. Examples include a formation of an electron and a positron (as presented in Figure 2.14), a proton and an antiproton, or a muon and an antimuon. The process of creation a electron-positron pair from the energy of a photon was first observed in counter-controlled cloud chamber by Patrick Blackett, leading to the 1948 Nobel Prize in Physics.

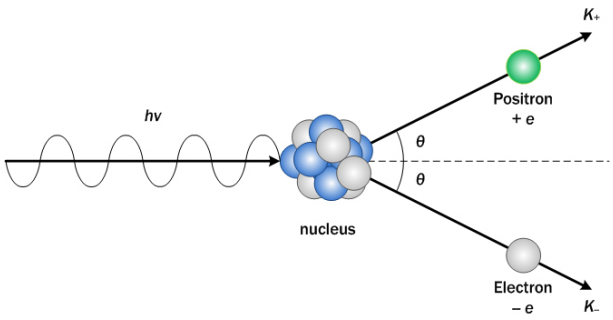

Figure 2.14: The process of pair production. High energy photon hits a nucleus causing a formation of an electron and a positron. [18].

The description of pair production presented in this thesis was prepared on the basis of information from the website [18]. In pair production, the energy of the photon is converted into masses of the created particles in accordance with Einstein's equation: $E = mc^2$, where E is energy, m is mass and c is the speed of light. The principles of conservation of both energy and momentum must be fulfiled. The formation of particles' pairs by photons occurs under two conditions: the photon's energy must be higher than the sum of the masses of the created particles, and an additional particle is involved in the process, which takes over the excess momentum, so that the principles of conservation of energy and momentum are fulfiled. These events can be observed in processes like the interaction of cosmic rays with particles of the atmosphere or in accelerators.

The cross section of pair production increases with photon energy as well as atomic number of the nucleus, and decreases with the mass of the produced particles. The process occurs most easily in a material medium containing large amounts of heavy elements, because the transfer of energy and momentum occurs through an electric field. The probability of pair production is proportional to the reciprocal of the square of the mass of the created particles. This means that even if the initial energy of the photon is sufficient to produce heavier particles, pairs of the lightest charged particles, i.e. electron-positron pairs, are by far the most frequently produced. The phenomenon of the creation of an electron and a positron by a photon in a material medium is sometimes called a photon conversion. If the process is reversed, it is called electron-positron annihilation.

Chapter 3

Gaseous radiation detectors

3.1 General information

Gaseous radiation detectors are instruments that allow to detect the presence of charged particles and measure ionising radiation [5, 6]. The principle of operation depends on three mechanisms: primary ionisation, electron drift, gas amplification. All of these processes take place in a gas-filled volume. A charged particle passing through the gas ionises some of the gas atoms or molecules that causes detachment of electrons from them. Due to the electric field in the gas volume, the electrons are transported to an anode and the positive ions to a cathode. The movement of the charged particles leads to creation of an electric signal that can be recorded by the electronic readout. In order to have a strong signal to noise ratio and making it easy to detect the particles, most gaseous detectors use electron avalanches - the multiplication of primary electrons in a high electric field by a cascade of secondary ionisation processes. The multiplication factor between the initial and the final amount of electrons is called the gain. The course of events involving the ionization of a gas and the acceleration of free electrons by an electric field, their collision with gas molecules, and in the following, with more free electrons, is called the Townsend avalanche or the Townsend discharge. The process of acceleration of the electrons and releasing extra electrons is sequential. The outcome is an avalanche multiplication that allows the gas to conduct electricity. The phenomenon requires a source of free electrons as well as a high electric field - without one of them, the discharge does not occur.

The use of gaseous radiation detectors requires the selection of appropriate operating conditions like drift field, biasing voltage and gas mixture [5, 6]. The drift and amplification processes depend on the reduced electric field which takes into account environmental variations. The most common base for gas mixture is a noble gas that does not react with the amplification structure, which could cause ageing of the detector. The typical noble gas used is Ar, but also He, Ne, Xe or Kr are used for specific applications. In addition, an admixture of a molecular gas, e.g. CH_4, CO_2, is usually used to absorb photons produced in the gas amplification process to avoid feedback - the so-called quenching process.

Gaseous radiation detectors were among the first tools to track particles' trajectories. During the evolution of physics and associated experimental requirements, scientists developed and improved the performance of gaseous detectors and invented new ways to technologically exploit electron avalanche mechanisms. The possibility to equip large area with gaseous detectors with reasonable area to cost ratio as well as radiation hardness and low material budget on the active medium are among their important features. These advantages make gaseous detectors an attractive choice for many applications including experiments at Large Hadron Collider.

3.2 Gaseous detection regions

The relationship of the gaseous detection regions is shown in Figure 3.1 [6, 19]. The diagram presents the relative level of ion current as a function of voltage applied between an anode and a cathode for a wire cylinder gaseous detector that is subjected to ionising radiation. This covers the practical areas of operation of the ionisation chamber, the proportional counter and the Geiger-Müller tube. Alpha and beta particles are plotted to demonstrate the impact of different densities of ionising energy loss, however, the same principle applies to all forms of radiation.

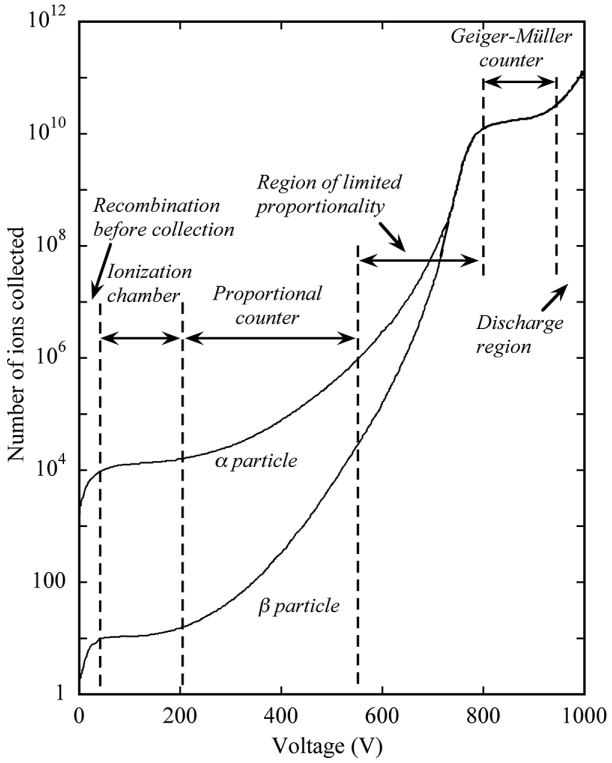

Figure 3.1: A diagram of different detection regions for a wire cylinder gaseous radiation detector. Alpha and beta particles are plotted to demonstrate the impact of different ionising energies. [6].

There are five important operation regimes for gaseous radiation detectors [6]:

- At very low voltages, charges start being collected, but recombination is still a dominant process. Thus, primary electrons are lost of the drift regions and the number of electrons reaching the anode structure is lower than the original number of primary charges.
- At higher electric fields, full charge collection begins and the detector starts to operate in the ionisation mode. In the ionization chamber region, alpha particles are more ionising and they produce more current than beta particles, but a distinction between the particles is impossible. Due to the problem that usually signal to noise ratio is too low, the ionisation chambers can be only operated in the current mode, so they give the amount of charge per second but not individual events.
- Increasing the voltage further, the electric field gets large enough to initiate an electrons avalanche mechanism and the detector operates in the proportional mode. As the proportional counting region, alpha particles produce more current than beta particles and a distinction between these two pulses is possible, because signal to noise ratio is high

enough, so the proportional counter is not operated in the current mode. As a result, the number of electrons at the end of the process is proportional to the initial number.

- At even higher voltages, this proportionality is steadily lost due to the electric field distortions and eventually the detector starts to operate in the Geiger-Müller mode. In the Geiger region, there is no distinction between alpha and beta particles because each individual ionisation event in the gas causes the same current output. The output is the same, because all of the energy stored in the detector is released, so each event that triggers this will give the same signal.
- Finally, the electric field is so high, that the detector enters the discharge region which can be destructive and therefore not suitable for operation (especially when self sustained discharges due to feedback processes occur).

3.3 Classification of gaseous detectors

Based on the classification of operation regimes presented above, there are three basic types of gaseous detectors: ionisation chambers, proportional counters and Geiger-Müller tubes [5, 6]. All gaseous detectors have similar designs consisting of two electrodes separated by gas, however, each of them measures the total number of collected electrons and ions using a different method. Main factors that determine the detector's response to ionising radiation are strength of the electric field between the electrodes, type of the gas mixture and its pressure. Classification of gaseous detectors presented in this thesis was written mainly on the basis of information taken from the books [5, 6] and the website [20].

3.3.1 Ionisation chamber

An ionization chamber is the simplest of gaseous radiation detectors [5]. It operates at low values of the electric field, therefore no electron multiplication takes place. In the ionisation chamber region, alpha particles are more ionising and they produce more current than beta particles, but a distinction between the particles is impossible due to the operation in the current mode which is not capable to recording individual events.

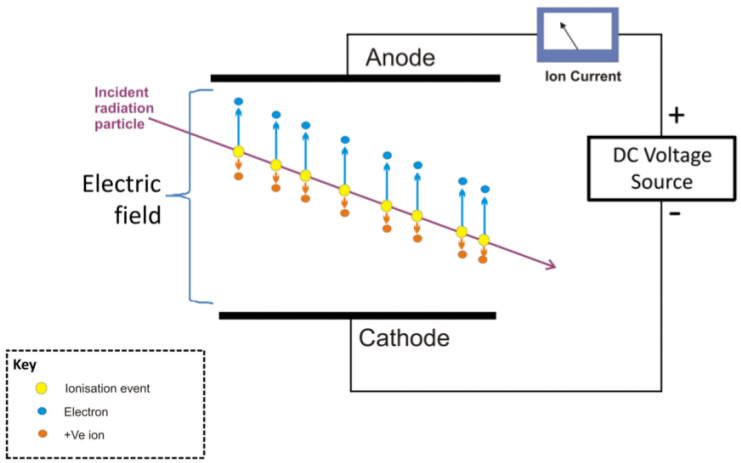

Figure 3.2: A schematic diagram of the ionisation chamber operation. Ions and free electrons are created and the applied electric field results in drifting the charge carriers towards the electrodes [20].

The description of the ionisation chamber presented in this thesis was written on the basis of information taken from the book [5] and the website [20]. A schematic diagram of the ionisation chamber operation is shown in Figure 3.2. The creation of electron-ion pairs generates ionised atoms or molecules and free electrons. The electric field makes the electrons drift towards an anode and the positive ions towards a cathode. The electric field must be strong enough to separate electrons from ions to not lose charge due to recombination. The ion current does not depend on the applied voltage while the detector is being operated in the ionisation chamber region. Since the charge is usually very small, the ionisation chambers are not suitable for recording individual particles, but they are used to detect high-intensity particle fluxes. They have good uniform response and allow for an accurate reading of total ionisation energy. Because of the simple concept, no statistical fluctuations during amplification as well as no charging up due to purely metallic electrodes, the ionisation chambers are very stable (in comparison to detectors with multiplication), therefore, they can be used for dosimetry.

3.3.2 Proportional counter

A proportional counter operates at higher values of the electric field compared to an ionisation chamber and it can generate avalanches of electrons [5, 6]. The main advantage is that the signal amplitude can be increased in a proportional way, therefore, one can get more signal but it still reflects proportionally the energy deposited by the incident radiation. The proportional counter has the ability to measure energy of radiation and differentiate between particles, be used for energy resolved imaging as well as make accurate measurements of the amount of charge deposited in the active volume of a detector by incident radiation.

The description of the proportional chamber presented in this thesis was prepared on the basis of information contained in the references [5, 6, 20]. Practical implementations of proportional counters are divided into two or more distinct ionisation regions with different electric field strength. The first region is located between the cathode and the amplification stage and it is called the drift region. In this part of the detector, the creation of number ion-electron pairs proportional to the amount of deposited energy takes place, causes the positive ions drift to the cathode and the electrons to the anode. The second region is located in the vicinity of the anode and it is called the avalanche or multiplication region. The anode is usually made of a thin wire around which the strong electric field is applied. Electrons approaching the wire gain their energy and ionise the subsequent atoms. The Townsend avalanches process takes place and results in signal amplification; the size of the recorded signal is proportional to the amount of the originally deposited charge, which is shown in Figure 3.3.

It is substantial to separate in the drift region and the amplification region. If the amplification takes place in the drift region, it would result in signal amplitude being dependent on depth of ionisation. That is because the path available for avalanche multiplication would be longer or shorter if the ionisation takes place farther or closer from the anode, respectively. By separating these regions, incident particles create primaries electrons in the drift region, they all drift to the amplification region and experience the high electric field region for the same distance, causing proportional avalanche multiplication.

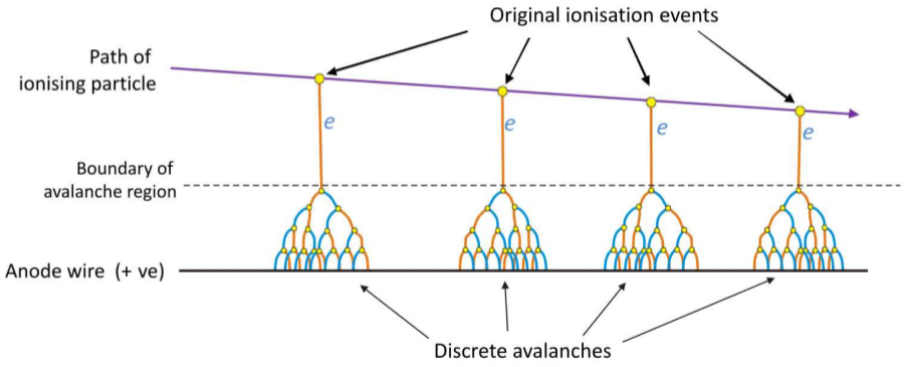

Figure 3.3: Generation of the Townsend avalanches in the proportional counter [20].

3.3.3 Geiger-Müller tube

A Geiger-Müller tube is the primary component of a Geiger counter [5, 6]. It operates at reduced pressure to allow using lower bias voltages; otherwise impractically high voltages would be required. The Geiger-Müller tube has no ability to distinguish between alpha and beta particles because each individual ionisation event in the gas causes the same current output.

The description of the Geiger-Müller tube presented in this thesis was written on the basis of information contained in the books [5, 6] and on the website [20]. The Geiger counter is constructed similarly to a proportional counter, however, the voltage on the anode wire is higher, selected such that each ion-electron pair causes an avalanche. Moreover, due to the emission of UV photons, multiple avalanches are created that spread along the anode wire, so the adjacent gas volume ionises even from a single ion-electron pair event. Generation of the spread of the Townsend avalanches caused by UV photons in the Geiger-Müller tube is shown in Figure 3.4. The current signals generated by the ionising events are transmitted to electronic readout which can measure count rate or radiation dose.

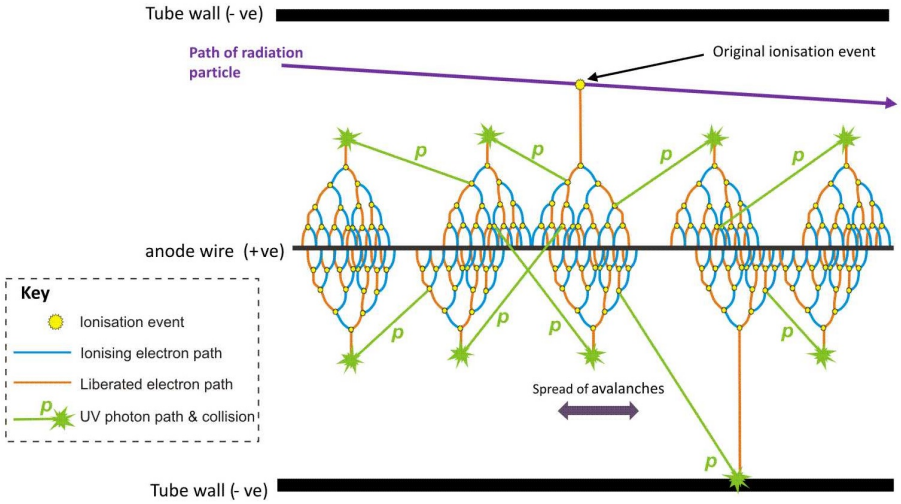

Figure 3.4: Generation of the spread of the Townsend avalanches caused by UV photons in the Geiger-Müller tube [20].

3.4 Multi-Wire Proportional Chamber

An important example of proportional counters is a Multi-Wire Proportional Chamber (MWPC) invented and developed by Georges Charpak in 1968, while at CERN in Switzerland [21]. This invention resulted in him being awarded the Nobel Prize in Physics in 1992.

The description of the MWPC presented in this work was prepared on the basis of information contained in the book [6] and on the website [22]. The MWPC detects charged particles and photons and can provide spatial information of interaction positions through multiple readout channels. It is built of a set of thin, parallel anode wires assembled between two cathode planes. The wires are usually biased with positive high voltage and the cathodes are at ground potential. Field lines near the anode wires are shown in Figure 3.5. The chamber is filled with a gas mixture so that particles passing through it can ionize gas atoms. The ionised particles are accelerated by the electric field. The positive ions drift to the cathode and the electrons - to the wires, resulting in the Townsend avalanche. The electron current is collected on the nearest wire and the ion charge is proportional to the charge of the original particle. By calculating signals from all the wires, the trajectory of the particle can be reconstructed. The spatial precision of the detector depends on the wires pitch.

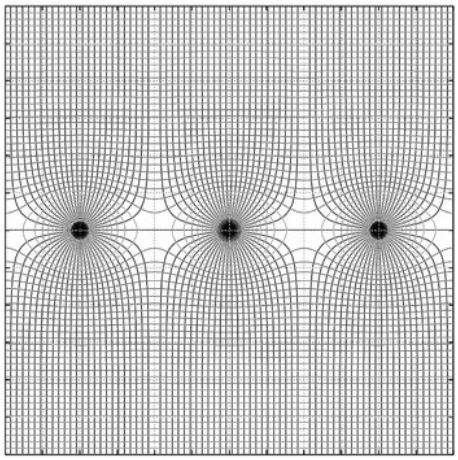

Figure 3.5: Field lines near the anode wires in the MWPC [6].

Due to its millimeter-scale spatial resolution, the detector quickly replaced bubble and spark chambers: the use of a proper electronic readout caused the data acquisition from the MWPC to be much faster than the existing techniques [6]. Moreover, the MWPC makes it possible to determine the position of an incoming particle using only one detector instead of using arrays of proportional counters. Nevertheless, the larger demand of high energy physics experiments highlighted the limitations of this detector. The most substantial disadvantages of the MWPC are limited spatial resolution due to mechanical difficulty with assembling wires precisely as well as electrostatic repulsion between wires and limited rate capability due to the space charge effect and aging of the wires.

3.5 Micro-Pattern Gaseous Detectors

Micro-Pattern Gaseous Detectors (MPGDs) are a group of gaseous radiation detectors consisting of structures with electrode geometries on the scale of tens of micrometers [6, 23]. A main factor in the popularity of the MPGDs was the development and the advancement of industrial Printed Circuit Board (PCB) structuring techniques. Precise photolithography allowing the production of flat structures at the μm level enabled the MPGDs to be manufactured.

The description of the MPGDs presented in this thesis was written mainly on the basis of information from the references [6, 23]. The MPGDs can be operated in different gas fillings (e.g. mixtures of Ar/CO_2 or Ar/CF_4), including pure noble gases (e.g. mixtures of Ar/Ne or Ar/Xe). The main advantages of the MPGDs, in comparison to previous gaseous detectors, include not only their count rate capability, but also time and position resolution. Moreover, MPGDs are distinguished by granularity (which is connected to the spatial resolution), stability and radiation hardness. In addition, building a detector with surface structuring techniques is simpler than stretching or fixing many wires precisely, which translates to better spatial resolution of MPGDs. The different types of the MPGDs vary in the method of creation of the strong electric field region used for amplification. Examples of the MPGDs include the Micro-Strip Gas Chamber (MSGC), the Gas Electron Multiplier (GEM) and the the Micro-Mesh Gaseous Structure (MicroMegas).

3.5.1 Micro-Strip Gas Chamber

The first MPGD was the Micro-Strip Gas Chamber invented by Anton Oed in 1988 [24]. The principle of operation of the MSGC is similar to the MWPC, however, instead of thin wires, it consists of very narrowly spaced micro-strips structured on an insulating substrate [6, 23]. The comparison between images of the MWPC and the MSGC is shown in Figure 3.6. The strips are alternatively supplied with positive and negative voltages. The high electric field, which is required to create avalanches, is generated between adjacent strips as shown in Figure 3.7. This type of detector gives the opportunity to increase the spatial resolution, because it can be structured more finely than wires can be placed. Moreover, the space charge effect can be reduced due to the fast collection of the ions by the nearest cathode strips. While the rate capability of the MWPC is limited by the space charge effect, the fine granularity of the MSGC increases the limit by two orders of magnitude [23].

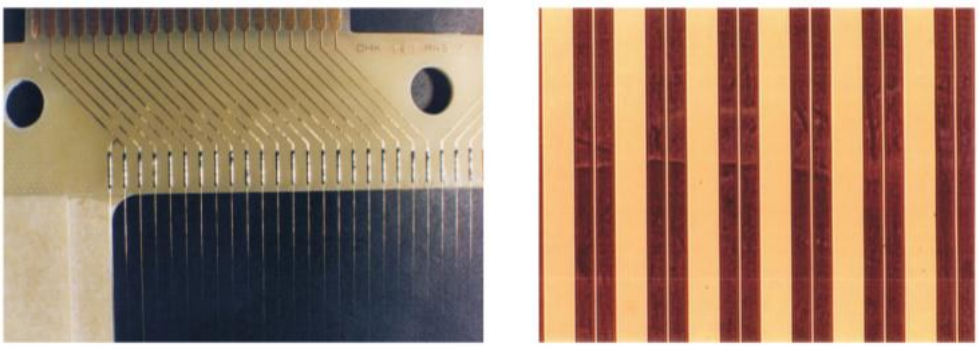

Figure 3.6: Left: wires of the Multi-Wire Proportional Chamber (MWPC) soldered to a frame. The typical separation between the anode wires (the "pitch") is few mm. Right: microscope image of the Micro-Strip Gas Chamber (MSG). The pitch here is approximately hundreds of μm [23].

Due to its high rate capability, the MSGC became an excellent detector for numerous applications [6, 23]. On the other hand, the development of the MSGC also pointed out some new limitations. One of them is charging up of insulating surfaces that locally changes the field shape and limits the stability in time. Another issue is the problem of discharges that made MSGCs suffer seriously. The discharges are induced by strongly ionising particles and can significantly damage the thin anode strips. In 1997 the Gas Electron Multiplier (GEM) was introduced by Fabio Sauli as a pre-amplification stage for the MSGCs [25]. This permitted the MSGC to operate at a lower voltage that contributed to reduce the probability of discharges.

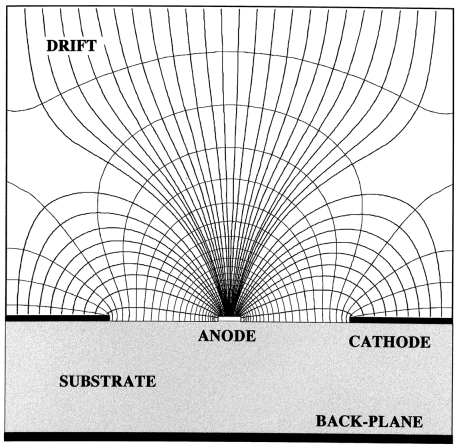

Figure 3.7: MSGC electric field in the vicinity of the strips [6].

3.5.2 Gas Electron Multiplier

The Gas Electron Multiplier is a thin, metal clad polymer foil consisting of many holes in a hexagonal pattern with a standard pitch of 140 μm [6, 23, 25]. The basic material used in the GEM production process is a polyimide film with two layers of metal (commonly copper) on opposite sides. The holes in the foil are created by using a chemical etching technique and have a diameter of about 70 μm. The electron microscope view of a GEM foil is shown in Figure 3.8.

The principle of operation of the GEM detector is described below [6, 23, 25]. The GEM foil is inserted between two electrodes applied with suitable bias voltages, providing the potential difference. A high dipole field develops inside the holes and around them, focusing the field lines between the electrodes as shown in Figure 3.9. The primary electrons created by ionisation in the drift gap are attracted into the holes where the Townsend avalanches occur and the electrons generated in this process are transferred into the lower region. The GEM foil acts as a charge amplifier in which each hole works as an independent proportional counter and the original ionisation pattern is preserved (but it is more discrete by the pattern of the holes). The gain depends on the voltage across the GEM, the gas mixture and its pressure as well as the length of the avalanche. Because of the high density of holes, the gain is not affected by space charge up to very high radiation fluxes [26].

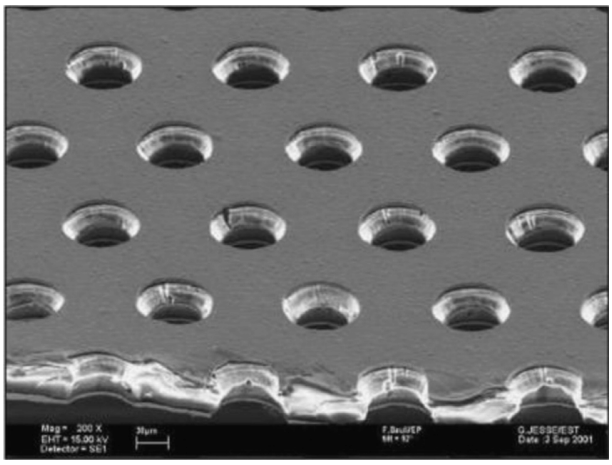

Figure 3.8: The electron microscope view of a GEM foil. The holes' diameter is about 70 microns and the standard pitch is 140 μm [6].

A useful feature of the GEM design is that the structure composed of several foils separated by transfer gaps can be assembled and several multiplication stages can be cascaded within the same detector [6, 23, 25]. The overall gain of a multiple structure, named the effective gain, corresponds to the product of gains of each foil separately. In comparison to the "normal" gain, the effective gain takes into account also collection, transfer and extraction efficiencies into the GEM foils and between them. High total gains can be reached with each foil at much lower voltage than for a single device, noticeably increasing the reliability of the detector. The structure built of three GEM foils, the so-called triple-GEM, assures the reliability necessary in harsh beam conditions. However, even a multi-GEM structure is limited by the so-called Raether limit - if local charge density exceeds this limit, it leads to electric breakdowns, including discharges. A schematic design of the triple-GEM detector is shown in Figure 3.10.

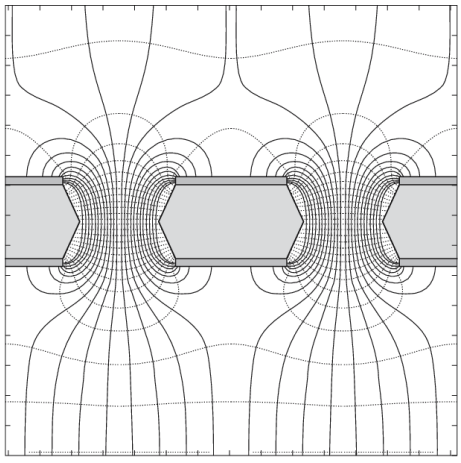

Figure 3.9: GEM electric field near holes in typical operating conditions [6].

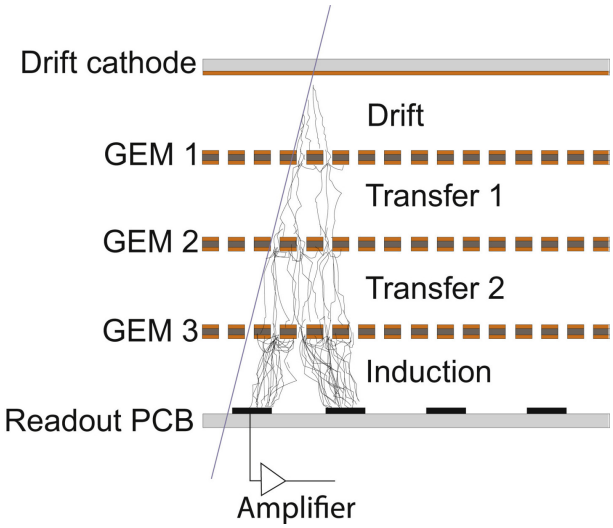

Figure 3.10: A schematic design of the triple-GEM detector, including the Townsend avalanches [27].

3.5.3 MicroMegas

The successful development of multi-wire and micro-strip structures has helped in the research of gaseous detectors that use amplification mechanism in uniform electric fields [6, 23]. Parallel plate counters that are mechanically sturdier have inherently better energy resolution and higher rate capability. Nevertheless, unstable operation caused by the exponential dependence of the gain on the gap as well as the sensitivity to defects result in limitations of their applicability. It was noticed, however, that in thin sub-millimeter gaps, because of saturation of the Townsend coefficient at very high fields, large gains can be reached. This observation has triggered the development of the MicroMegas [28].

The detector consists of a thin, stretched metal grid (micro-mesh) supported at the distance of 50 to 150 microns above the anode [6, 23, 28]. Primary electrons created in the drift region are collected into the amplification region between the mesh and the anode. The uniformity of the multiplying gap is ensured by regularly spaced insulating support pillars created during the manufacturing process. A schematic design of the MicroMegas construction and its electric field lines are shown in Figure 3.11 and Figure 3.12, respectively. The narrow gap and very high field cause positive ions being transported very rapidly. Signals on the anodes are induced fast with an ion tail that depends on the width of the gap. Due to the lower drift field, most ions are collected on the cathode mesh and the charge backflow into the drift gap is reduced. High energy resolution and high gain achievable by the MicroMegas make the device able to efficiently detect and localize radiation with high sensitivity.

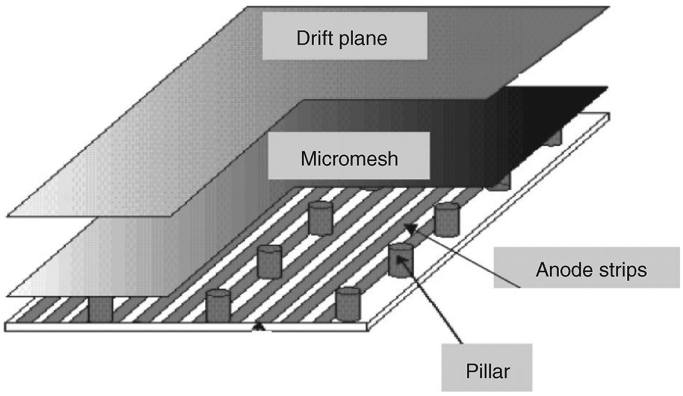

Figure 3.11: A schematic design of the MicroMegas construction, including insulating pillar spacers across the multiplying gap inserted during manufacturing electrodes [6].

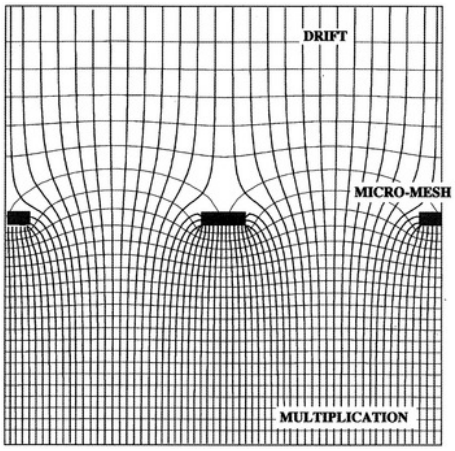

Figure 3.12: Electric field in the MicroMegas [6].

Chapter 4

PicoSec MicroMegas: Precise timing with gaseous detectors

4.1 PicoSec detection concept

The challenges of future High Energy Physics experiments, including high-pile-up environments expected in the High-Luminosity Large Hadron Collider (HL-LHC) [1], have aroused intense interest in the development of technologies for precise detectors with high time resolution. Conventional MPGDs would be great candidates for that technologies, however, their limitations include time resolution is on the scale of nanoseconds due to interaction depth differences on the millimeter-scale in the active detection volumes. The necessary time resolution is of the order of ten of picoseconds, therefore, within the PicoSec MicroMegas collaboration [2], a precise-timing gaseous detector is being developed. The concept consists of a "two-stage" MicroMegas detector coupled to a Cherenkov radiator coated with a photocathode, as shown in Figure 4.1. The radiator is a MgF_2 crystal with light transmission above 115 nm, while the photocathode is CsI with high quantum efficiency for photons below 200 nm. This setup guarantees a bandwidth for the production and detection of Cherenkov light in the vacuum ultraviolet (VUV) wavelength range. A charged particle passing through the radiator creates and emits UV photons that are converted into primary electrons at the photocathode. Because all the photoelectrons are created at the same location, they drift together and create a very short pulse. There is no uncertainty about the location of the photoelectrons production, so precise timing is achievable.

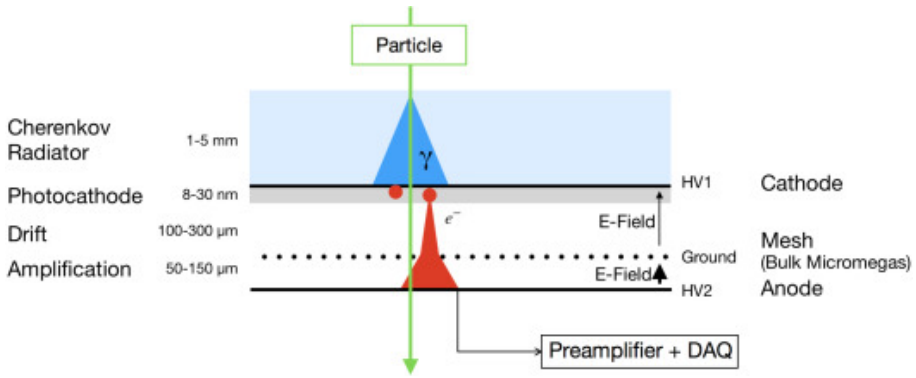

Figure 4.1: The PicoSec detection concept. A charged particle passing through the Cherenkov radiator creates a cone of UV photons that are partially converted into primary electrons at the photocathode. The primary electrons are pre-amplified in the drift region and they are multiplied in the amplification gap below the mesh due to the high electric field [2].

Due to the high electric field in the drift region (~20 kV/cm), the photoelectrons are pre-amplified. Afterwards, the primary electrons partially traverse the mesh and they are amplified in the multiplication gap under the influence of the high electric field (~40 kV/cm). Operated in the 80% Ne + 10% C_2H_6 + 10% CF_4 gas mixture, the readout can achieve gains up to $10^5 - 10^6$, which is sufficient to detect single photoelectrons and the electron drift velocity is high enough for a fast collection of charge. The amplified electrons induce a fast signal at the anode referred to as the electron-peak (with a risetime of about ~0.5 ns), while the movement of the ions created in the multiplication gap in the opposite directions produces a slower component-ion-tail (~100 ns), as shown in Figure 4.2.

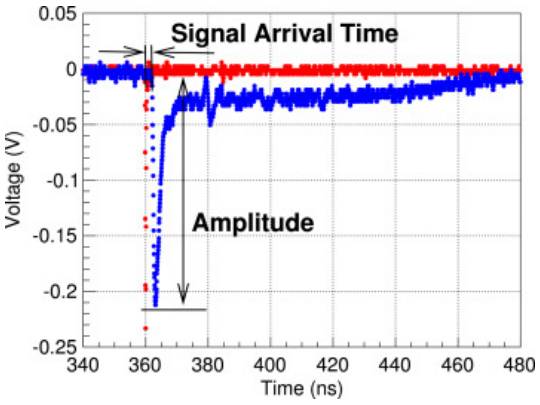

Figure 4.2: An example of an signal induced from the PicoSec detector created by 150 GeV muons (blue points), recorded along with the timing reference of the microchannel plate MCP signal (red points) [2].

4.2 Developments towards applicable detector

The first prototype of the detector demonstrated high timing resolution on small scale [2], however, to make the concept appropriate to physics applications, several developments are required. Developments towards applicable detectors include: finding a robust photocathode, scaling up the detector and minimisation of the deformation to improve the planarity.

The first development involves the photocathode which is in the core of the PicoSec detector. The prototype of the detector uses a semi-transparent cesium iodide (CsI) photocathode [2], but the degradation of CsI quantum efficiency (QE) is a concern in the development of this concept. Prolonged operation in particle beams might lead to a deterioration of photocathode materials and decreases their QE, resulting in a decrease in timing capabilities as well as detection efficiency. Therefore, detailed studies of the suitability and robustness of different photocathode materials are necessary. This includes the characterisation of different photocathode materials as well as accelerated ageing studies of photocathodes under ion bombardment to find and choose a well-suited photocathode for the PicoSec detector. This thesis is focused on the measurements of 4 different photocathode materials including: CsI, diamond like carbon (DLC), boron carbide (B_4C) and hydrogenated nanodiamonds (HND). An example of photocathodes with different thickness of the material is presented in Figure 6.2. The detailed studies of the photocathodes are described in the next chapters.

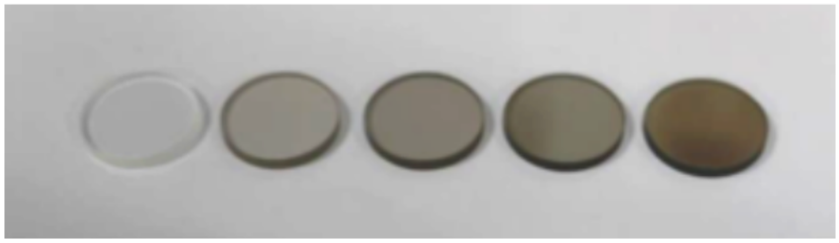

Figure 4.3: DLC photocathodes of different thickness produced at University of Science and Technology of China (USTC) [29]

The second development is scaling up the detector for future coverage of large area detectors. Figure 4.4 shows: a first prototype which was a single pad, a multi pad with 19 hexagonal channels and a new PicoSec module design with 100 square channels and an active area increased almost 10 times in comparison to the previous version of the detector. Within this thesis two different housing designs for the new PicoSec module are presented.

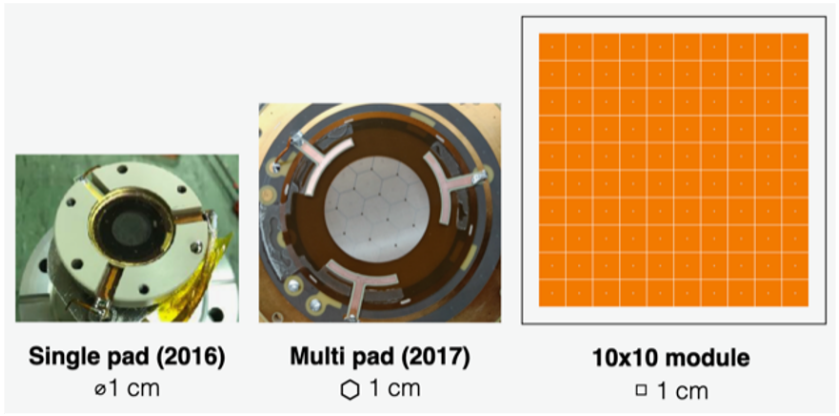

Figure 4.4: Scaling up the detector. From the left side: a first prototype, a multi pad with 19 hexagonal channels and a new PicoSec module design with 100 square channels.

The last development is the minimisation of the deformation to improve the planarity. In the first multi-pad PicoSec detector, the deformations in the range of 30 μm in the active area were observed [2]. This resulted in a time error and non-uniform response of the detector. To have uniform detector response, a uniform gap over the entire active area and the deformation below 10 μm is needed. However, this thesis does not cover this development as it was outside the scope of my work.

4.3 New PicoSec module designs

The new PicoSec module has two different housing designs in order to test different parameters and functionalities. The first approach is an aluminium housing which was made to evaluate the planarity of the detector. The second approach is a sealed housing to build a compact, clean, hermetically closed detector for high gas quality for prolonged sealed operation.

4.3.1 Aluminium housing

The aluminium housing was built to improve the planarity of the detector. Its cross section is presented in Figure 4.5. The aluminium housing consists of two parts: walls and a flange with a matrix of holes milled in the flange to transmit UV light and support the radiator during pumping. Inside the housing there is a radiator: a flat MgF_2 crystal to improve detector's planarity. Above the radiator, there are four copper spacers and a MicroMegas PCB made of ceramic boards: its planarity was improved thanks to simulations and optical planarity measurements during the production. Next parts is a matrix of pogo pins: the connectors are not fixed to the MicroMegas PBC in order to avoid deformations, instead, they are soldered to the outer PCB and pressed against the MicroMegas PCB. On the top of the outer PCB the electronics boards are coneccted. Figure 4.6 shows 3D drawings of the aluminium housing designed using Fusion 360 software. The actual elements were produced at the Thin Film and Glass workshop at CERN (M. van Stenis).

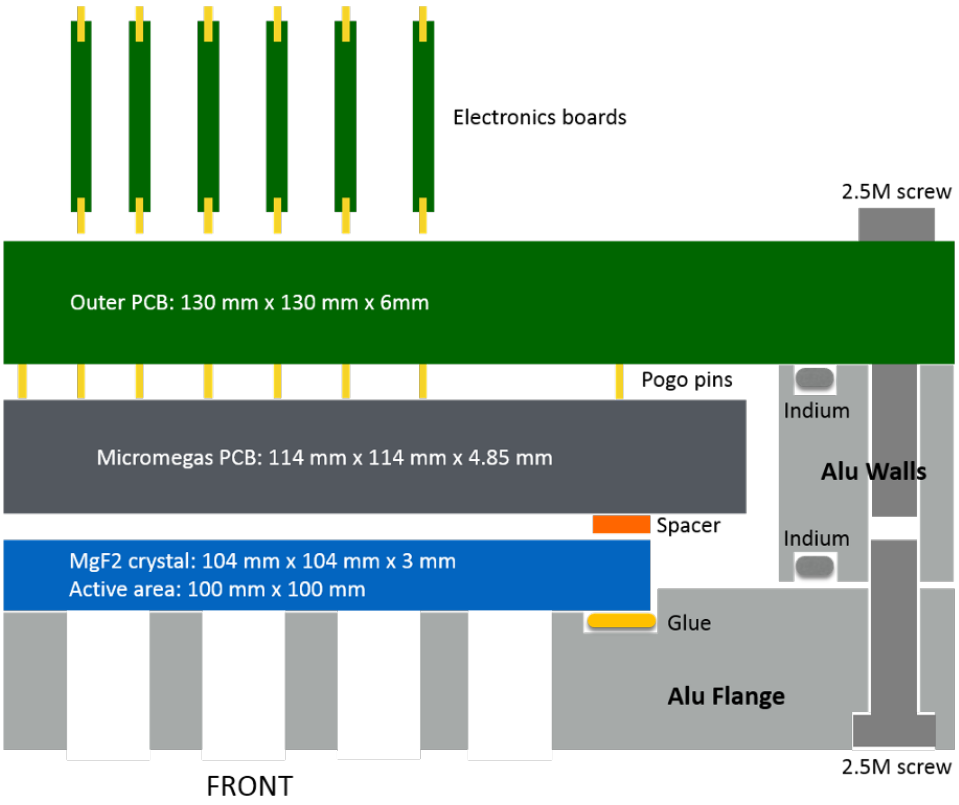

Figure 4.5: A cross section of the aluminium housing. The housing consists of two parts: walls and a flange. It is built of flat components: the radiator and PCBs, to improve the planarity of the detector.

The routine of the aluminium housing's first assembly is presented in Figure 4.7. In the first trial a piece of glass was used instead of the radiator and a mock up MicroMegas PCB without a mesh. The first step was to glue the glass to the aluminium flange and screw the flange to the walls with an indium seal in between (first 2 photos in the first row). Then, the spacers were soldered to the bottom side of the MicroMegas PCB (4 next photos in the first row) and they were placed inside the housing (first 2 photos in the second row). In addition, few pogo pins were soldered to the outer PCB from the inside and some gas connectors for pumping and filling

were attached to this PCB from the outside (second 2 photos in the second row). At the end, the outer PCB was screwed to the aluminium walls, again with an indium seal in between (2 last photos in the second row). Preliminary tests showed that the detector held the pressure well and the achieved max voltages were satisfactory.

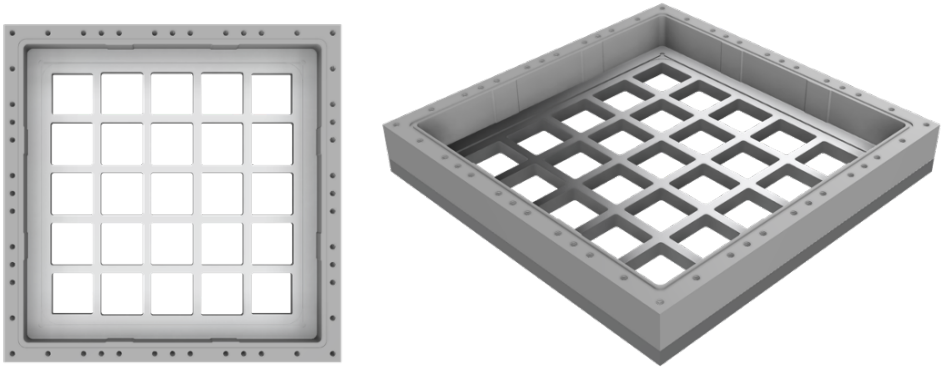

Figure 4.6: 3D drawings of the aluminium housing: left - top view; right - side view.

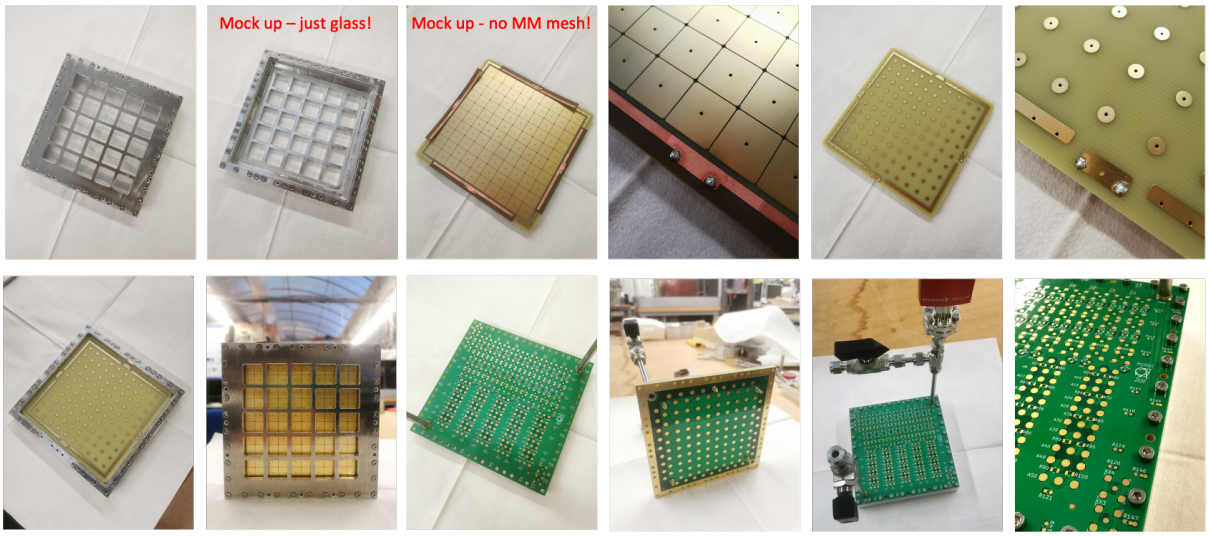

Figure 4.7: The routine of the aluminium housing's first assembly (described in detail in the text). The trial was conducted using some mock-up components.

4.3.2 Sealed housing

The sealed housing was built to have a compact, clean, hermetically closed detector for high gas quality. A cross section of the sealed housing is shown in Figure 4.8. It is similar to the aluminium housing, however, in this concept there are titanium housing parts, a ceramic board with brazed invar pins instead of the outer PCB and extra sapphire windows on the bottom. The main difference between these two approaches is the sealed housing's assembly procedure which

uses different joining steps. Figure 4.9 presents 3D drawings of the sealed housing designed using Fusion 360 software. The actual titanium housing parts were produced at CERN workshop and the ceramic board with brazed pins was ordered from an external company.

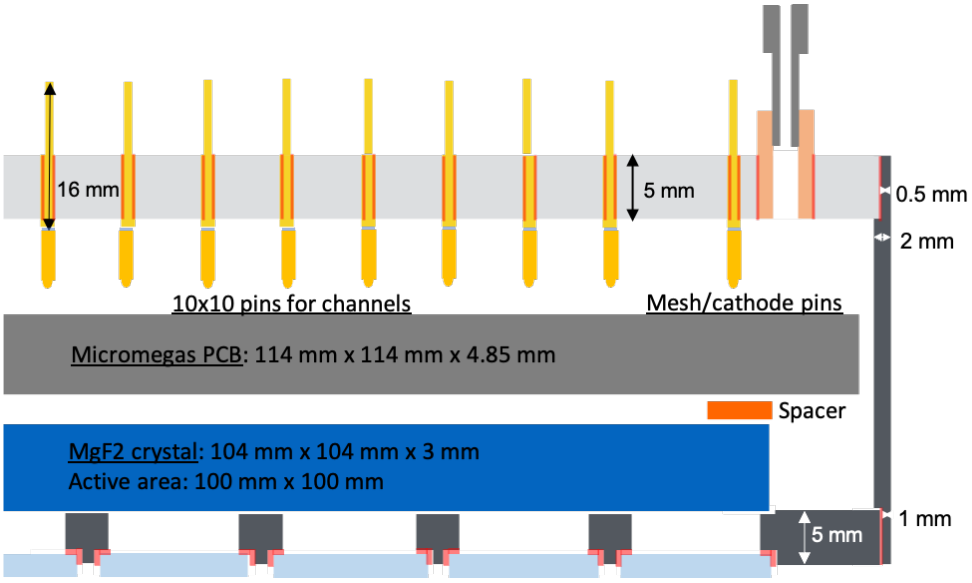

Figure 4.8: A cross section of the sealed housing. In this concept there are titanium housing parts, a ceramic board instead of the outer PCB and extra sapphire windows on the bottom.

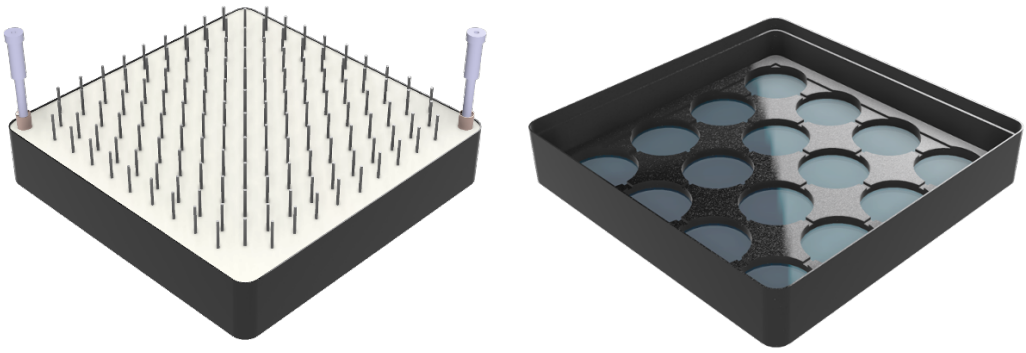

Figure 4.9: 3D drawings of the aluminium housing: left - top view; right - inside view.

The procedure of the sealed housing assembly is presented in Figure 4.7. Looking from the right side: the ceramic board is brazed to the metallic housing on its lateral sides, pogo pins are soldered to the pads on the ceramic board and the MicroMegas PCB is pressed against the pogo pins. Looking from the left side: the sapphire windows are brazed to the flange and the MgF_2 crystal is placed on the flange. The last step is that the metallic flange is electron beam welded to the metallic walls to avoid heating the full assembly when the sensitive detector components are placed inside.

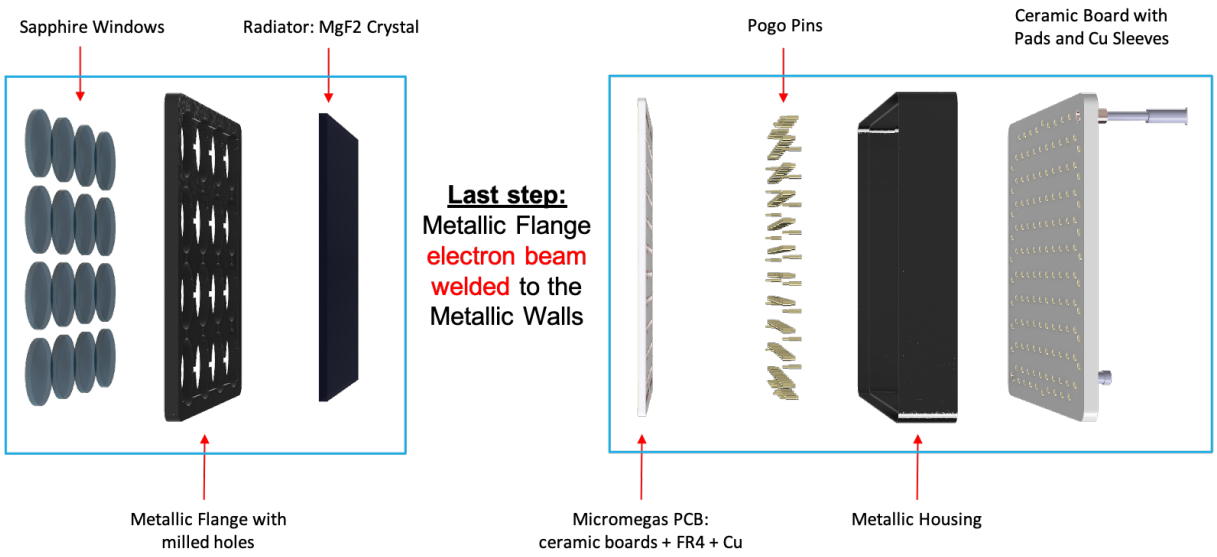

Figure 4.10: The procedure of the sealed housing assembly (described in detail in the text).

Summarising the new PicoSec module, two different housing were designed. When it comes to the aluminium housing, the first detector assembly was produced, while for the sealed housing, the detector is still in production. In addition, developments towards applicable detector included the improvement of the MicroMegas PCB planarity to minimise the deformations below 10 μm are required.

Chapter 5

ASSET - photocathode characterisation device

5.1 Introduction

The first prototypes of the PicoSec detector uses semi-transparent CsI photocathodes (18 nm) on MgF_2 crystals and the degradation of CsI quantum efficiency is a concern in the development of this concept [2]. The motivation to develop the ASSET setup are robust photocathodes for use with precise timing MicroMegas as in the PicoSec MicroMegas project. Therefore, the quantification of the degradation of CsI when exposed to ion back flow and the examination of possible alternative photocathode materials as well as protective layers are the main goals of the ASSET setup development. The ASSET setup was originally developed for ALICE-HMPID [30] and it has been upgraded and modified for the purposes of this thesis.

5.2 Overview of the setup

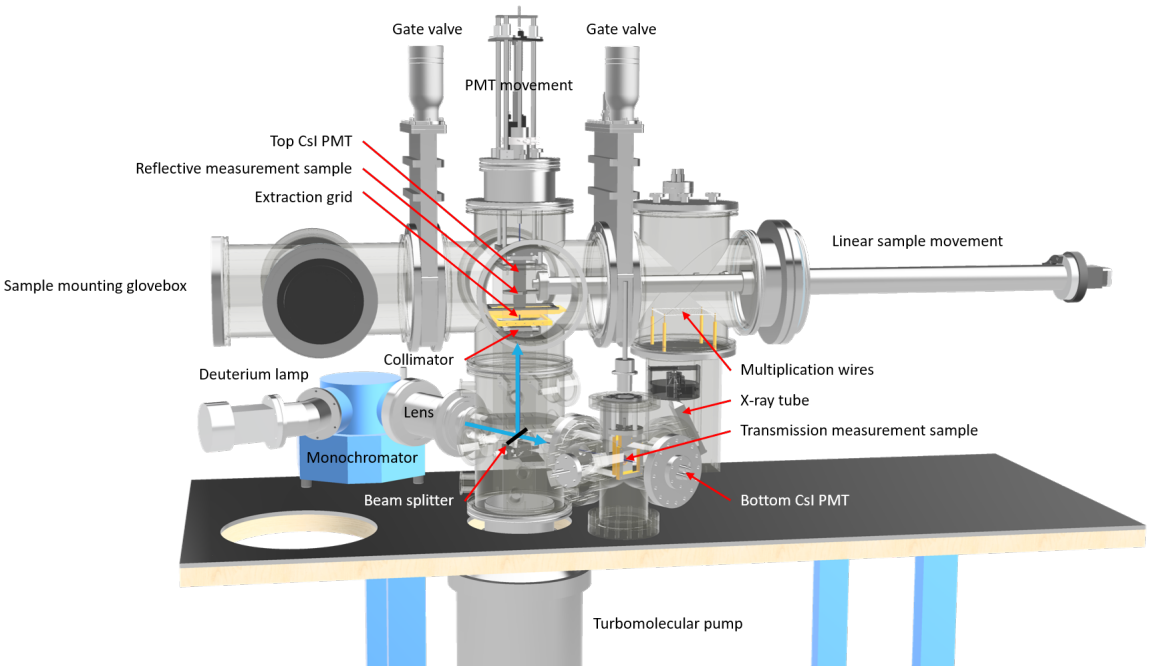

Figure 5.1: The general overview of the ASSET setup.

The general overview of the ASSET setup is presented in Figure 5.1. Measurements are done by the use of UV light from a system consisting of a deuterium lamp [31] and a VUV monochromator [32]. The system can be purged with high purity nitrogen in order to avoid any absorption of the short wavelength part of the UV spectrum. The monochromator is attached to the measurement chamber via an extension containing a MgF_2 collimating lens with the aim of focusing the light. A beam splitter divides the light into two separate beams. The light intensity is monitored by two calibrated CsI PMTs, one of which is used to measure the amount of light in the sample position, while the other one monitors stability of the light during measurements. The wavelength range that the measurements are conducted in is limited to about 130 nm on the low-wavelength side due to the MgF_2 lens transparency and at about 170 nm on the high-wavelength side due to the intensity of light from the deuterium lamp. The highest light intensity is observed at 160 nm. The deuterium lamp spectrum is shown in Figure 5.2.

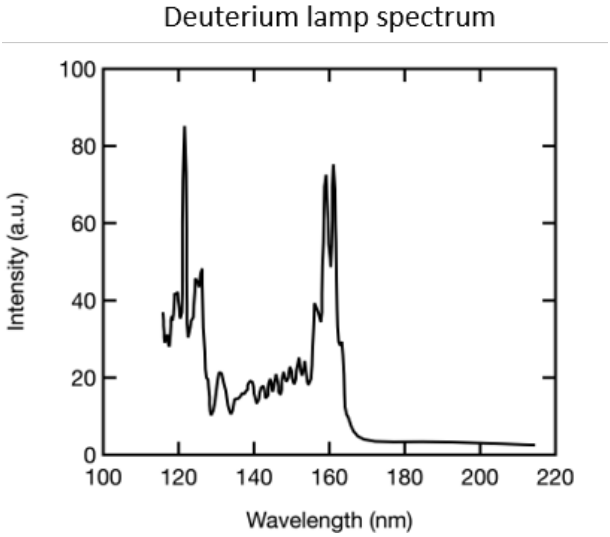

Figure 5.2: The deuterium lamp spectrum. The highest light intensity in the accessible wavelength range is observed at 160 nm.

The setup permits reflective as well as transmission mode measurements. The reflective mode allows to measure the quantum efficiency of the photocathodes, while the transmission mode enables the measurements of the quantum efficiency as well as the transparency. The modes are marked in Figure 5.3. Both measurements are done in the vacuum on the level of 10^{-7} mbar obtained by pre-pumps and turbomolecular pumps. In addition, irradiation to induce ageing due to ion bombardment is possible. The irradiation is done in a gas mixture with an X-ray tube providing primary ionisation and wire grid used to create high ion currents. The setup contains gate valves that permit a separation of the volumes and pump only the measurement chamber or flush only the irradiation chamber. A sample movement arm enables a linear transfer of the sample from one part of the chamber to another.

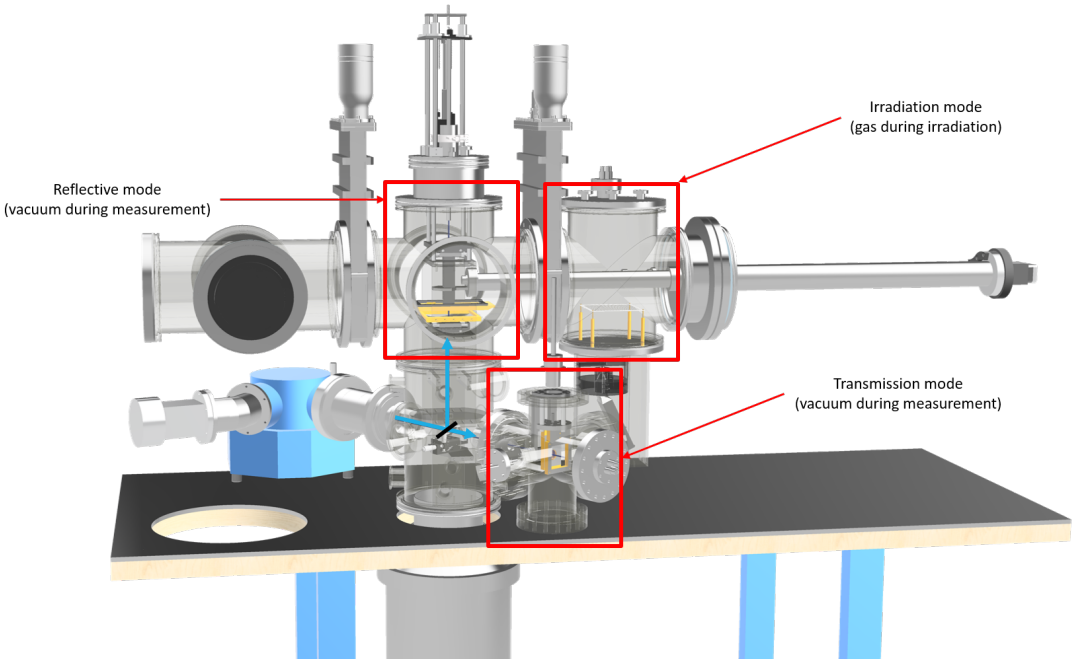

Figure 5.3: The setup permits reflective and transmission mode measurements as well as irradiation to induce ageing due to ion bombardment.

5.2.1 Reflective mode

The scheme of the reflective mode measurement is shown in Figure 5.4a. The UV beam coming from the bottom of the chamber arrives to the collimator. The light intensity is monitored by two calibrated CsI PMTs. The top PMT can be inserted into the measurement position to be in the same location as the sample being measured using an automated linear movement device and it can measure the amount of light, while the sample is out of the measurement position that is shown in Figure 5.4b. The top PMT can be also moved back to the IDLE position and the sample can be transferred to the measurement position. In this configuration the light hits the sample and electrons extracted from it are collected on a grid placed 5 mm under the sample that is shown in Figure 5.4c. The sample holder provides 3 positions for samples, so it is possible to measure them one after another without exposing them to air.

5.2.2 Transmission mode

Besides the reflective mode, the setup permits the transmission mode measurement that is shown in Figure 5.5. It is targeted at semi-transparent photocathodes such as thin photocathode layers on crystals. The transmission mode reflects the way photocathodes will be used in the PicoSec project and is closer to the intended application than the reflective mode. The UV beam, which is transmitted through the beam splitter, goes through a MgF_2 window that separates two volumes and preserves vacuum in main chamber, and it arrives to a collimator. The transmission mode is able to measure one sample at the time that can be transferred (together with an extraction mesh) into and out of the UV beam path. In the measurement position, the light hits the sample and electrons extracted from it are collected on the mesh mounted 1 cm behind the sample. Analogously, like in the reflective mode, the light intensity is monitored by two calibrated CsI PMTs.

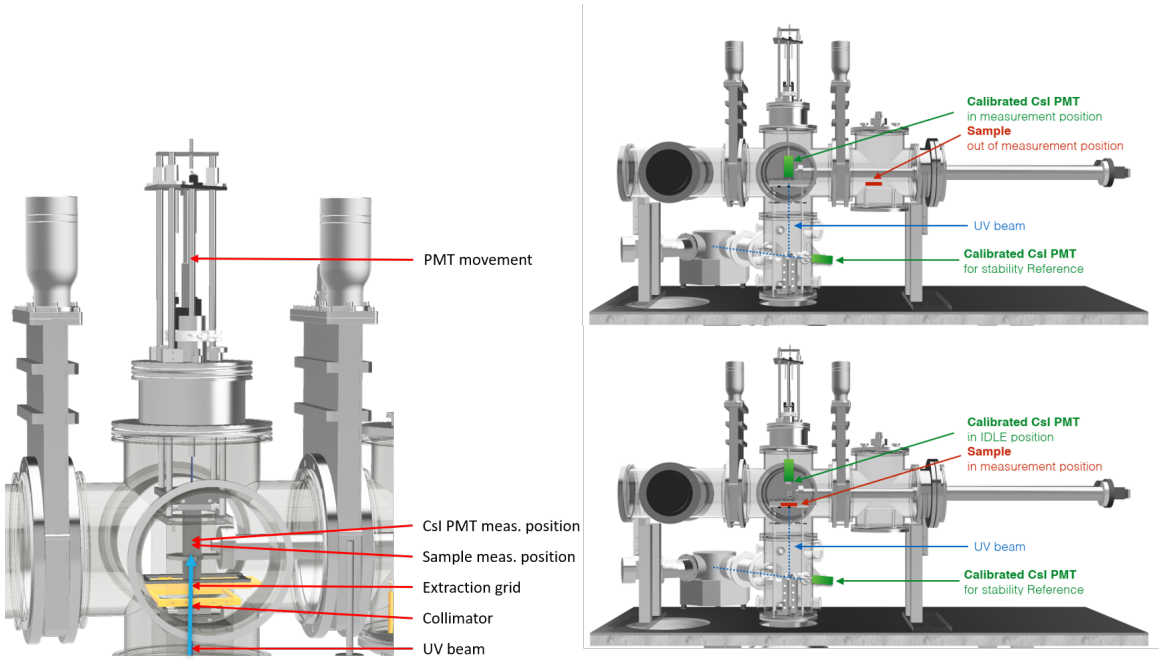

Figure 5.4: (a) The scheme of the reflective mode measurement. (b) The top PMT in the measurements position, while the sample out of the measurement position. (c) The top PMT out of the measurements position, while the sample in the measurement position.

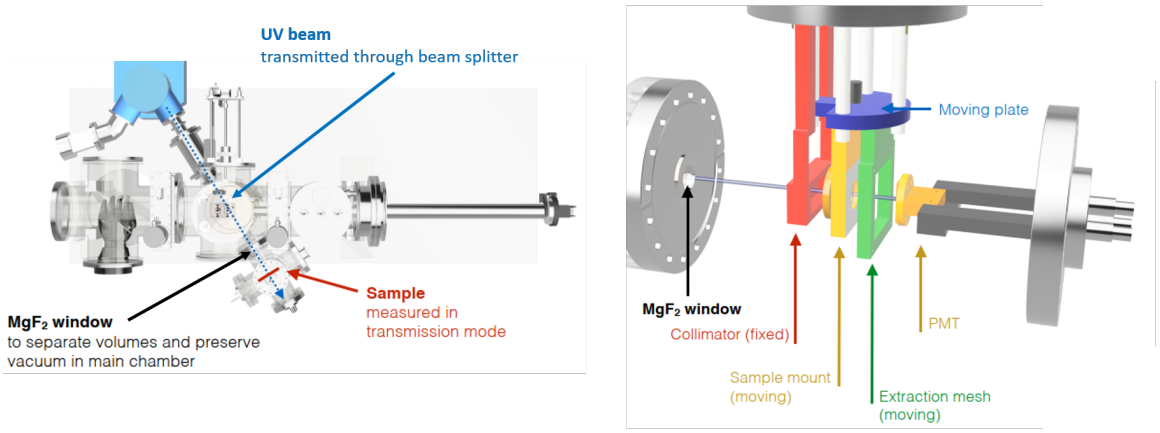

Figure 5.5: The scheme of the transmission mode. The mode is targeted at semi-transparent photocathodes such as thin photocathode layers on crystals.

5.2.3 Irradiation mode

In addition to the measurement modes, irradiation to induce ageing due to ion bombardment is possible. The scheme of the irradiation mode is shown in Figure 5.6. The sample movement arm enables a linear transfer of the sample from the reflective mode to irradiation position. An X-ray beam enters the irradiation chamber filled with a gas mixture: 70%Ar + 30%CO_2 (at ambient pressure), the gas is ionised by the X-ray photons and primary electrons are created. The

primary electrons are attracted by the multiplication wires and due to avalanche multiplication in the high electric field region in the vicinity of the wires, electrons and ions are produced. Electrons from the avalanche are collected on the wires, while ions move towards the sample which is at ground potential. This is used to accumulate a certain amount of charge on a sample in order to quantify the drop in quantum efficiency after such an exposure. The scheme of the irradiation process is presented in Figure 5.7.

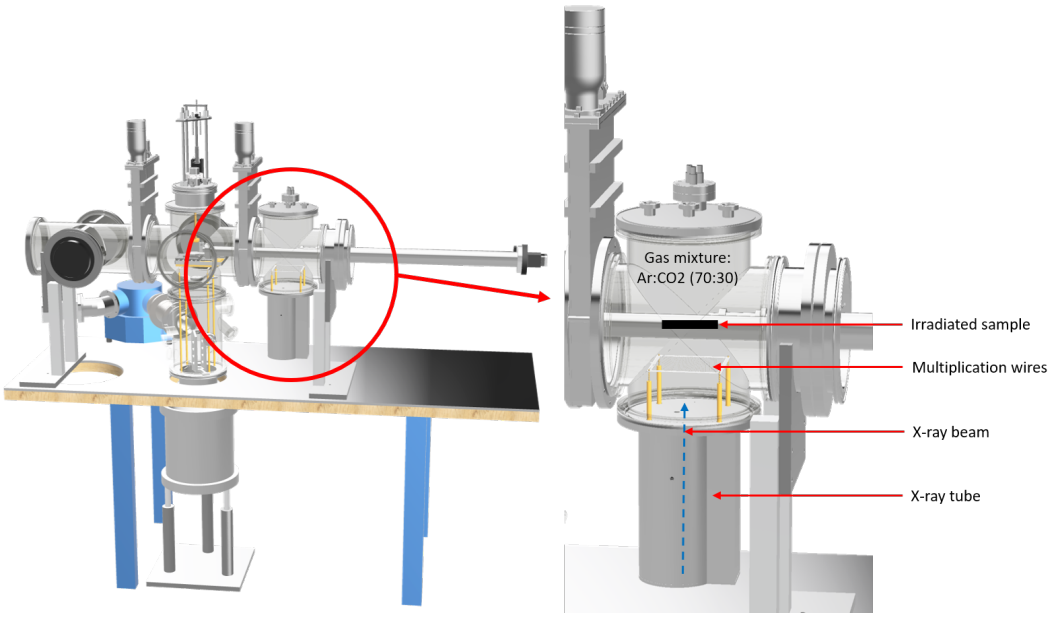

Figure 5.6: The scheme of the irradiation chamber, where irradiation to induce ageing due to ion bombardment is possible. During the process, the irradiation chamber is filled with gas mixture.

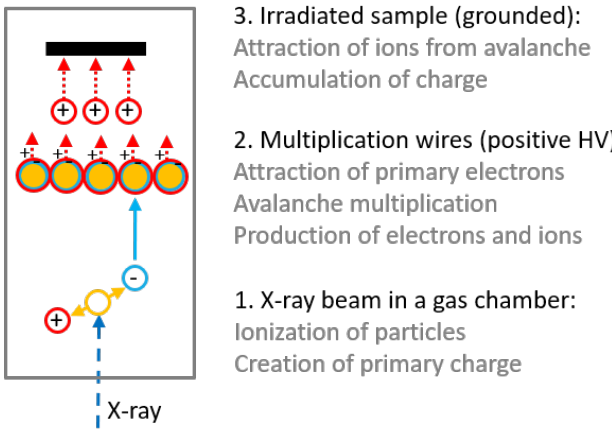

Figure 5.7: The scheme of the irradiation process. The X-ray tube is used to create primary charge and ions are produced by avalanche multiplication at the wires operated in a gas mixture. The charge is accumulated on a sample and measured by an ammeter.

5.2.4 Setup upgrades

Improvement, development and automatisation of the ASSET setup were necessary to optimise it for the measurements. A few of the implemented upgrades are listed below:

- The communication between the ASSET setup and the user is performed by a common PCB, Arduino boards and a custom LabVIEW software. The PCB was exchanged and Arduino as well as LabVIEW software were programmed. The hardware components are presented in Figure 5.8

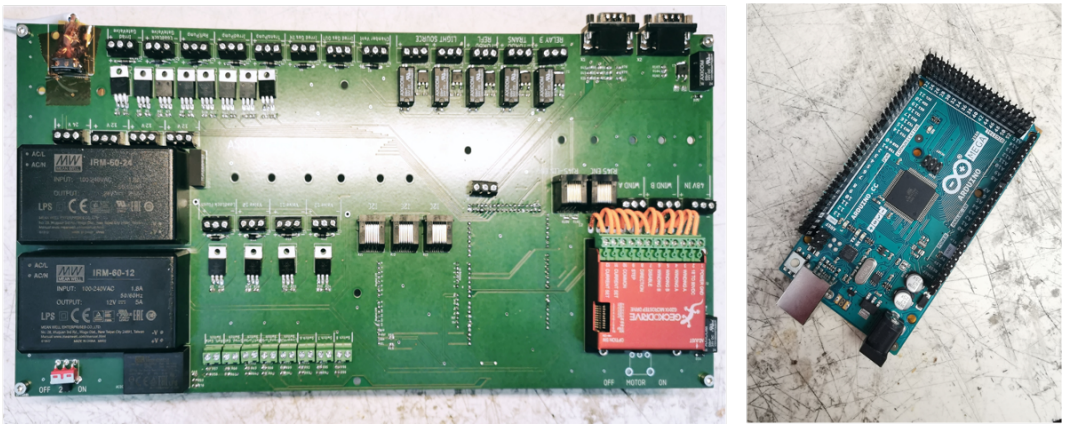

Figure 5.8: Left: the exchanged common PCB; right: the Arduino board.

- For the cables in the transmission mode, they were replaced with triax shielded cables to lower the noise of the photocurrent.
- A sample movement arm makes a linear transfer of the sample from one part of the chamber to another. For an automated linear movement device, new components including a motor, a gearbox, a potentiometer were ordered, assembled and programmed.

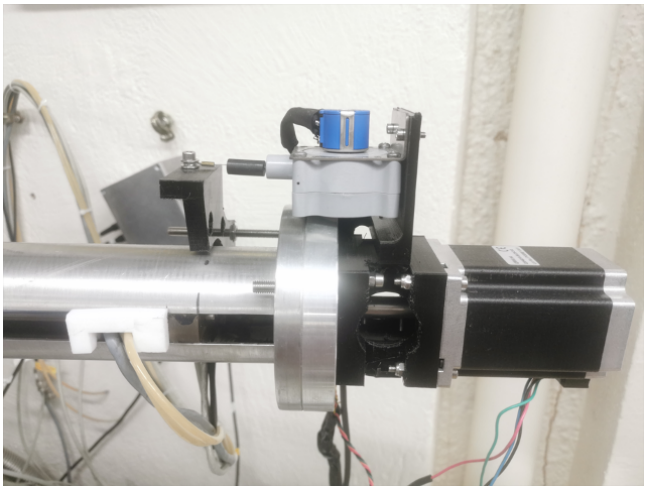

Figure 5.9: New components for the automated linear movement device.

- For collimating optics to extend sensitivity and wavelength range, a simple collimating lens was replaced with a collimating mirror chamber, which is presented in Figure 5.10. Figure 5.11 shows how the focusing for different wavelength looked like for a MgF_2 lens and how it looks for the collimating mirror chamber. The adjustment was implemented at the end of my work at CERN and was not used for the presented measurements.

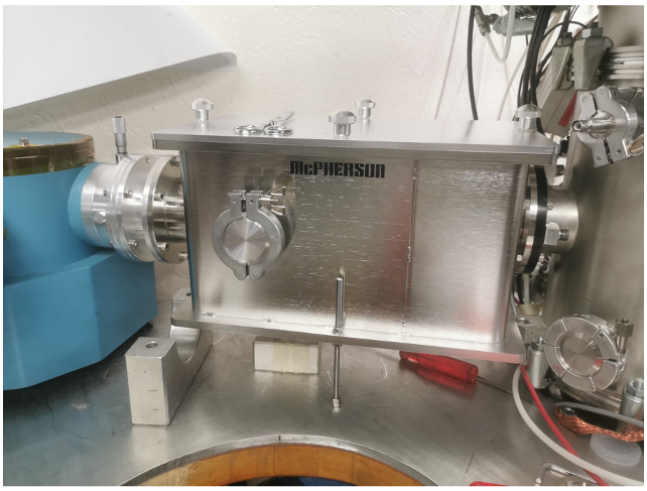

Figure 5.10: The collimating mirror chamber that replaced a simple collimating lens.

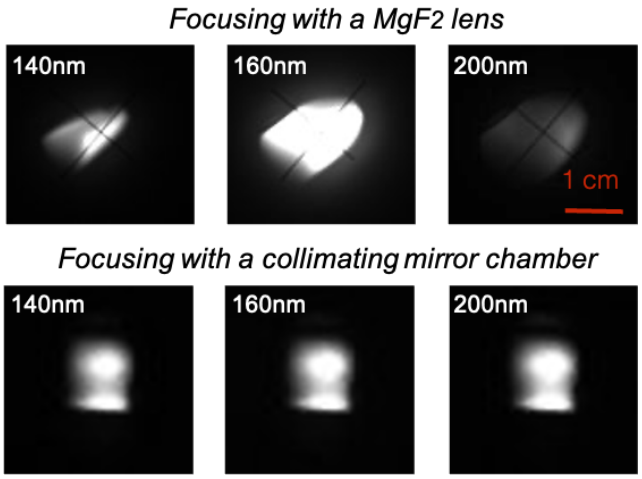

Figure 5.11: The comparison of the focusing for different wavelength for a MgF_2 lens (first row) and for the collimating mirror chamber (second row).

5.3 LabVIEW software

The custom LabVIEW software developed for the control on the setup provides manual operations as well as automated reflective or transmission mode measurement and irradiation routines. The screenshot of the "Manual Operation" interface is shown in Figure 5.12. It allows the user to check and manage many preparation and measurement options, including:

- sample choice and movement;
- light and monochromator settings;
- pumping and monitoring the pressure;
- manual measurement of the current on PMTs and samples;
- irradiation of samples.

Figure 5.12: The screenshot of the "Manual Operation" interface.

The reflective and transmission modes provide automated procedures of measurements with the possibility to choose samples to be measured (with an option to scan samples position - only for reflective mode) as well as the wavelength range and wavelength steps. The interfaces include graphs to present current measurements results. The screenshots of the "Reflective Measurement" and "Transmission Measurement" interfaces are shown in Figures 5.13 and 5.14, respectively.

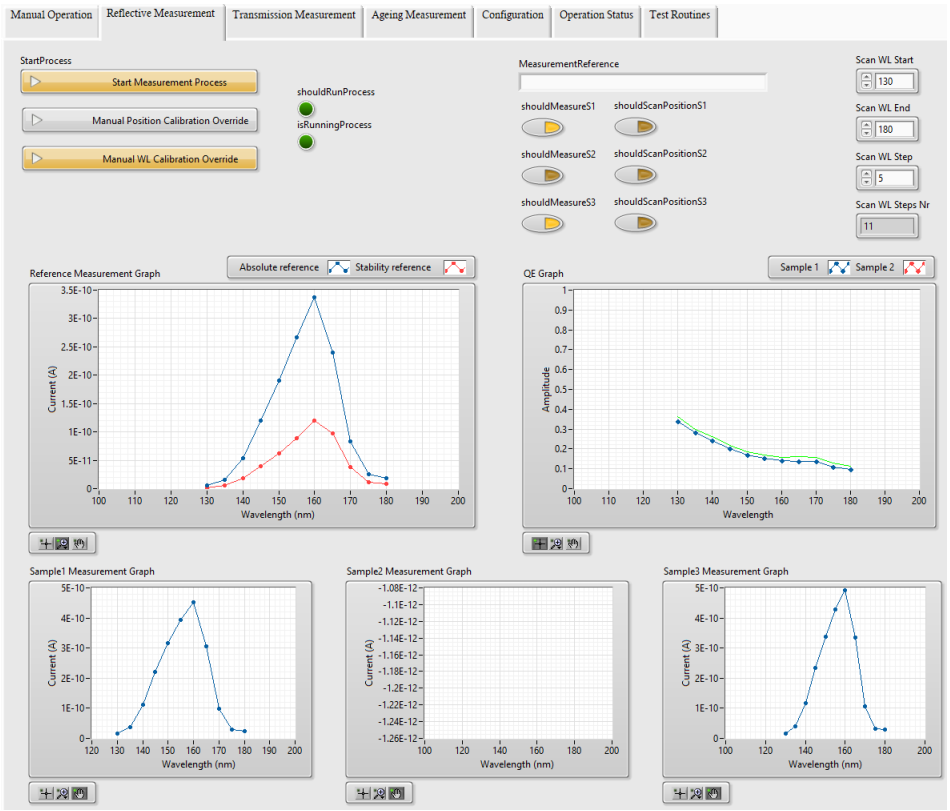

Figure 5.13: The screenshot of the "Reflective Measurement" interface.

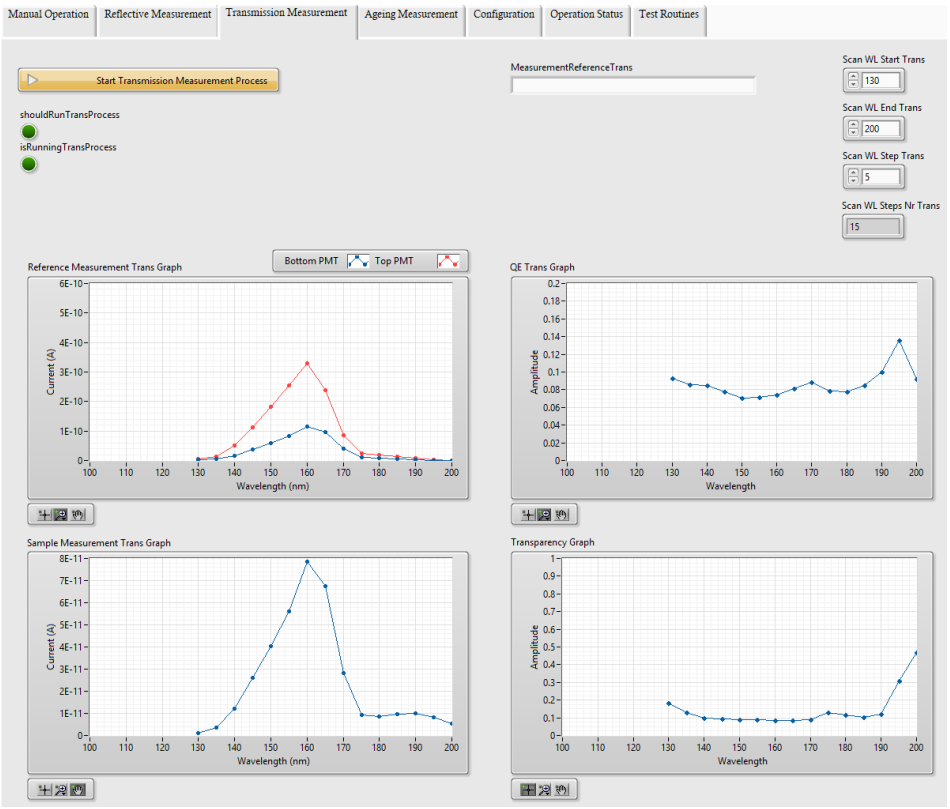

Figure 5.14: The screenshot of the "Transmission Measurement" interface.

The ASSET setup also provides an automated LabVIEW procedure of measurement and irradiation of the samples in the reflective mode, which was fully developed by me. The interface allows one to define a sequence of alternating tasks with the following parameters:

- a task: M (measurement) or I (irradiation);
- a sample (S1, S2, S3);
- a charge to be accumulated (in case of irradiation).

This means that it is not required to manually take care of the pumping that is needed for measurement as well as flushing for irradiation, because all the routines are already programmed in the software. The screenshot of the "Ageing Measurement" interface is shown in Figure 5.15.

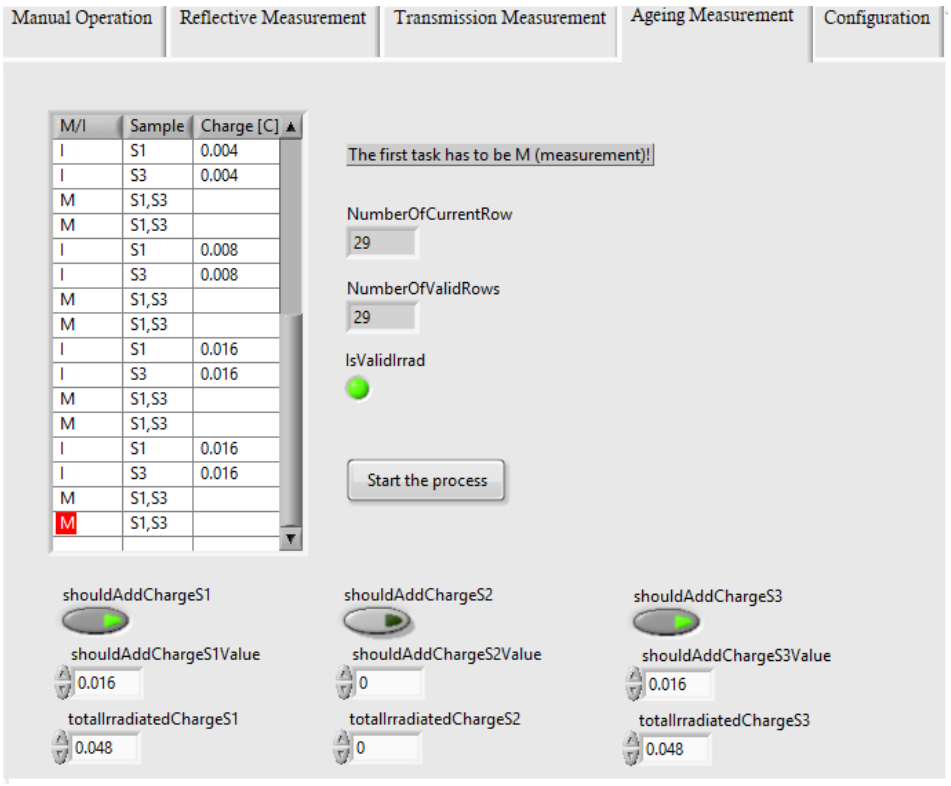

Figure 5.15: The screenshot of the "Ageing Measurement" interface that provides a fully automated procedure of measurement and irradiation of the samples in the reflective mode.

5.4 Measurement capabilities

The main capability of the setup is the measurement of photocurrents and the calculation of quantum efficiency (QE) in both modes. The full routine of the QE measurement is as follows:

- moving the top PMT in the sample position;
- scanning wavelengths and recording light intensity with both PMTs;
- moving the top PMT to idle, inserting a sample;
- scanning wavelengths and recording photocurrent from the grid and light intensity on the bottom PMT;
- comparing extracted photocurrent with light intensity (corrected with the bottom PMT).

Quantum efficiency is calculated from current measurements by the formula:

$$QE = \frac{N_e}{N_{ph}} = \frac{\frac{I_s}{e}}{\frac{I_{PMT}}{e \cdot CalFac_{PMT}}}, \tag{5.1}$$

where:

N_e	- number of electrons extracted from the sample (measured on the sample in the measurement position);
N_{ph}	- number of photons that arrived to the sample (measured on the PMT in the measurement position);
I_s	- current measured on the sample (offset subtracted);
I_{PMT}	- current measured on the PMT (offset subtracted);
$CalFac_{PMT}$	- calibration factor from the calibrated CsI PMT (depends on wavelength);
$e = 1,602 \cdot 10^{-19}\ [C]$	- elementary charge.

In the transmission mode, additionally, the transparency (T) can be extracted. Transparency is given by the formula:

$$T = \frac{I_{PMT,\ sample\ in}}{I_{PMT,\ sample\ out}}, \tag{5.2}$$

where:

$I_{PMT,\ sample\ in}$	- PMT current measured when the sample in measurement position;
$I_{PMT,\ sample\ out}$	- PMT current measured when the sample out of measurement position.

The following Subsections 5.4.1-5.4.4 describe the capabilities of the ASSET setup that have been verified in order to allow reliable measurements of the samples.

5.4.1 Reproducibility

A valuable feature of the setup is the reproducibility of QE measurements. Examples of the ASSET reproducibility (two different sets of measurements) are presented in Figures 5.16 and 5.17. In both graphs, the results mostly overlaps and minor fluctuations between measurements may come from: different pressure, noise, offsets in the measurement of the photocurrent or CsI degradation. Error bars are given in all measurements and they represent statistical errors from current measurements.

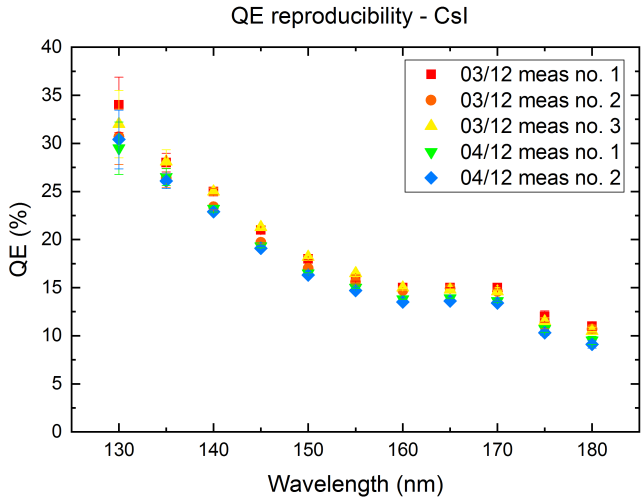

Figure 5.16: Five QE measurements of CsI 057 (18 nm) sample made during 2 days.

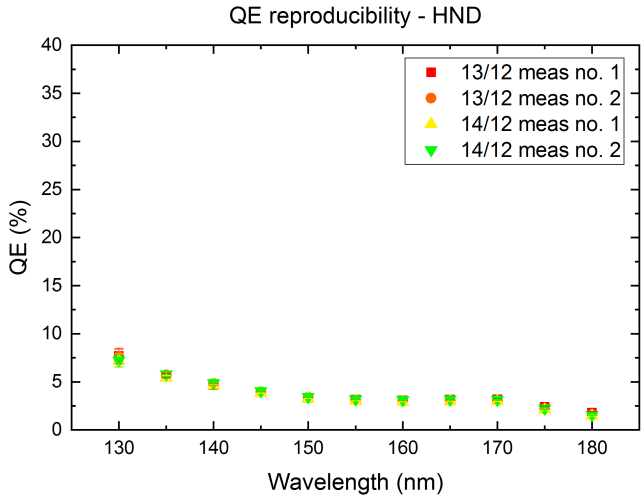

Figure 5.17: Four QE measurements of HND 060 (50 shots) sample made during 2 days.

5.4.2 Electric field scanning

An electric field scanning to determine an efficient extraction field for different samples was performed for both the reflective and the transmission mode. The gap between the sample and the extraction wires for the reflective mode is 5 mm thick and for the transmission mode it is 1 cm thick. The photocurrent was measured at 160 nm. The electric fields were set at the values where all the currents were efficiently collected (where a plateau were observed) - at 1000 V/cm for the reflective mode and at 300 V/cm for the transmission mode. The electric field scanning for the reflective and transmission modes are shown in Figures 5.18 and 5.19.

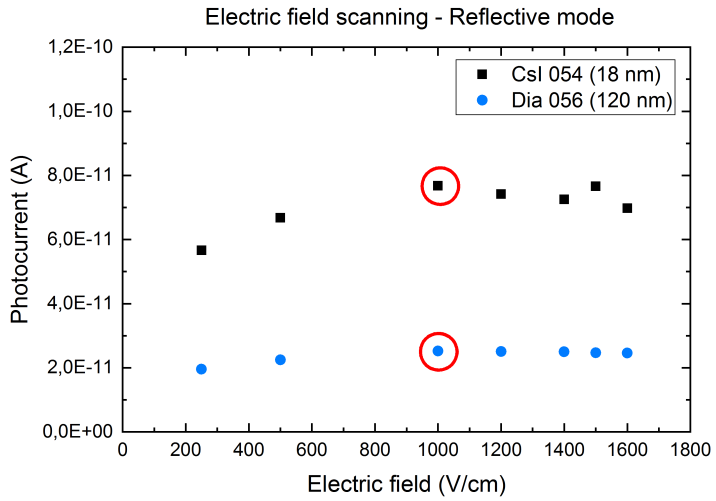

Figure 5.18: The electric field scan of CsI 054 (18 nm) and Dia 056 (40-120 nm) samples in the reflective mode. In this case the electric field was set at 1000 V/cm for both samples.

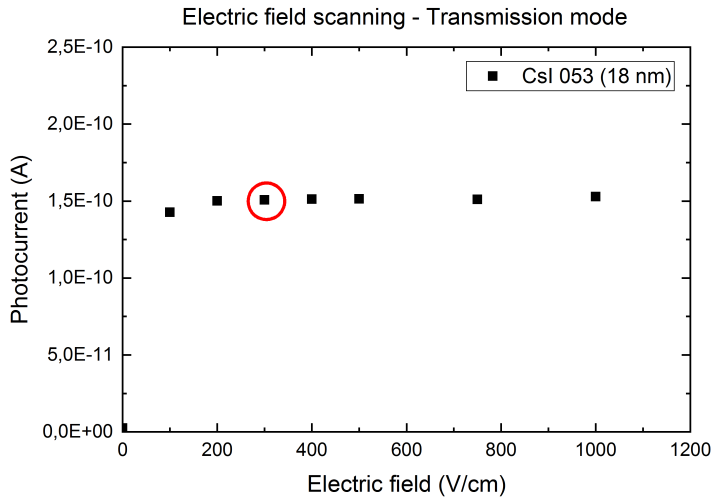

Figure 5.19: The electric field scan of CsI 053 (18 nm) sample in the transmission mode. In this case the electric field was set at 300 V/cm.

5.4.3 Position scanning

Besides the electric field, the setup allows us to scan a position of the samples to study QE uniformity along one direction. This kind of measurement can be done only in the reflective mode. Examples of the position scanning of CsI as well as hydrogenated nanodiamonds (HND) samples are presented in Figures 5.20 and 5.21 respectively. The photocurrent was measured at 160 nm. The extraction grid was set at 500 V for CsI and 1000 V for HND. The UV beam has a diameter of 5 mm, while the scanning area has a diameter of 17 mm (marked as a blue rectangular in Figures 5.20 and 5.21).

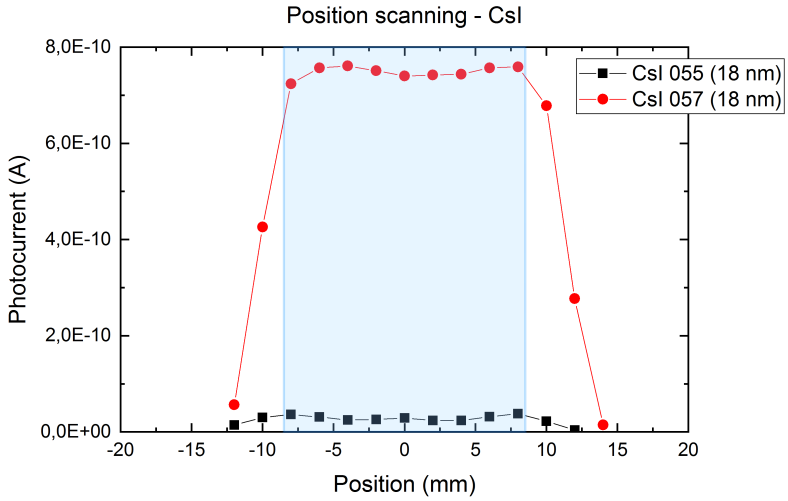

Figure 5.20: The position scanning of CsI samples. The samples have profiles with edges decreasing when the spot is (partially) outside of the sample. CsI 055 has a lower photocurrent than CsI 057 due to previous degradation (exposure to humidity in ambient air).

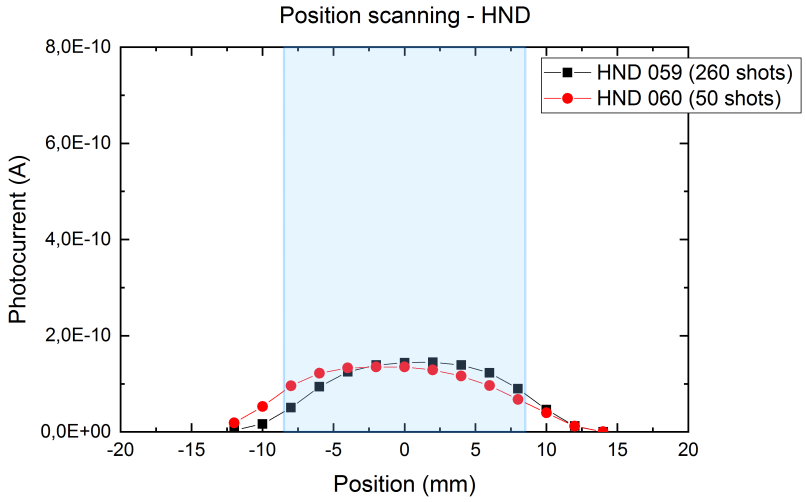

Figure 5.21: The position scanning of HND samples. The samples have gaussian shape profiles due to the deposition procedure.

5.4.4 Ageing studies

A crucial capability of the ASSET measurements are ageing studies. Figure 5.22 presents the interface of the irradiation process. It allows to manually open and close the valves for gas flow, switch on and off the X-ray tube. The preparation for irradiation as well as the execution of the routine for chosen samples with irradiation up to a chosen target charge to be accumulated can be run in an automated mode. In addition, the preparation for the measurement after the irradiation is possible.

The ageing studies routine is performed as follows: At the beginning, the irradiation chamber is separated from the reflective one and filled with the Ar:CO_2 (70%:30%) gas mixture. Then, in order to achieve a good quality of the gas inside, the volume is pumped with the use of the irradiation pre-pump and again filled with the gas mixture. This can be repeated multiple times to improve the quality of the gas in the volume. Afterwards, the X-ray tube and the high voltage of the wires are switched on and the charge is accumulated on the surface of the sample. The graph in the top right corner of Figure 5.22 shows the dependence of temperature, current and voltage of the X-ray tube in time during the ageing studies. The second graph presents sample current as a function of time and the third on displays charge accumulated as a function of time measured during the irradiation routine.

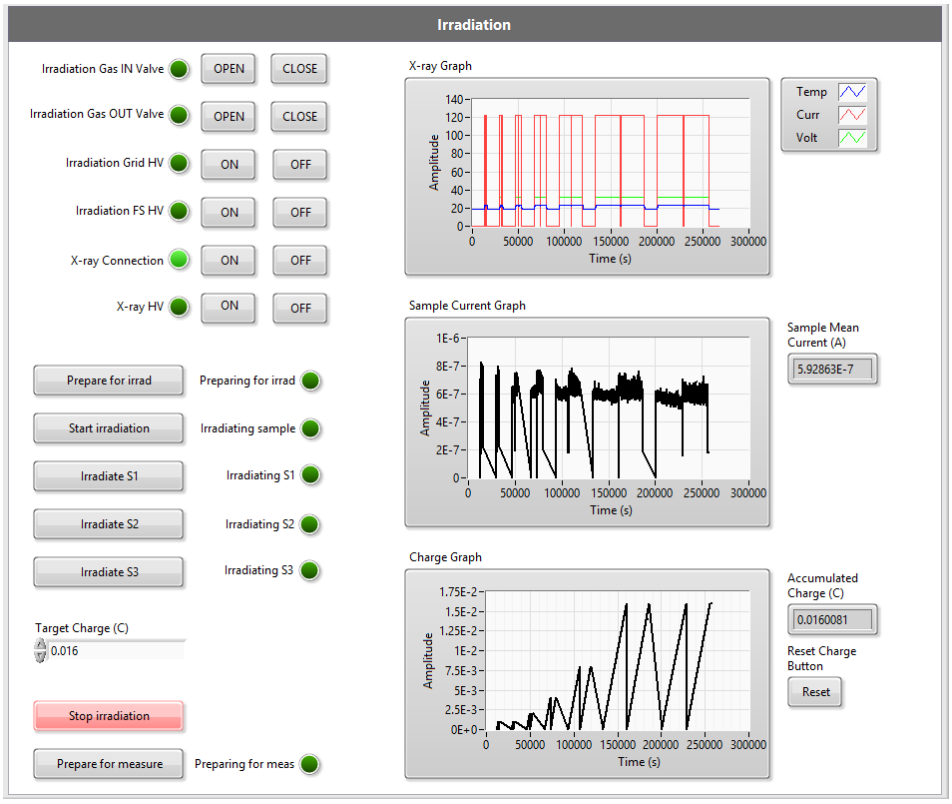

Figure 5.22: The interface of the irradiation process.

In order to confirm that irradiated samples suffer from the ion bombardment, the influence of the gas and X-rays was checked. The test was performed on the CsI samples in the same way as a standard ageing study in the gas mixture but the HV grid was switched off, i.e. no amplification and significant production of ions was taking place. CsI 072 was placed in the position 1 in the

sample holder and CsI 073 - in the position 3 (as a reference). During the measurement only X-rays were hitting the sample and the test was run for the same amount of time as during the standard ageing of CsI 068. The results of QE and QE descrease vs total time of being exposed to the gas and X-rays are presented in Figures 5.23 and 5.24, respectively. After 2 steps of exposure - 8 min and 15 min, 23 min in total - QE decrease of CsI 068 - 0.16 mC charge accumulated in total - equaled 15% (reference CsI 069 was 3%). QE decrease of CsI 072, aged with HV grid off, equaled 3% (reference CsI 073 was 2%). This shows that samples suffer not only from the ion bombardment, but the gas and/or X-rays also contribute to the QE decrease.

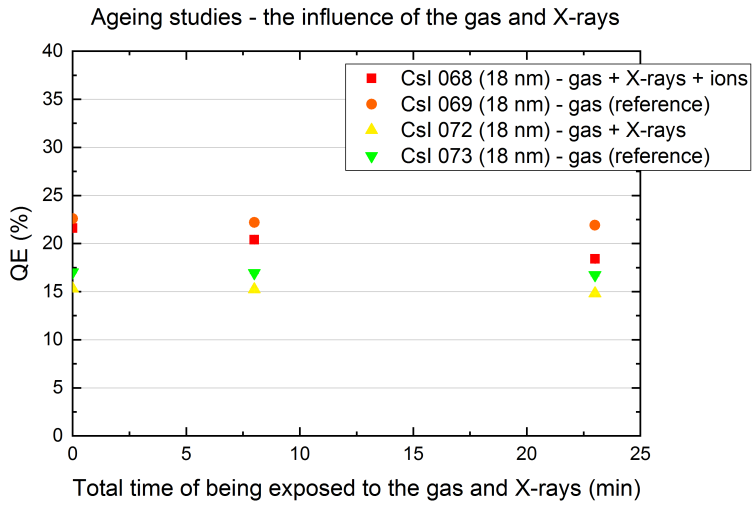

Figure 5.23: QE vs total time of being exposed to the gas and X-rays. 2 steps of exposure of 8 min and 15 min were performed. It can be seen that the gas and/or X-rays also contribute to the QE decrease.

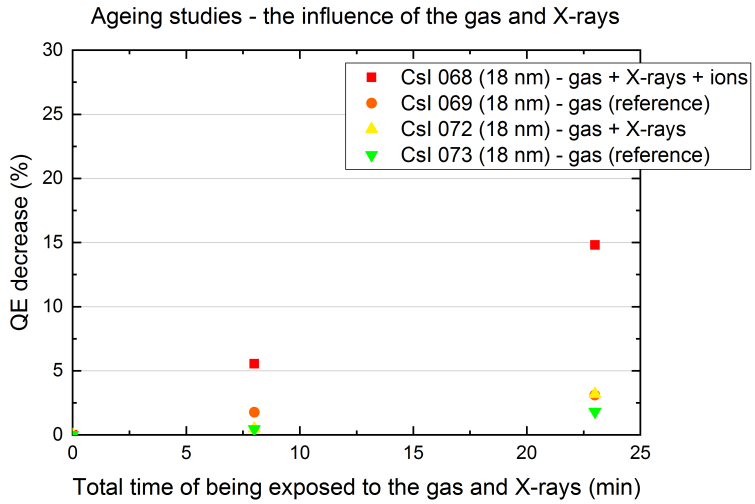

Figure 5.24: QE descrease vs total time of being exposed to the gas and X-rays. QE decrease of CsI 068 after 23 min of exposure - 0.16 mC/cm^2 charge accumulated in total - equaled 15% (reference CsI 069 was 3%), QE decrease of CsI 072, aged with HV grid off, equaled 3% (reference CsI 073 was 2%).

Next test was to check the influence of the gas only. The ageing studies of CsI 072 and CsI 073 were performed in the gas with both HV grid and X-rays off, just to let the samples stay in the gas for the same amount of time as during the standard ageing of CsI 068. The results of QE and QE descrease vs total time of exposure are presented in Figures 5.23 and 5.24, respectively. On the left side of the dashed line the results of being exposed to the gas and X-rays are presented, while on the right side - the results of being exposed to the gas only.

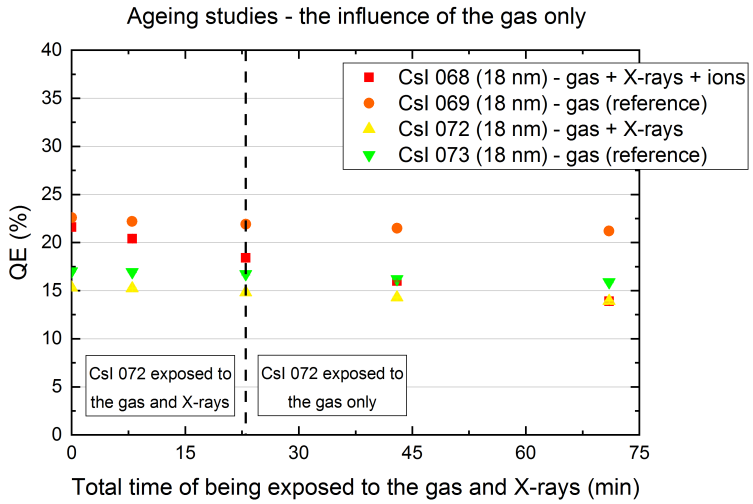

Figure 5.25: QE vs total time of exposure. On the left side of the dashed line the results of being exposed to the gas and X-rays are presented, while on the right side - the results of being exposed to the gas only.

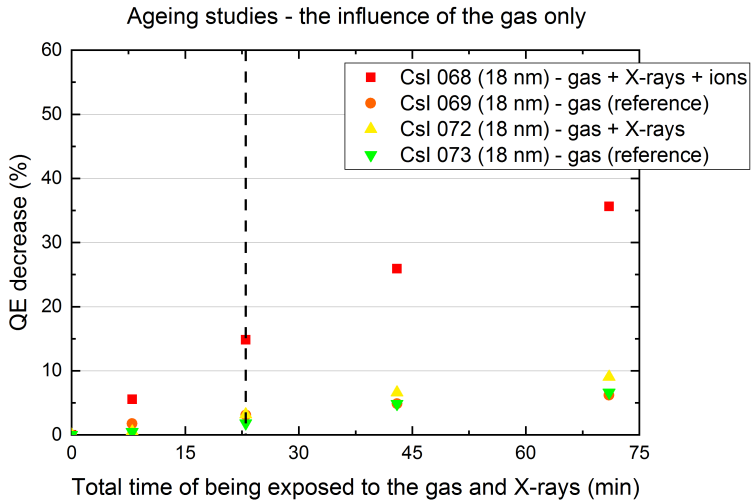

Figure 5.26: QE descrease vs total time of exposure. QE decrease of CsI 068 after 71 min - 0.16 mC charge accumulated in total - equaled 36% (reference CsI 069 was 6%), QE decrease of CsI 072, exposed to the gas only, equaled 9% (reference CsI 073 was 7%).

The measurement shows that after 2 more steps of exposure - 20 min and 28 min, 71 min in total - QE decrease of CsI 068 - 0.21 mC charge accumulated in total - equaled 36% (reference CsI 069 was 6%). QE decrease of CsI 072 equaled 9% (reference CsI 073 was 7%). QE decrease trend of CsI 072 is approximately linear, thus, the impact of the gas is much greater than of X-rays. Due to the thin layer of the CsI and the resulting cross-section for an interaction of X-rays with the photocathode layer, no test to check the influence of X - rays only was performed.

Knowing that the gas affects the measurements, in order to check Ar:CO_2 mixture quality, studies on the humidity level inside the irradiation chamber were carried out. The measurements were done using a residual gas analyzer (RGA) and the results after different number of flushing are presented in Table 5.1. The amount of water after 2 flushing cycles was 14651 ppm and after a whole night of flushing it dropped to 2543 ppm. The data from the RGA can be used for a relative comparison of the water content but should not be treated as absolute numbers. A small orifice was used to sample gas from the ambient pressure irradiation chamber, which can affect the absolute values as sampling rate depends on gas species.

Table 5.1: Amount of water after different number of flushing.

Number of flushing	Amount of water [ppm]
2	14651
2	8306
4	6129
6	5215
All night	2543

Chapter 6

Photocathodes characterisation

6.1 Samples description

Although an ordinary metal cathode will exhibit photoelectric properties, a specialized coating greatly enhances this effect [4]. This is why photocathodes - thin layers of a material applied to the supporting surfaces - are commonly used in gaseous radiation detectors. They can be classified according to the mode in which they operate. There are opaque photocathodes - working in the reflective mode, the emission of electrons occurs from the same side from which the light falls - and semi-transparent photocathodes - working in the transmission mode, the emission of electrons takes place on the opposite side to the illuminated surface. Due to the low work function of the photocathodes, they are made mainly of alkali metals - often cesium - and their compounds. Depending on the type of the photocathode, it is sensitive in different spectral ranges, generally ranging from near infrared to ultraviolet. Photocathodes operate in a vacuum, that is why their construction corresponds to the technology of vacuum tubes [4]. Since most photocathodes are sensitive to air, their assembly usually takes place after the chamber has been evacuated. During the operation, photocathodes require an electric field with a positive electrode nearby to support the extraction of electrons from the photocathode material. An important quantity that defines photocathodes is quantum efficiency (QE).

Within the scope of this Master's thesis, the measurements of 4 different photocathode materials were made including: cesium iodide (CsI), diamond like carbon (DLC), boron carbide (B_4C) and hydrogenated nanodiamonds (HND). Different samples were produced by different research institutes including: European Organization for Nuclear Research (CERN), University of Science and Technology of China (USTC), French Atomic Energy Commission (CEA) and National Institute for Nuclear Physics (INFN).

6.1.1 Cesium Iodide

Cesium Iodide (CsI) is the most popular material used as a photocathode in gaseous radiation detectors due to its high QE and UV sensitivity. The baseline solution for PicoSec MicroMegas detector is a 18 nm CsI photocathode deposited on a 3 mm MgF_2 substrate with a 3 nm chromium (Cr) interface in-between them [2]. The photocathode was successfully used in test beam campaigns and exhibits high QE. Unfortunately, the material is sensitive to humidity and sparks, which results in the degradation of QE. Robustness of the photocathode is crucial to preserve QE and, thus, detector efficiency and timing resolution during prolonged operation. The problem can be solved in two ways: replacing CsI with alternative photocathode materials or using protection layers to make CsI more robust. The protection layers that could minimise

effects of ion back flow on CsI and mitigate degradation include materials like MgF_2 or LiF. The layers have already been tested before [35] and they have shown to passivate but also modify work function. The risk of using the protection layers is that they may also inhibit the extraction of electrons and result in low QE. Table 6.1 presents the description of CsI samples that were measured within the scope of this Master's thesis. The photocathodes differ in the thickness of the Cr interface. All of them were produced at CERN using chemical vapour deposition technique.

Table 6.1: CsI samples description.

Sample ID	Material	Substrate	Interface	Protection	Producer
CsI 053	CsI 18nm	MgF_2 3mm	Cr 3nm	-	CERN
CsI 068	CsI 18nm	MgF_2 3mm	Cr 3nm	-	CERN
CsI 069	CsI 18nm	MgF_2 3mm	Cr 3nm	-	CERN
CsI 070	CsI 18nm	MgF_2 3mm	Cr 3nm	LiF 2 nm	CERN
CsI 071	CsI 18nm	MgF_2 3mm	Cr 3nm	MgF_2 2nm	CERN
CsI 072	CsI 18nm	MgF_2 3mm	Cr 3nm	-	CERN
CsI 073	CsI 18nm	MgF_2 3mm	Cr 3nm	-	CERN
CsI 074	CsI 18nm	MgF_2 3mm	Cr 3nm	-	CERN
CsI 075	CsI 18nm	MgF_2 3mm	Cr 3nm	-	CERN
CsI 076	CsI 18nm	MgF_2 3mm	Cr 1.19nm	-	CERN
CsI 077	CsI 18nm	MgF_2 3mm	Cr 1.59nm	-	CERN
CsI 078	CsI 18nm	MgF_2 3mm	Cr 2.09nm	-	CERN
CsI 079	CsI 18nm	MgF_2 3mm	Cr 1.19nm	-	CERN
CsI 080	CsI 18nm	MgF_2 3mm	Cr 1.59nm	-	CERN
CsI 081	CsI 18nm	MgF_2 3mm	Cr 2.09nm	-	CERN

6.1.2 Diamond-Like Carbon

Diamond-Like Carbon (DLC) is one of the alternative photocathode materials that could be inherently more robust to environmental influence and ion bombardment than CsI. DLC is a class of amorphous carbon material that contains diamond-structure as well as graphite-structure and exhibits excellent properties, including good chemical and thermal stability, hardness and wear resistance [33]. It can be applied to almost any other material that is compatible with a vacuum environment. The most commonly method for DLC coating is magnetron sputtering technique at low-temperature. The process is repeatable as well as controllable and provides photocathode layers with good accuracy and uniformity in thickness. Table 6.2 shows the description of measured DLC samples of different thickness, produced at USTC and CEA.

Table 6.2: DLC samples description.

Sample ID	Material	Substrate	Interface	Protection	Producer
DLC 007	DLC 10nm	MgF_2 3mm	-	-	USTC
DLC 008	DLC 10nm	MgF_2 3mm	-	-	USTC
DLC 009	DLC 3nm	MgF_2 3mm	-	-	USTC
DLC 010	DLC 10nm	MgF_2 3mm	-	-	USTC
DLC 050	DLC 30nm	MgF_2 3mm	-	-	CEA

6.1.3 Boron Carbide

Boron Carbide (B_4C) is the next candidate for an alternative photocathode material. B_4C is an organic chemical compound from the group of carbides, made of carbon and boron. It is a crystalline, extremely hard material that often replaces diamond. Table 6.3 presents the description of measured B_4C photocathodes of different thickness, with or without an interface layer, produced at CEA and USTC.

Table 6.3: B_4C samples description.

Sample ID	Material	Substrate	Interface	Protection	Producer
B4C 037	B_4C 10nm	MgF_2 3mm	Cr 3nm	-	CEA
B4C 038	B_4C 20nm	MgF_2 3mm	Cr 3nm	-	CEA
B4C 039	B_4C 10nm	MgF_2 3mm	-	-	CEA
B4C 040	B_4C 20nm	MgF_2 5mm	-	-	CEA
B4C 046	B_4C 5nm	MgF_2 3mm	Cr 3nm	-	CEA
B4C 047	B_4C 2.5nm	MgF_2 3mm	Cr 3nm	-	CEA
B4C 055	B_4C 50nm	MgF_2 3mm	Cr 3nm	-	USTC

6.1.4 Hydrogenated nanodiamonds

Nanodiamond (ND) photocathodes can also replace CsI photocathodes due to their better stability and robustness [34]. Thin layers consisting of small diamonds are obtained by Microwave Plasma Enhanced Chemical Vapour Deposition (MWPECVD) technique. Most of them have a peculiarity - hydrogenated surface - which moves down negative electron affinity (a crucial parameter for electron photo- and thermo-emission). Table 6.4 shows the description of measured (H)ND samples that differ in the thickness of the photocathode material, all produced at INFN.

Table 6.4: (H)ND samples description.

Sample ID	Material	Substrate	Interface	Protection	Producer
HND 059	HND 260s	PCB 2mm	-	-	INFN
HND 060	HND 50s	PCB 2mm	-	-	INFN
HND 061	HND 60s	MgF_2 3mm	-	-	INFN
HND 063	HND 100s	MgF_2 3mm	-	-	INFN
HND 064	HND 25s	PCB 2mm	-	-	INFN
HND 066	HND 200s	PCB 2mm	-	-	INFN
ND 067	ND 200s	PCB 2mm	-	-	INFN

6.2 Reflective mode measurements

In the reflective mode, QE vs wavelength measurements of four different photocathode materials (CsI, DLC, B_4C and (H)ND) were carried out. All the tests were performed in pressures below 5E-6 mbar. Results of the measurements are presented in Figures 6.1 - 6.5.

6.2.1 Cesium Iodide

Figure 6.1 presents the results of CsI photocathodes measurements done in the reflective mode. The aim of the test was to compare QE of CsI (18 nm) samples without and with protection layers: LiF (2 nm) and MgF_2 (2 nm). The materials were chosen due to the results presented in reference [35], where it was reported that these layers could slow down the ageing of the CsI photocathode. The graph shows that the CsI 069 has the highest QE, equals 22.6% @ 160 nm, while the protection layers of the samples CsI 070 and CsI 071 decrease their QE, which is an expected behaviour. There are two things that protection layers can do: block ions and block humidity. Not only does an extra layer on the top of photocathode make the path for particles longer and harder to pass, but it also acts as another interface that electrons have to traverse. This means that they need to have enough energy to pass this additional barrier from CsI where they are produced to the gas where they can move freely. Nevertheless, CsI with LiF protection layer has higher QE values than CsI with MgF_2 which makes the first one more promising candidate to replace pure CsI.

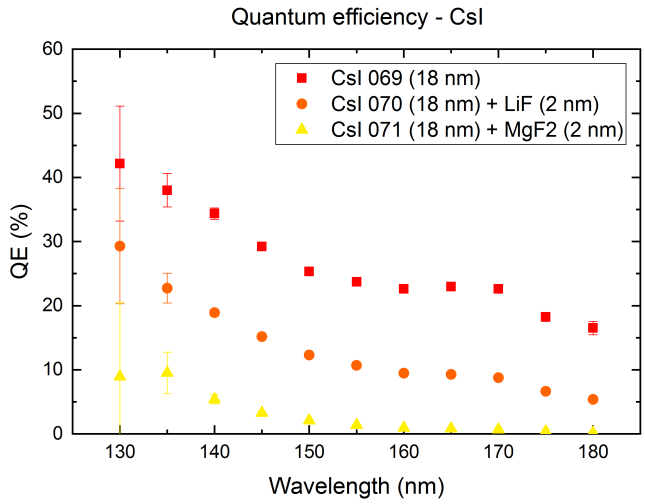

Figure 6.1: QE vs wavelength of three CsI photocathodes: CsI 069 (18 nm), CsI 070 (18 nm) with LiF (2 nm) protective layer and CsI 071 (18 nm) with MgF_2 (2 nm) protective layer, all measured in the reflective mode.

6.2.2 Diamond Like Carbon

DLC photocathodes were already tested in the beam with PicoSec detector and reasonable timing performance was achieved [29]. However, the values obtained with ASSET measurements are very low, what is presented in Figure 6.2 showing QE vs wavelength graph of three DLC (10 nm) photocathodes measured in the reflective mode. All DLC samples have QE values around 0.05% @ 160 nm, and above 165 nm they are too small to measure. The attempt to compare the factor in QE between CsI and DLC in ASSET measurement to the number of photoelectrons generated by Cherenkov light on the surface of photocathode layer for CsI and DLC from reference [29] with a possible explanation are presented in Subsection 6.3.3.

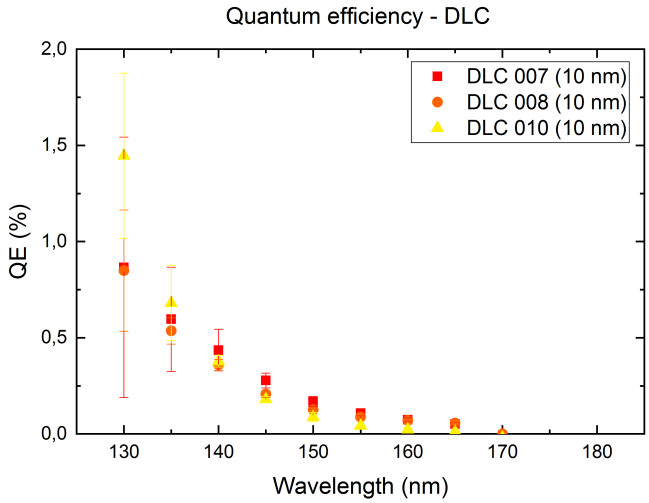

Figure 6.2: QE vs wavelength of three DLC (10 nm) photocathodes measured in the reflective mode.

6.2.3 Boron Carbide

Figure 6.3 presents the dependence of QE and wavelength of two B_4C photocathodes: B4C 040 (20 nm) without Cr and B4C 055 (50 nm) with Cr (3 nm), both measured in the reflective mode. B4C 040 has higher QE, equals 0.24% @ 160 nm, than B4C 055 and above 170 nm both samples cannot be measured due to photocurrent being in the noise.

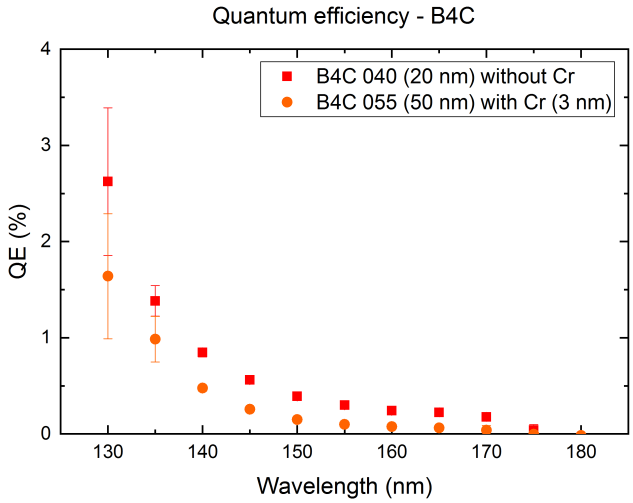

Figure 6.3: QE vs wavelength of two B_4C photocathodes: B4C 040 (20 nm) on MgF_2 (5 nm) without Cr and B4C 055 (50 nm) on MgF_2 (3 nm) with Cr, both measured in the reflective mode.

6.2.4 Hydrogenated nanodiamonds

Figure 6.4 shows the plot of QE vs wavelength of five (H)ND photocathodes: HND 064 (25 shots), HND 060 (50 shots), ND 067 (200 shots), HND 066 (200 shots) and HND 059 (260 shots), all measured in the reflective mode. The highest QE is observed for HND with 260

shots, equals 3.02% @ 160 nm, and HND with 50 shots, equals 3.12% @ 160 nm. In general, the more shots, the higher QE, however, HND with 50 shots is an exception. The reason may be not precise application of the photocathode layer or lack of uniformity. If a location which is not well coated is bombarded, as it was presented in position scanning measurements in Subsection 5.4.3, a response varies strongly. Therefore, it is possible that the beam was not hitting a location with good coating if it was not well aligned.

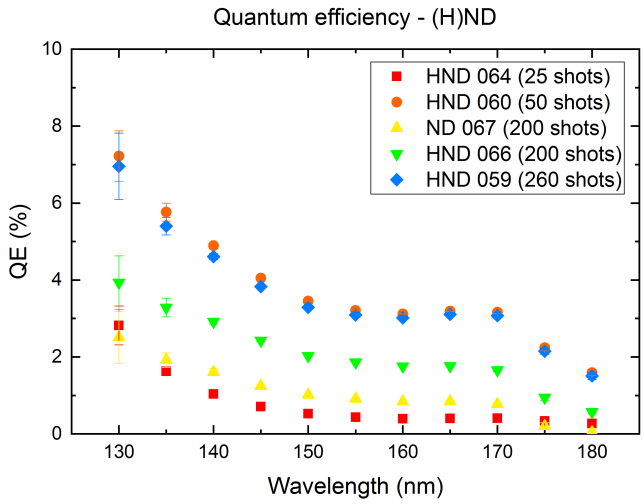

Figure 6.4: QE vs wavelength of five (H)ND photocathodes: HND 064 (25 shots), HND 060 (50 shots), ND 067 (200 shots), HND 066 (200 shots) and HND 059 (260 shots), all measured in the reflective mode.

6.2.5 Comparison of investigated materials

Figures 6.5 and 6.5 present the summary of the best samples of each material that was measured: CsI 069, DLC 010, B4C 040 and HND 060, all measured in the reflective mode. The highest QE values are observed for CsI sample. HND is second best candidate for a photocathode after CsI. QE values of DLC and B4C are low in comparison to other materials.

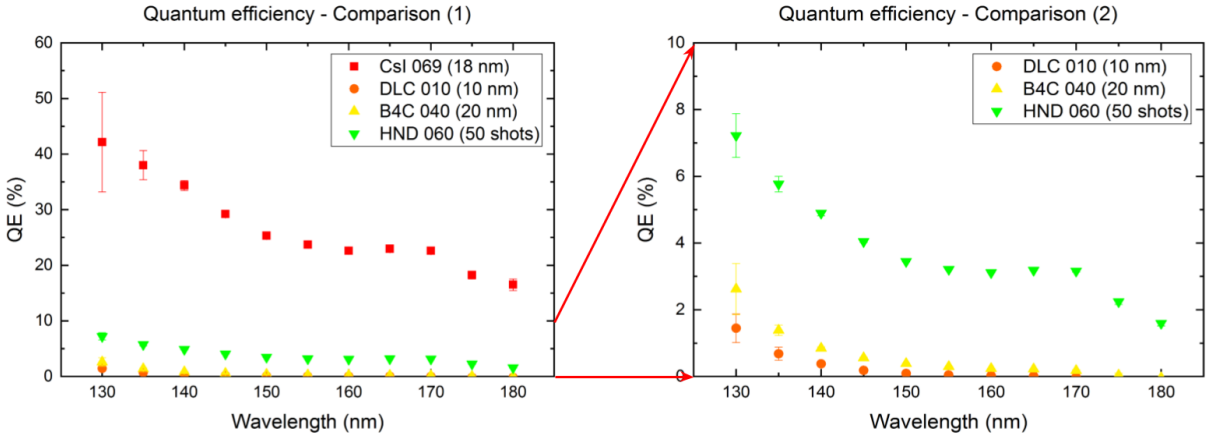

Figure 6.5: Left side: QE vs wavelength of four different photocathodes: CsI 069, DLC 010, B4C 040 and HND 060, all measured in the reflective mode. Right side: zoom view of the QE vs wavelength graph.

6.3 Transmission mode measurements

In the transmission mode, transparency vs wavelength measurements of a MgF_2 (3 mm) window, MgF_2 (3 mm) windows with different Cr layers as well as four different photocathode materials (CsI, DLC, B_4C and HND) were done. As for the reflective mode, QE vs wavelength measurements of these photocathodes were carried out. Tests were performed in pressures below 5E-6 mbar to obtain good VUV transmission. Results of all the measurements in the transmission mode are presented in Figures 6.6 - 6.16.

6.3.1 MgF_2 windows with Cr layer

Figure 6.6 and presents the results of transparency vs wavelength measurements of a MgF_2 (3 mm) window and MgF_2 (3 mm) windows with different Cr layers carried out in the transmission mode. In the range from 140 nm to 190 nm the measurements were done in a vacuum and above 200 nm in the air.

Sample 045 shows that the pure MgF_2 window has the transparency of about 80% @ 160 nm. The transparency of two 1.19 nm samples mainly overlaps - around 60% @ 160 nm - as well as of two 1.59 nm samples - about 57% @ 160 nm. In general, all four samples have similar transparency. For the 2.09 nm samples, the difference in transparency is quite significant: sample 078 is around 55% and sample 081 - about 52% @ 160 nm. Sample 081 was measured again, but in position set 0.75 cm higher than usually and in the way that the beam was still hitting the active area, however, in a different spot. The transparency was a bit lower in comparison to the first measurement - around 1 percentage point lower for each wavelength. Therefore, the Cr layer on the top of this sample could be not perfectly uniform. Moreover, the transparency of old Cr 3 nm sample 048 is much lower than in case of the new Cr samples.

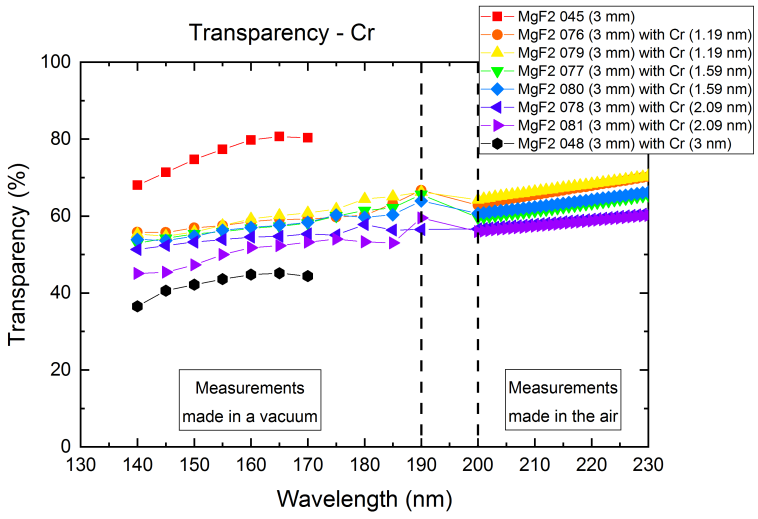

Figure 6.6: Transparency vs wavelength of a MgF_2 (3 mm) window and MgF_2 (3 mm) windows with different Cr layers. In the range from 140 nm to 190 nm the measurements were done in a vacuum and on the range from 200 nm to 230 nm - in the air.

6.3.2 Cesium Iodide

Figure 6.7 shows the dependence of transparency and wavelength of a MgF_2 (3 mm) window, a MgF_2 (3 mm) window with a Cr (3 nm) layer and a MgF_2 (3 mm) window with a Cr (3 nm) layer with CsI (18 nm) photocathode. For MgF_2 window, the transparency changes from 36% @ 130 nm to 80% @ 170 nm. Adding the Cr layer decreases the values almost by factor of 2 - the transparency from 7% @ 130 nm to 44% @ 170 nm. Finally, applying the CsI layer results in huge drop in transparency that oscillate around 0.10 across the measured wavelength range.

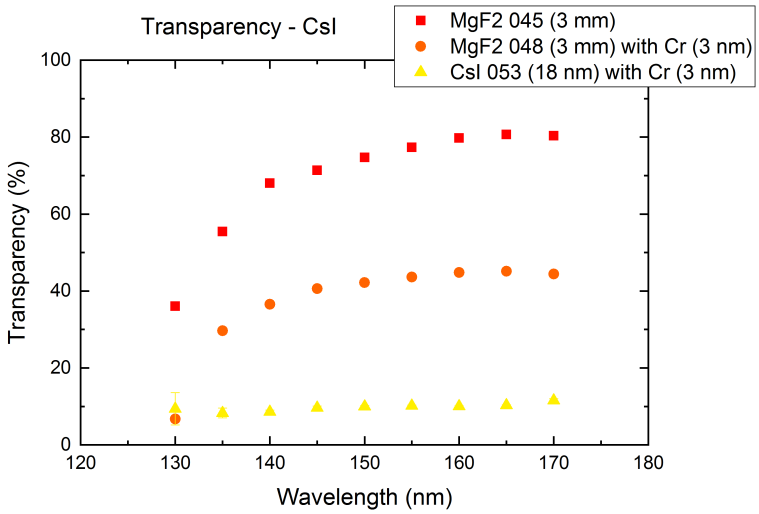

Figure 6.7: Transparency vs wavelength of a MgF_2 (3 mm) window, a MgF_2 (3 mm) window with a Cr (3 nm) layer and a MgF_2 (3 mm) window with a Cr (3 nm) layer with CsI (18 nm) photocathode.

Figure 6.8 shows the dependence of QE and wavelength of CsI 053 (18 nm) photocathode measured in the transmission mode. The values of QE oscillate around 10% on the measured wavelength range, which is much lower than QE values measured in the reflective mode. There is also a rise in QE from 150 nm, which can be an effect of a higher transparency in this range.

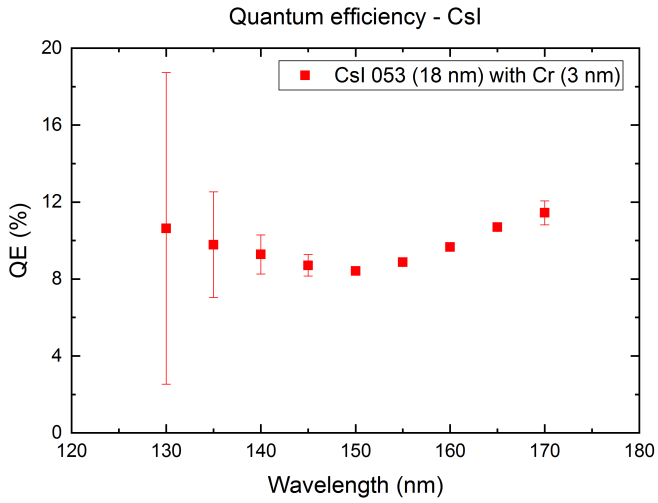

Figure 6.8: QE vs wavelength of CsI 053 (18 nm) photocathode measured in the transmission mode.

6.3.3 Diamond-Like Carbon

Figure 6.9 is a transparency vs wavelength graph of two DLC photocathodes: DLC 009 (3 nm) and DLC 050 (30 nm). The thinner sample, 3 nm DLC, has higher transparency - 55% @ 160 nm - than the thicker one, 30 nm DLC - 17% @ 160 nm.

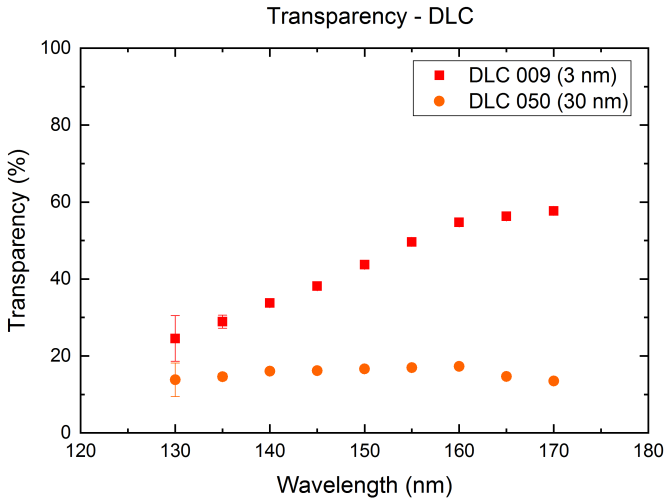

Figure 6.9: Transparency vs wavelength of two DLC photocathodes: DLC 009 (3 nm) and DLC 050 (30 nm).

Figure 6.10 shows the plot of QE vs wavelength of two DLC photocathodes: DLC 009 (3 nm) and DLC 050 (30 nm), both measured in the transmission mode. DLC 050 shows better QE than DLC 009.

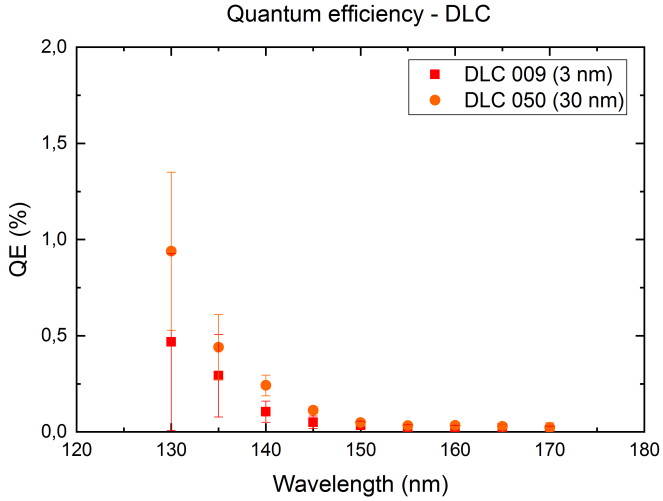

Figure 6.10: QE vs wavelength of two DLC photocathodes: DLC 009 (3 nm) and DLC 050 (30 nm), both measured in the transmission mode.

The comparison of the factor in QE between CsI and DLC in ASSET measurement and the number of photoelectrons ("Npe") generated by Cherenkov light on the surface of photocathode layer per muon for CsI and DLC from reference [29] was conducted. The ratio of QE @ 160 nm

for CsI and DLC in the ASSET measurement in the transmission mode equals 300. The ratio of "Npe" per muon for CsI and DLC from reference [29] equals 4.35. The discrepancy between the ratio of photoelectrons obtained during test beam measurements between CsI and DLC photocathodes and the QE measurements in the ASSET setup is not understood at the moment. Secondary emission from photocathode layers may contribute to the increased photoelectron yield in particle test beams but further studies are necessary to confirm the significance of this process.

6.3.4 Boron Carbide

Figure 6.11 presents the relationship between transparency and wavelength of seven B_4C photocathodes of different thicknesses and with/without Cr layer. The general dependence is that the thicker sample, the lower the transparency. In addition, the presence of Cr layer decreases the transparency. The highest transparency is observed for B4C 047 (2.5 nm) with Cr layer and equals 24% @ 160 nm.

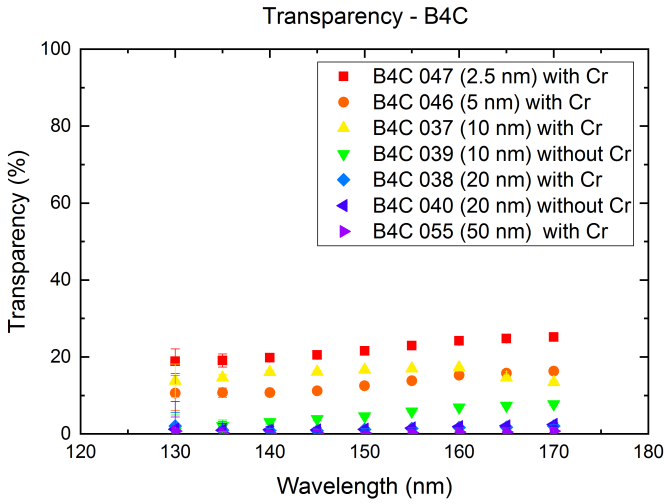

Figure 6.11: Transparency vs wavelength of seven B4C photocathodes of different thicknesses and with/without Cr layer.

Figure 6.12 presents the QE vs wavelength graph of seven B_4C photocathodes of different thicknesses and with/without Cr layer, all measured in the transmission mode. The dependence of QE on thickness for transmission mode is a balance between too much and not enough absorption: a layer needs to be thick enough to absorb light and produce electrons. However, the layer cannot be too thick, otherwise light is absorbed at the beginning of the layer (close to interface with substrate) and it is too deep for electrons to travel all the way through the layer to be extracted on the other side. The dependence is also connected to the transparency measurements: the higher the transparency, the better the QE. The results of the measurements below show that the general rule is that the thicker the photocathode layer, the worse the QE and the best QE is observed for B4C 047 (2.5 nm) with Cr layer.

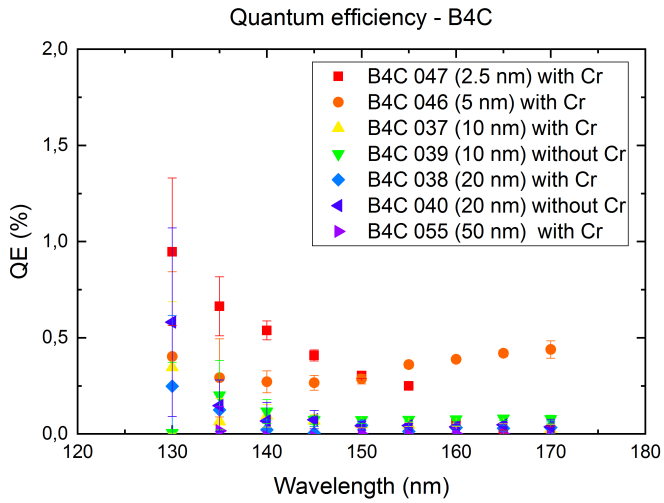

Figure 6.12: QE vs wavelength of seven B4C photocathodes of different thicknesses and with/without Cr layer, all measured in the transmission mode.

6.3.5 Hydrogenated nanodiamonds

Figure 6.13 is a transparency vs wavelength graph of two HND photocathodes: HND 061 (60 shots) and HND 063 (100 shots). In this case, the thicker sample, 100 shots HND, has higher transparency - 25% @ 160 nm - than the thinner one, 60 shots HND - 16% @ 160 nm. The reason for such an unexpected result can be explained similar as in was done for the reflective mode measurements in Subsection 6.2.4: there is a possibility that bombarded area was not well aligned or coated properly, therefore, there is a lot of doubt in the result. In addition, the spray technique used may yield varying results depending on solution, therefore it should be considered as a preliminary technique.

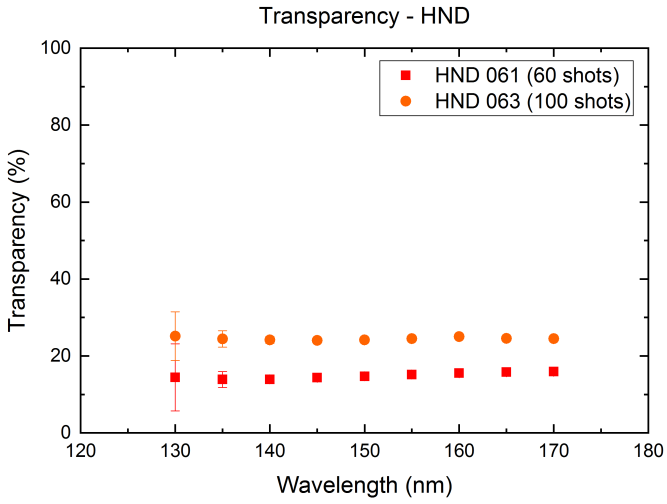

Figure 6.13: Transparency vs wavelength of two HND photocathodes: HND 0061 (60 shots) and HND 0063 (100 shots).

Figure 6.14 shows the dependence of QE and wavelength of two HND photocathodes: HND 061 (60 shots) and HND 053 (100 nm), both measured in the transmission mode. HND 053 shows better QE than HND 061.

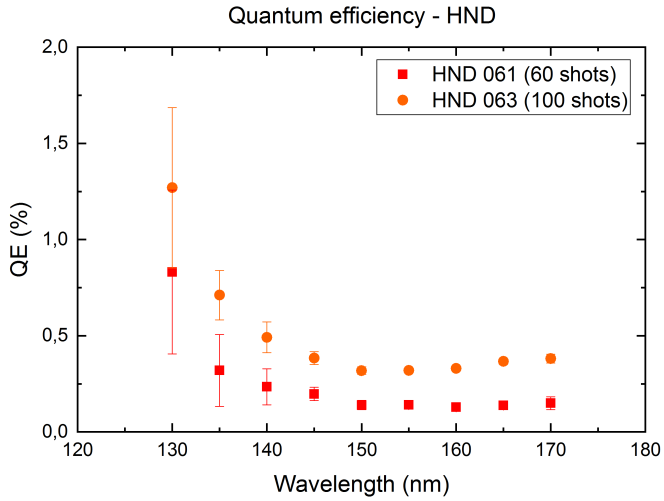

Figure 6.14: QE vs wavelength of two HND photocathodes: HND 061 (60 shots) and HND 053 (100 nm), both measured in the transmission mode.

6.3.6 Comparison of investigated materials

Figure 6.15 presents transparency vs wavelength of a window only, a window with Cr layer and four windows with photocathode layers made of different materials: CsI 053, DLC 009, B4C 047 and HND 063. The best transparency (concerning photocathodes) is observed for DLC sample without Cr layer. B_4C and HND photocathodes show similar values and CsI sample has the lowest transparency from all measured materials.

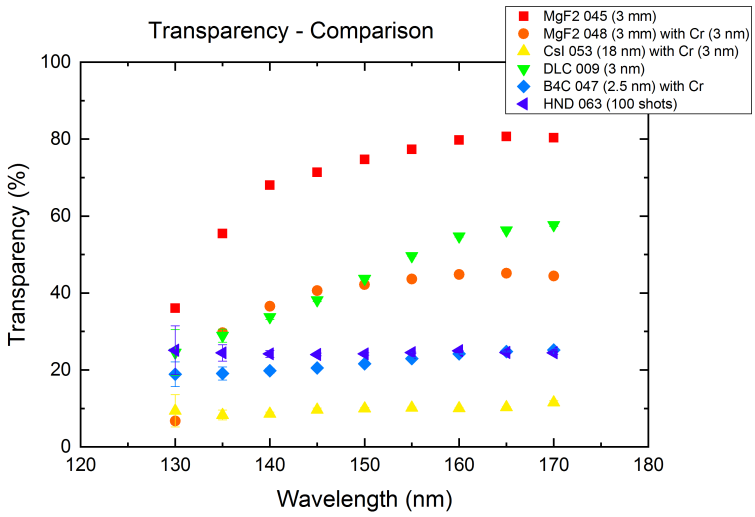

Figure 6.15: Transparency vs wavelength of two windows without photocathode and four windows with photocathode layers made of different materials: CsI 053, DLC 009, B4C 047 and HND 063.

Figure 6.16 presents the results of four photocathodes made of different materials: CsI 053, DLC 009, B4C 047 and HND 063, all measured in the transmission mode. The best QE is observed for CsI sample. HND is second best candidate for a photocathode after CsI. QE values of DLC and B_4C are lower than other materials.

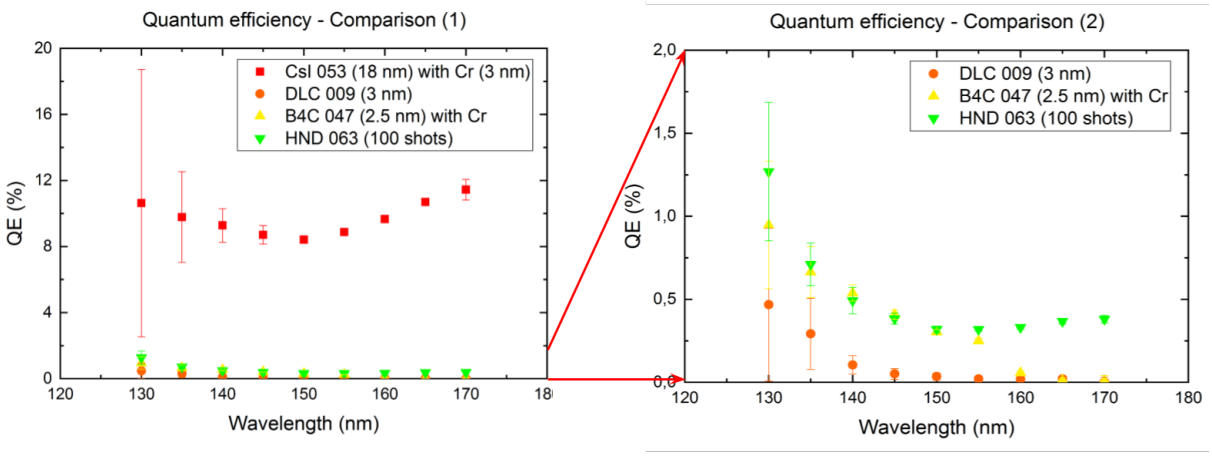

Figure 6.16: Left side: QE vs wavelength of different photocathodes: CsI 053, DLC 009, B4C 047 and HND 063, all measured in the transmission mode. Right side: zoom view of the QE vs wavelength graph.

6.4 Ageing studies

The ageing studies under ion bombardment are an important part of ASSET measurements in a view of the application in the PicoSec detector. Figure 6.17 presents an example of QE vs wavelength measurements before and after several steps of irradiation of the CsI 058 (18 nm) sample. The graph shows that CsI indeed suffers from ion bombardment. The results of ageing studies of all measured samples including CsI (without and with protection layers), B_4C and HND are shown in Figures 6.18 - 6.28.

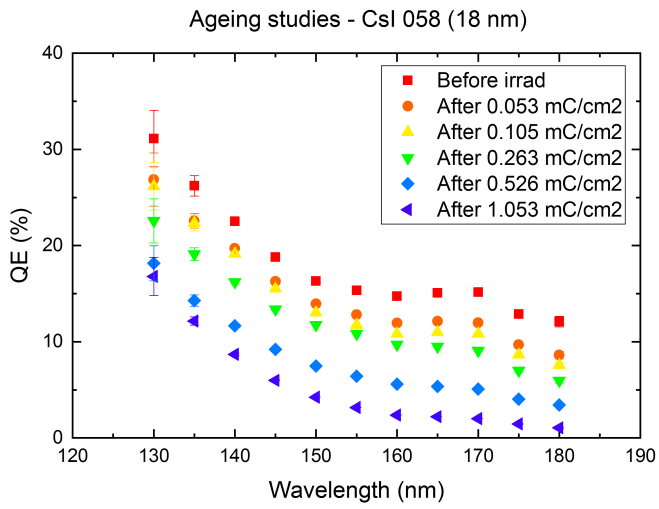

Figure 6.17: QE vs wavelength before and after several steps of irradiation of the CsI 058 (18 nm).

6.4.1 Cesium Iodide

Figures 6.18 and 6.19 present respectively QE and QE decrease @ 160 nm vs charge accumulated of two CsI photocathodes. Sample CsI 068 (18 nm) was placed in the position nr 1. inside the holder, while sample CsI 069 (18 nm) in the position nr 3. (distance between the middle of the samples was 8 cm). Both samples were measured before the ageing. Then CsI 068 (18 nm) was irradiated in several steps and measured after each of them, while CsI 069 was used as a reference and it was just measured. After about 10.5 mC/cm^2 of charge accumulated, QE of CsI 068 dropped from initial value of 21.6% to 2.13%, while QE of CsI 069 from 22.6% to 13.4%, that corresponds to the QE decrease of 90% and 41%, respectively. The QE drop of CsI 069 may come from unwanted parasitic ion bombardment or low gas quality in the chamber.

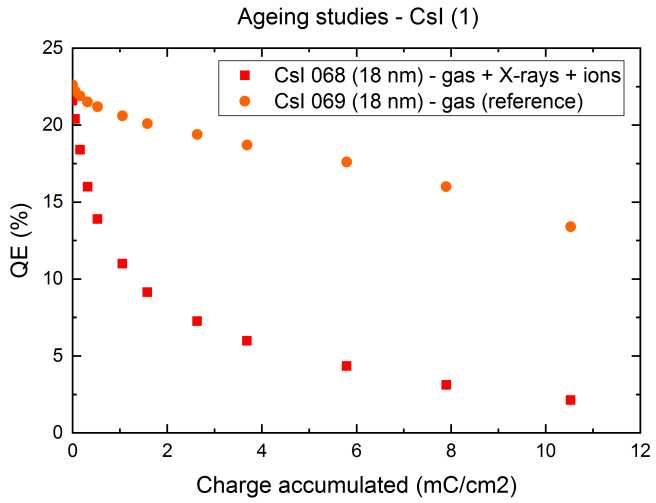

Figure 6.18: QE @ 160 nm vs charge accumulated of two CsI photocathodes: CsI 068 (18 nm) that was measured and irradiated and CsI 069 (18 nm) that was used as a reference and it was just measured.

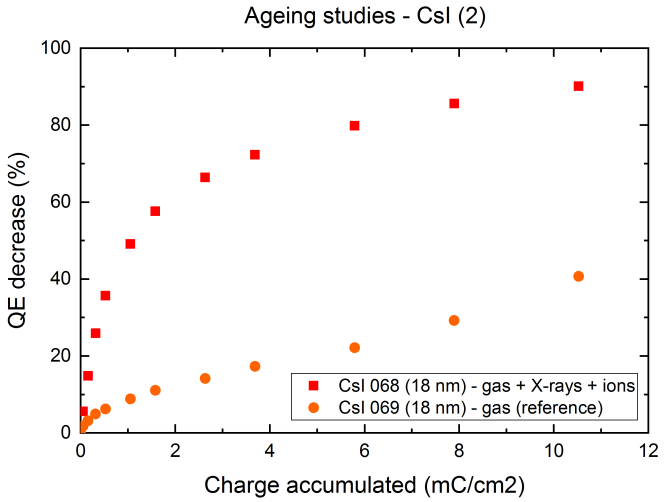

Figure 6.19: QE decrease @ 160 nm vs charge accumulated of two CsI photocathodes. QE decrease of CsI 068 and CsI 069 after about 10.5 mC/cm^2 charge accumulated equals 90% and 41%, respectively.

The results of QE decrease vs charge accumulated were compared with the reference [30]. In the reference, measurements of QE decrease after different number of days of the CsI photocathode being kept inside the experimental setup were presented and can be seen in Figure 6.20. QE decrease depends on the number of days of the sample being kept inside the chamber. As the measurements in this thesis were made right after assembling the photocathode inside the setup, the result of the measurement after 2 days from the reference [30] was taken into account. After 10 mC/cm^2 of charge accumulated in the measurement carried out in this thesis, QE decrease equals almost 90%, while in the reference it is about 55%. Figures 6.19 and 6.20 show that both curves have qualitatively similar behaviour, however, the thickness of the CsI layer described in the reference [30] is unknown, therefore, the numbers cannot be properly compared.

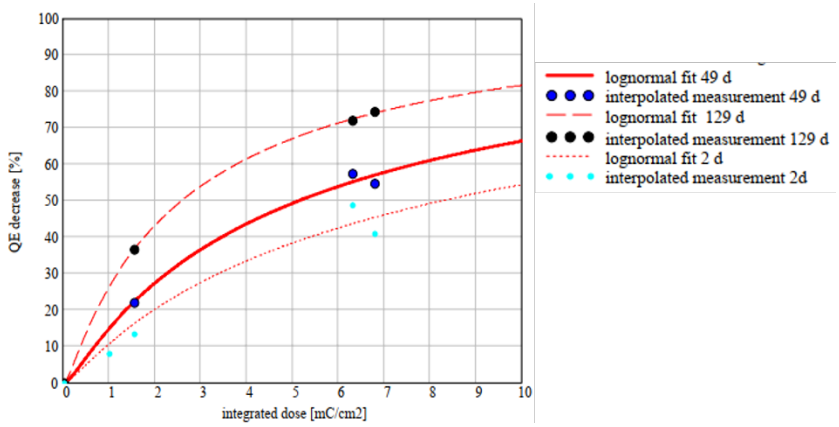

Figure 6.20: QE decrease @ 160 nm vs charge accumulated of CsI photocathode from reference [30].

Figures 6.21 and 6.22 show respectively QE and QE decrease @ 160 nm vs charge accumulated of three CsI photocathodes: pure CsI 068 (18 nm), CsI 070 (18 nm) with LiF (2 nm) protection layer and CsI 071 (18 nm) with MgF_2 (2 nm) protection layer. Pure CsI 0068 has the highest QE, while the protection layers of the samples CsI 070 and CsI 0071 decrease their QE. QE decrease of CsI 068, CsI 070 and CsI 071 after 10.5 mC/cm^2 charge accumulated equal 90%, 97% and 82%, respectively. All three samples were degraded very fast and the protection layers did not improve the robustness of the CsI photocathodes against QE decrease.

6.4.2 Diamond-Like Carbon

DLC samples were shown to be stable in other measurements [29] , however, they were not investigated in ageing studies in this work due to already very low QE to start with. Instead, the measurements of other materials that show higher QE were presented within this thesis.

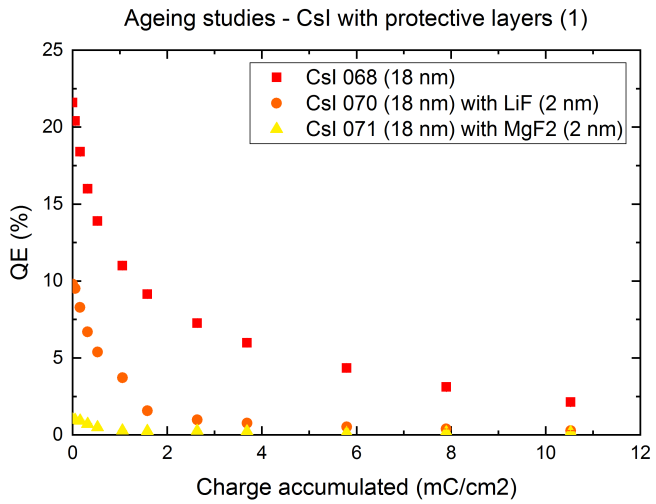

Figure 6.21: QE @ 160 nm vs charge accumulated of three CsI photocathodes: pure CsI 068 (18 nm), CsI 070 (18 nm) with LiF (2 nm) protection layer and CsI 071 (18 nm) with MgF_2 (2 nm) protection layer.

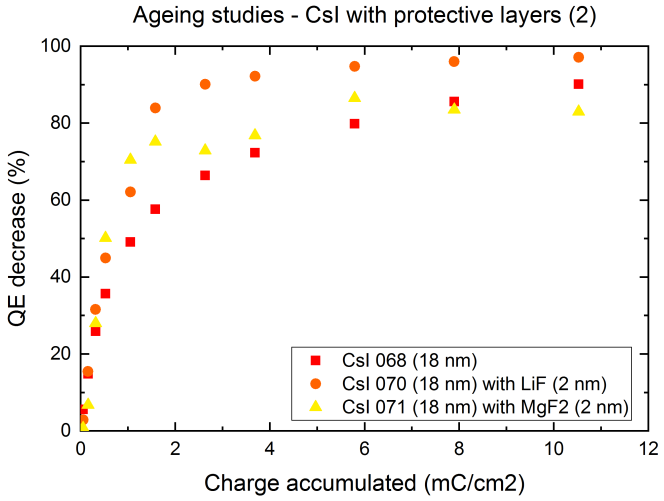

Figure 6.22: QE decrease @ 160 nm vs charge accumulated of three CsI photocathodes. QE decrease of CsI 068, CsI 070 and CsI 071 after 10.5 mC/cm^2 charge accumulated equal 90%, 97% and 82%, respectively.

6.4.3 Boron Carbide

Figures 6.23 and 6.24 present respectively QE and QE decrease @ 160 nm vs charge accumulated of B4C 040 (20 nm) on MgF_2 (5 nm) without Cr. QE of the sample after first irradiation is much higher than before irradiation which is an unexpected behaviour and may be attributed to charging up of the sample. The effect of charging up might be explained by the large resistance/low conductivity of the samples. QE decreases with charge accumulated: after 5.8 mC/cm^2 charge accumulated it equals 47%. The values measured 20h (red circle) and 5 days (blue circle) after the last irradiation are getting lower - QE decrease equals 56% and 66%, respectively, supporting the hypothesis that charging up modifies the observed currents and thus measured QE right after irradiation.

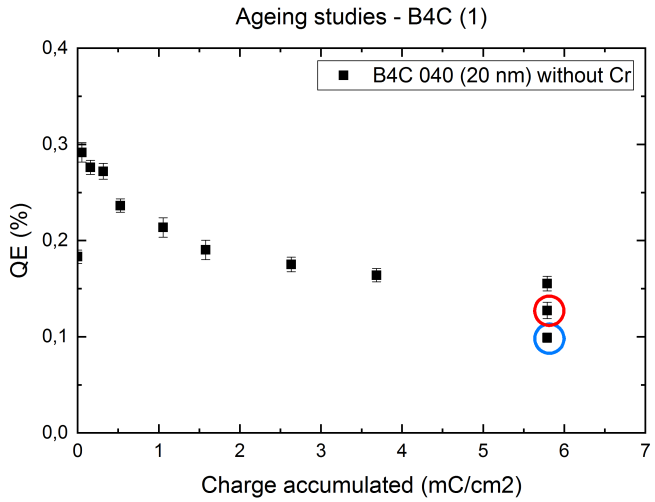

Figure 6.23: QE @ 160 nm vs charge accumulated of B4C 040 (20 nm) on MgF_2 (5 nm) without Cr.

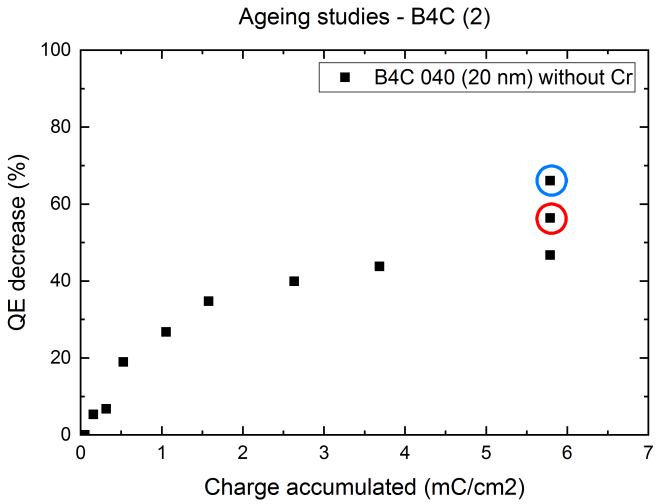

Figure 6.24: QE decrease @ 160 nm vs charge accumulated of B4C 040. Due to the fact that QE of the sample after first irradiation is much higher than before irradiation, the initial point was set at the first value after irradiation (0.05 mC/cm^2).

6.4.4 Hydrogenated nanodiamonds

Figures 6.23 and 6.24 show respectively QE and QE decrease @ 160 nm vs charge accumulated of of three (H)ND photocathodes: ND 067 (200 shots), HND 066 (200 shots) and HND 059 (260 shots). HND with 260 shots has the highest QE, while both samples of 200 shots have quite low QE values during the whole process of ageing studies. The QE decrease of HND 059, HND 066 and ND 067 after more than 8 mC/cm^2 charge accumulated equals 75%, 35% and 55%, respectively. HND with 260 shots was the most degraded sample, while the smallest QE decrease was observed for HND with 200 shots.

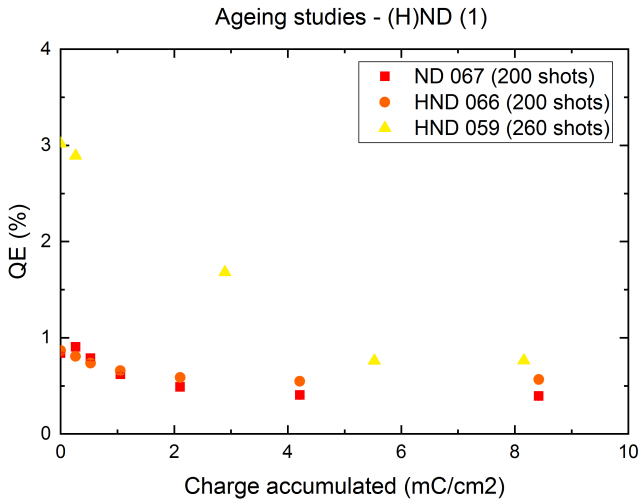

Figure 6.25: QE @ 160 nm vs charge accumulated of three (H)ND photocathodes: ND 067 (200 shots), HND 066 (200 shots) and HND 059 (260 shots).

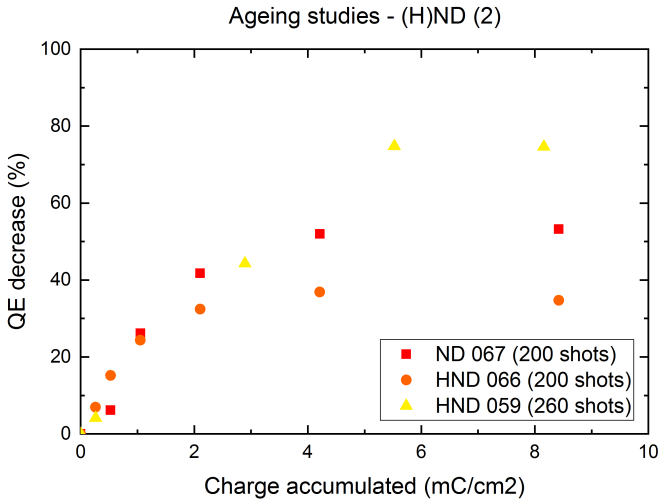

Figure 6.26: QE decrease @160 nm vs charge accumulated of three (H)ND photocathodes. The QE decrease of HND 059, HND 066 and ND 067 after more than 8 mC charge accumulated equal 75%, 35% and 55%, respectively.

6.4.5 Comparison of investigated materials

Figures 6.23 and 6.24 present respectively QE and QE decrease @ 160 nm vs charge accumulated of three different photocathode materials that were the best in theirs groups: CsI 068 (18 nm), B4C 040 (20 nm) on MgF_2 (5 mm) without Cr and HND 066 (200 shots). The highest values of QE were observed for CsI 068, while for B4C 040 and HND 066 they were low, however CsI 068 was the most degraded sample, while the smallest QE decrease was observed for HND 066.

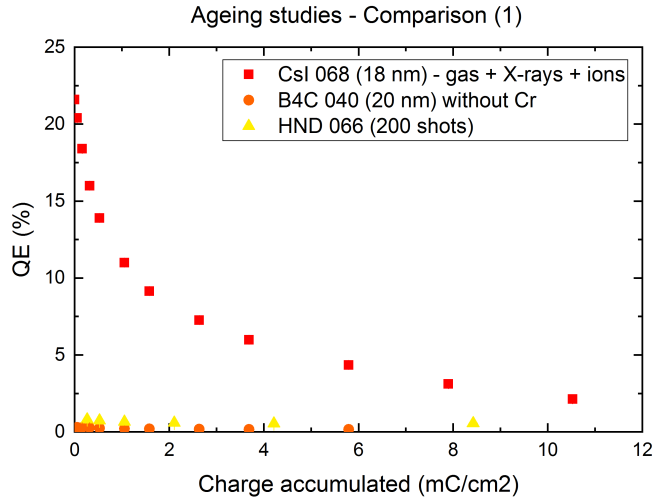

Figure 6.27: The comparison of QE @ 160 nm vs charge accumulated of three different photocathode materials: CsI 068 (18 nm), B4C 040 (20 nm) on MgF_2 (5 mm) without Cr and HND 066 (200 shots).

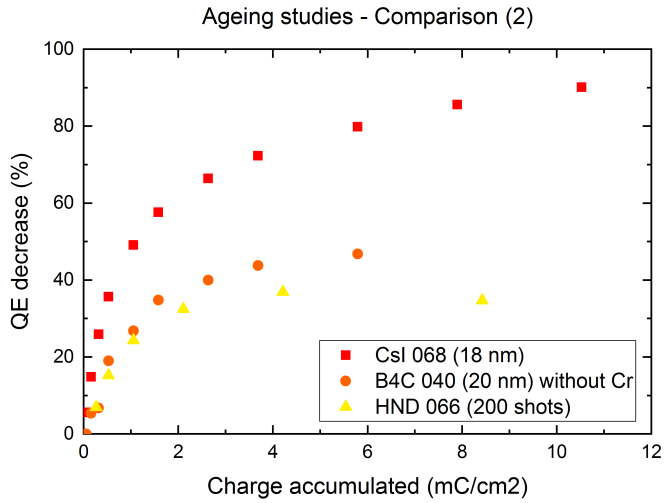

Figure 6.28: The comparison of QE decrease @ 160 nm vs charge accumulated of three different photocathode materials. CsI 068 was the most degraded sample, while the smallest QE decrease was observed for HND 066.

Chapter 7

Conclusions

The studies presented within the scope of this Master's thesis were targeted for robust photocathodes for precise-timing gaseous detectors. Main goals were to examine different photocathode materials as well as protective layers and carry out ageing studies of photocathodes under ion bombardment to find and choose a well-suited photocathode for the PicoSec detector. Therefore, wavelength-resolved quantum efficiency (QE) measurements and accelerated ageing studies of 4 photocathode materials were done. The samples included: cesium iodide (CsI), diamond-like carbon (DLC), boron carbide (B_4C) and hydrogenated nanodiamonds (HND).

Cesium iodide, the photocathode material that was chosen for the first prototype of the PicoSec detector, is characterised by high QE and UV sensitivity. However, CsI is sensitive to humidity and sparks, which results in the degradation of QE. In order to minimise effects of ion back flow on CsI and mitigate degradation, the protection layers including MgF_2 and LiF were tested. The reflective mode measurements demonstrated that the protection layers inhibit the extraction of electrons and result in low QE. CsI with LiF protection layer has higher QE values than CsI with MgF_2, which makes the first one more promising candidate to replace pure CsI. Unfortunately, the results of ageing studies showed that all CsI samples degrade very fast and the protection layers do not improve the robustness of the CsI photocathodes against QE decrease.

Diamond-like carbon is a material that could replace CsI photocathodes due to its better robustness to environmental influence and ion bombardment. However, although DLC has the best transparency of all investigated materials, the QE values obtained with ASSET measurements are very low. Therefore, DLC samples were not investigated in ageing studies within this thesis.

For boron carbide, the QE values are very low in both reflective and transmission modes. The dependence of QE on thickness for transmission mode is a balance between too much and not enough absorption. The measurements results showed the general rule: the thicker the photocathode layer, the worse the QE. Ageing studies of B_4C demonstrated its slower degradation in comparison to CsI. In addition, the effect of charging up of the sample was observed, which can be explained by the large resistance/low conductivity of B_4C.

When it comes to hydrogenated nanodiamonds, the material could also be an alternative solution for CsI photocathodes due to its good stability and robustness. From all investigated materials, HND samples show the best QE after CsI. In general, the thicker the layer, the better the values, however, the results showed that the samples were not uniform and the coatings were not precise. Nevertheless, HND demonstrated the smallest QE decrease, which makes it the best choice to replace CsI, concerning the materials tested within this thesis.

Summarising, the studies presented within the scope of this Master's thesis showed that CsI had the highest quantum efficiency, however, the degeneration of B_4C and HND was much slower. It may still not be a strong argument to replace CsI photocathodes, but the direction of the measurements is solid. The main achievement of the studies is that the setup has been tested and the results are reliable. Next step would be to examine more materials towards promising photocathodes for precise-timing gaseous detectors.

Bibliography

[1] S. White, *Experimental challenges of the European strategy for particle physics*, International Conference on Calorimetry for the High Energy Frontier, CHEF 2013: Paris, France, April 22–25, 118–127 (2013)

[2] F. J. Iguaz et al., *PICOSEC: Charged particle timing at sub-25 picosecond precision with a Micromegas based detector*, Nucl. Instr. Meth. A, 903, 317-325 (2018)

[3] M. Lisowska, *ASSET - Photocathode characterisation device*, RD51 MiniWeek, Genewa, Switzerland, 10-13 Feb 2020

[4] `https://en.wikipedia.org/wiki/Photocathode`, access date: 11.06.2021

[5] G. F. Knoll, *Radiation detection and measurement (3rd ed.)*, Wiley, New York, USA (1999)

[6] F. Sauli, *Gaseous Radiation Detectors: Fundamentals and Applications*, Cambridge University Press, European Organisation for Nuclear Research, CERN, Geneva, Switzerland (2014)

[7] H. Bethe et al., *Experimental Nuclear Physics. Volume 1.*, New York, 253 (1953)

[8] `https://en.wikipedia.org/wiki/Bremsstrahlung`, access date: 11.06.2021

[9] `https://web2.uwindsor.ca/courses/physics/high_schools/2006/Medical_Imaging/x%20ray%20brem.gif`, access date: 11.06.2021

[10] `https://www.orau.org/ptp/collection/xraytubescoolidge/coolidgeinformation.htm`, access date: 11.06.2021

[11] `https://www.open.edu/openlearn/health-sports-psychology/health/imaging-medicine/content-section-2.2.1`, access date: 11.06.2021

[12] P. A. Cerenkov, *Visible Emission of Clean Liquids by Action of γ Radiation*, Doklady Akad. Nauk SSSR 2, 451 (1934)

[13] `https://commons.wikimedia.org/w/index.php?curid=2277813`, access date: 11.06.2021

[14] J.Seguinot, T.Ypsilantis, *Photo-ionization and Cherenkov ring imaging*, Nucl. Instr. Meth, 142, 377-391 (1977)

[15] `http://www.nuclear-power.net/nuclear-power/reactor-physics/interaction-radiation-matter/interaction-gamma-radiation-matter`, access date: 11.06.2021

[16] https://en.wikipedia.org/wiki/Photoelectric_effect, access date: 11.06.2021

[17] https://en.wikipedia.org/wiki/Compton_scattering, access date: 11.06.2021

[18] https://en.wikipedia.org/wiki/Pair_production, access date: 11.06.2021

[19] G. C. Montgomery, D. D. Montgomery, *Geiger–Mueller Counters*, J. Franklin Inst., 231, 447 (1941)

[20] https://en.wikipedia.org/wiki/Gaseous_ionization_detector, access date: 11.06.2021

[21] G. Charpak et al., *The use of multiwire proportional counters to select and localize charged particles*, European Organisation for Nuclear Research, CERN, Geneva, Switzerland (1968)

[22] https://en.wikipedia.org/wiki/Wire_chamber, access date: 11.06.2021

[23] S. D. Pinto, *Micropattern gas detector technologies and applications, the work of the RD51 collaboration*, IEEE Nuclear Science Symposium 2010 Conference Record

[24] A. Oed, *Position-sensitive detector with microstrip anode for electron multiplication with gases*, Nucl. Instr. Meth. A, 263, 351–359 (1988)

[25] F. Sauli, *GEM: A new concept for electron amplification in gas detectors*, Nucl. Instr. Meth. A, 386, 531–534 (1997)

[26] P. Thuiner et al., *Multi-GEM Detectors in High Particle Fluxes*, EPJ Web of Conferences, 174, 05001 (2018)

[27] *CMS Technology Transfer: Homeland security application of CMS GEMs. 2017 CERN, for the benefit of the CMS Collaboration*

[28] Y. Giomataris et al., *MICROMEGAS: a high-granularity position-sensitive gaseous detector for high particle-flux environments*, Nucl. Instr. Meth. A, 376, 29–35 (1996)

[29] Xu Wang et al., *Study of DLC photocathode for PICOSEC detector*, RD51 Collaboration Meeting, Oct 2020

[30] H. Hödlmoser, *Development of Large Area CsI Photocathodes for the ALICE/HMPID RICH Detector*, CERN PhD Thesis (2005)

[31] https://www.mcphersoninc.com/pdf/632.pdf, access date: 11.06.2021

[32] https://mcphersoninc.com/spectrometers/vuvuvvis/model234302.html, access date: 11.06.2021

[33] Yi Zhou et al., *Production and performance study of Diamond-Like Carbon resistive electrode in MPGD*, Nucl. Instr. Meth. A, 958, 162759 (2020)

[34] Triloki on behalf of INFN Trieste and INFN Bari collaboration, *Preliminary results of ND Photocathode coupled to THGEMs*, RD51 MiniWeek, Genewa, Switzerland, 10-13 Feb 2020

[35] A. Breskin et al., *New Ideas in CsI-Based Photon Detectors: Wire Photomultipliers and Protection of the Photocathodes*, IEEE Transactions on Nuclear Science, 42, 298-305 (1995)